Stony Brook University

Wave gradiometry and its link with Helmholtz equation solutions applied to USArray

A Dissertation presented

by

Yuanyuan Liu

to

The Graduate School

in Partial Fulfillment of the

Requirements

for the Degree of

Doctor of Philosophy

in

Geosciences

Stony Brook University

May 2016

Stony Brook University

The Graduate School

Yuanyuan Liu

We, the dissertation committe for the above candidate for the

Doctor of Philosophy degree, hereby recommend

acceptance of this dissertation

William Holt - Dissertation Advisor
Professor at Department of Geosciences

_____

Daniel Davis - Chairperson of Defense
Professor at Department of Geosciences

_____

Lianxing Wen - Committee of Defense
Professor at Department of Geosciences

_____

Donald Weidner - Committee of Defense
Professor at Department of Geosciences

_____

Ryan Porter - Committee of Defense
Professor in Earth Sciences at Northern Arizona University

_____

This dissertation is accepted by the Graduate School

_____

Charles Taber
Dean of the Graduate School

Abstract of the Dissertation

Wave gradiometry and its link with Helmholtz equation solutions applied to USArray

by

Yuanyuan Liu

Doctor of Philosophy

in

Geosciences

Stony Brook University

2016

Wave gradiometry is an array processing technique using the shape of seismic wavefields captured by dense seismic arrays to estimate fundamental wave propagation characteristics [*Langston*, 2007a,b; *Liang and Langston*, 2009]. We first explore a compatibility relation that links the spatial gradients to displacements and velocity seismograms through two unknown coefficients: $\vec{A}$ and $\vec{B}$. We show that the $\vec{A}$-coefficient corresponds to the gradient of logarithmic amplitude and the $\vec{B}$-coefficient corresponds approximately to the local wave slowness. These coefficients are solved through iterative, damped least-squares inversions to provide estimates of four gradiometry products: dynamic phase velocity, back-azimuth, radiation pattern and geometrical spreading. Furthermore, *Liu and Holt* [2015] have advanced the technique by estimating the spatial gradients in a continuous field and combining wave gradiometry with Helmholtz equation solutions to obtain structural phase velocity. Compared with the dynamic phase velocity obtained in

traditional methods, the structural phase velocity is independent of specific geometry of wavefields or source properties and thus it's more appropriate for surface wave tomography studies [*Wielandt*, 1993; *Friederich et al.*, 1995; *Lin and Ritzwoller*, 2011a; *Jin and Gaherty*, 2015; *Liu and Holt*, 2015].

The $\vec{A}$ and $\vec{B}$-coefficients are then interpolated to explore a second compatibility relation through the Helmholtz equation solutions. For most wavefields passing through the eastern U.S., we show that the $\vec{A}$ vectors are generally orthogonal to the $\vec{B}$ vectors. Where they are not completely orthogonal, there is a strong positive correlation between $\nabla \cdot \vec{B}$ and changes in geometrical spreading, which can be further linked with areas of strong energy focusing and defocusing. We provide Rayleigh wave isotropic structural phase velocities for 15 period bands between 20 s and 150 s, by stacking and averaging results from 37 earthquakes. We observe a velocity change for 20 s - 30 s Rayleigh waves, along the approximate boundary of the early Paleozoic continental margin. The most prominent features in the eastern U.S. are two low velocity anomalies, one centered over the central Appalachians (referred to as the Central Appalachian Anomaly, CAA) where Eocene basaltic volcanism occurred [*Schmandt and Lin*, 2014; *Pollitz and Mooney*, 2016], and the other within the northeastern U.S. (referred to as the Northeast Anomaly, NEA), possibly associated with the Great Meteor Hotspot track [*Eaton and Frederiksen*, 2007; *Villemaire et al.*, 2012].

We continue to apply wave gradiometry to six earthquakes centered in Gulf of California with similar source locations, focal mechanisms, depths and magnitudes. These separate events occurred over a time frame such that their wavefields were captured by

the entire USArray Transportable Array. This analysis gives us an opportunity to investigate the characteristics of a wavefield, generated by a relatively consistent source, that propagates across the entire contiguous United States. We then apply wave gradiometry methods to synthetic waveforms obtained from two crust and upper mantle models of the U.S., a relatively smoothed model US_{00}, and an updated U.S. model US_{22} based on adjoint tomography. Given the correlations of gradiometry parameters from real records and synthetic data, and the similarity of source mechanisms for these six events, we combine gradiometry parameters for all events. This combined solution shows the wavefield characteristics from a single source, which defines the patterns of $\vec{A}$ and $\vec{B}$ vector fields and their spatial derivatives throughout the contiguous U.S. We show that the $\vec{A}$ vectors generally point along the steepest amplitude gradient towards amplitude highs, and they are generally orthogonal to the $\vec{B}$ vectors. These fields demonstrate the links between energy focusing/defocusing and amplitude variations. We are able to show that gradiometry parameters are sensitive to the underlying structures along with subtle variations in source radiation patterns. We thus argue these parameters can be used for determining viable structural models in the future. Furthermore, gradiometry parameters embedded in the transport equation, obtained from the imaginary part of the Helmholtz equation solutions, yields estimates of local amplification factors, which can potentially provide new constraints on the variations of elastic velocities and densities.

We finally combine wave gradiometry and Helmholtz equation solutions to process wavefields from 696 earthquakes between 2006 and 2014, with magnitudes larger than 5.0 and focal depths shallower than 50 km, recorded by 1,739 USArray TA stations.

After stacking, averaging, and smoothing Rayleigh wave structural phase velocities from all events, we obtain isotropic velocities and variances across the contiguous U.S. for the period range of 20 s - 150 s. The structural phase velocities generally increase with period from 3.2 ± 0.1 km/s (20 s) to 4.5 ± 0.2 km/s (150 s) and are consistent with the theoretical dispersion curves [*Dahlen and Tromp*, 1998]. Furthermore, we have identified several regions with potentially new constraints. For instance, we observe a belt of lower velocities along the Great Plains and Superior Uplands (SU) for the longest periods of 120 s - 150 s. The strong anomalies within the Central Appalachian Anomaly (CAA) and Northeast Anomaly (NEA) persist for the periods of 40 s - 150 s [*Schmandt and Lin*, 2014; *Porter et al.*, 2016]. We observe a semi-continuous band of lower phase velocities between South Georgia Rift (SGR) and NEA for the longest periods of 140 s - 150 s. These patterns may be signatures in the lower lithosphere left by the Central Atlantic Magmatic Province (CAMP) [*Heffner et al.*, 2012; *Pollitz and Mooney*, 2016], or due to hotspot interaction with the thermal-chemical lithosphere [*Chu et al.*, 2013]. The gradiometry parameters and products are archived for future studies to better constrain viable 3-D structural models.

In order to better understand the tectonic evolution in the North American continent, *Porter et al.* [2016] utilized seismic data recorded by USArray TA stations to build three-dimensional shear velocity models for the continental United States. The Rayleigh wave structural phase velocities are estimated using ambient noise tomography at short periods (8 s - 40 s) and wave gradiometry at longer periods (20 s - 150 s), which allows for a sensitivity to a broader depth range within the crust and upper mantle (6 - 200 km).

The high-resolution model provides us key information about orogenic and postorogenic events on the evolution of the lithosphere beneath those velocity anomaly regions [*Porter et al.*, 2016]. The lower and higher velocity regions in the western, central and eastern U.S. are all consistent with major geological provinces. The most prominent feature is the contrast in crustal and upper mantle structure between the relatively slow western and relatively fast eastern U.S. for all depths we investigated, similar to our Rayleigh wave structural phase velocity plots [*Liu and Holt*, 2015].

Dedicated to my father Qixin Liu, my mother Miaoying Zheng and my wife Xintong Qi.

Contents

Acknowledgements

Though only my name appears on the cover of this dissertation, a great many people have contributed to its production. My deepest gratitude is to my advisor, Prof. William Holt for the continuous support of my Ph.D study and related research, for his patience, motivation, and immense knowledge. I have been amazingly fortunate to have him as my advisor who gave me the freedom to explore on my own, and at the same time the guidance to recover when my steps faltered. His patience and support helped me overcome many crisis situations and finish this dissertation.

Besides my advisor, I would like to thank the rest of my thesis committee: Prof. Daniel Davis, Prof. Lianxing Wen, Prof. Donald Weidner, and Prof. Ryan Porter for their insightful comments and encouragement, but also for the hard question which inspired me to widen my research from various perspectives.

I thank my fellow labmates Gina Shcherbenko and Huiyu Yang for the stimulating discussions, and for all the fun we have had in the last five years.

I am also grateful to the following former or current staff at Geosciences Department, for their various forms of support during my graduate study - Yvonne Barbour, Owen Evans, Laura Colucci and Melissa Campo.

Most importantly, none of this would have been possible without the love and patience of my family. My immediate family to whom this dissertation is dedicated to, has been a constant source of love, concern, support and strength all these years. I would like to express my heart-felt gratitude to my parents and my wife.

Chapter 1

Wave Gradiometry and its Link with Helmholtz Equation Solution

1.1 Introduction

Embedded within the North American continental lithosphere is the history of continental growth, with many ancient terranes that have accreted since the Archean, including the Superior, Wyoming, Yavapai and Mazatzal Provinces, along with major structures associated with the Grenville and Appalachian orogenies [*Whitmeyer and Karlstrom*, 2007]. Furthermore, the continental interior contains several ancient rift structures [*Liang and Langston*, 2008]. Studies coming out of USArray have already revealed many exciting details about the crust and upper mantle beneath western and central North America [*Brudzinski and Allen*, 2007; *Lin et al.*, 2008; *Sigloch et al.*, 2008; *Yang and Ritzwoller*, 2008; *West et al.*, 2009; *Cao and Levander*, 2010; *Schmandt and Humphreys*, 2010; *Yuan and Romanowicz*, 2010; *Levander et al.*, 2011; *Obrebski et al.*, 2011; *Schmandt and*

Humphreys, 2011; *Shen et al.*, 2013a,b; *Evanzia et al.*, 2014; *Langston and Horton*, 2014; *Pollitz and Mooney*, 2014; *Porritt et al.*, 2014]. The lithosphere within these regions shows major lateral heterogeneity, with a complex upper mantle structure profoundly influenced by the history of subduction. Details for the eastern U.S., are beginning to emerge [*Burdick et al.*, 2014; *Lin et al.*, 2014; *Schmandt and Lin*, 2014; *Jin and Gaherty*, 2015]. One major question identified within the EarthScope Science Plan is whether seismic studies can reveal if these major terrane boundaries, and province interiors, have a crust/mantle signature [*Williams et al.*, 2010]. Secondly, what can the resolved structures tell us about continental accretion processes? Does the central and eastern U.S. lithosphere show similar heterogeneity as the western U.S.? Resolving lithosphere heterogeneity not only has implications for improving our understanding about the evolution of the continent, it also provides information that improves our understanding of the present-day dynamics of the North American lithosphere. That is, resolving structure provides constraints for temperature and possibly composition, which in turn provides constraints for density, internal body forces, and rheological heterogeneity. This information feeds into dynamic models (e.g. [*Ghosh and Holt*, 2012; *Ghosh et al.*, 2013]) of intraplate stress and strain, necessary for understanding intraplate earthquakes, an important goal of EarthScope Science Plan [*Liang and Langston*, 2008; *Williams et al.*, 2010].

We now have an important opportunity to apply the wave gradiometry technique to the wavefields sampled by dense USArray TA stations. This observational approach, involving quantification of the shape of wavefield, is the next important step in seismology that, when combined with theory, has the potential to lead to new important discoveries

regarding structural complexity and wavefield propagation characteristics. This work involves further development and use of wave gradiometry. We have implemented several new adaptations, including treatment of continuous displacement gradient fields within subarrays and a solution method for the Helmholtz equation. We show that gradiometry parameters can be used to investigate an approximation to the Helmholtz equation solution [*Wielandt*, 1993], as well as providing insight into the transport equation [*Cerveny*, 2005]. The gradiometry method is applied to multiple events recorded by USArray and reveals a rich field of information for each event, including significant effects of focusing and defocusing of energy, along with associated variations in geometrical spreading, radiation pattern and back-azimuth.

Gradiometry results for 55 s Rayleigh wave are described for four events. We also provide isotropic phase velocity maps in the eastern U.S. for 15 periods between 20 s to 150 s, by stacking and averaging results from 37 earthquakes. However, a detailed and comprehensive analysis of how spatial variations of gradiometry parameters are linked with 3-D structure modeling, including azimuthal anisotropy effects, are reserved for future analysis.

1.2 Methodology

Most traditional techniques in seismology, such as traveltime tomography, receiver function and shear wave splitting, apply some averaging methods, which treat each seismic station as an isolated observation [*Liang and Langston*, 2009]. This may smooth out or

ignore wavefield amplitude differences that reflect real structure or complexity. The wave gradiometry method, however, is designed to take advantage of the spatial variations of wave amplitudes sampled by the dense array, and resolve structure and propagation effects that cannot be derived strictly from the averaging methods [*Langston*, 2007a].

In a Cartesian coordinate system, the solution to the wave equation can be written as:

$$u(t, x, y) = G(x, y) f(t - p_x(x - x_0) - p_y(y - y_0)) \tag{1.1}$$

where u represents the displacement field, G represents the wave amplitude variation across space, f represents the phase variation as a function of time, t, and location $(x - x_0,\ y - y_0)$, p_x and p_y are components of the horizontal slowness in the x and y directions, respectively. Though equation (1.1) is a compatibility relation for a single dominant phase, we refer to the fact that *Langston* [2007a] showed that simultaneously arriving waves with the same frequency content generally do not provide a problem with the gradiometry treatment/approximation, so long as the amplitude of one of the two arrivals is small (at the noise level). Differentiating equation (1.1) gives us a set of equations, which link the spatial gradients to important wavefield propagation parameters [*Langston*, 2006, 2007a,b,c; *Liang and Langston*, 2009]:

$$\frac{\partial u}{\partial x} = A_x \cdot u + B_x \cdot \frac{\partial u}{\partial t} \tag{1.2}$$

$$\frac{\partial u}{\partial y} = A_y \cdot u + B_y \cdot \frac{\partial u}{\partial t} \tag{1.3}$$

where:

$$A_x = \frac{\partial G(x,y)}{\partial x} \cdot \frac{1}{G(x,y)} \qquad A_y = \frac{\partial G(x,y)}{\partial y} \cdot \frac{1}{G(x,y)} \tag{1.4}$$

$$B_x = -\Big[p_x + \frac{\partial p_x}{\partial x}(x - x_0)\Big] \qquad B_y = -\Big[p_y + \frac{\partial p_y}{\partial y}(y - y_0)\Big] \tag{1.5}$$

Integrating B_x and B_y over the interval $[x_0, x]$ gives the slowness in the x and y directions:

$$p_x = -\frac{1}{x - x_0}\int_{x_0}^{x} B_x dx \qquad p_y = -\frac{1}{y - y_0}\int_{y_0}^{y} B_y dy \tag{1.6}$$

When $x \to x_0$ and $y \to y_0$, the limit of equation (1.6) can be solved as:

$$p_x(x_0) = -B_x(x_0) \qquad p_y(y_0) = -B_y(y_0) \tag{1.7}$$

In general, the displacements, the spatial gradients and the time derivatives (velocity) of displacement field, measured at a single seismic station, can be used through equations (1.2) and (1.3) to iteratively solve for the $\vec{A}$ and $\vec{B}$-coefficients (discussed later in section 2.2). Then the following relations may be used through equations (1.4) and (1.7) to find phase velocity v, back-azimuth θ, radiation pattern $A_\theta(\theta)$, and geometrical spreading $A_r(\theta)$ [*Liang and Langston*, 2009]:

$$v = (B_x^2 + B_y^2)^{-\frac{1}{2}} \tag{1.8}$$

$$\theta = tan^{-1}(\frac{B_x}{B_y}) \tag{1.9}$$

$$A_\theta(\theta) = \frac{\partial G}{\partial \theta}\frac{1}{G} = r(A_x \cos\theta - A_y \sin\theta) \tag{1.10}$$

$$A_r(\theta) = \frac{\partial G}{\partial r}\frac{1}{G} = A_x \sin\theta + A_y \cos\theta \tag{1.11}$$

where r is the epicentral distance for the master station. There is a sign difference for $A_r(\theta)$ between equation (1.11) and equation (7) in *Liang and Langston* [2009]. We believe that the sign in *Liang and Langston* [2009] is a typo, as the correct expression is given by equation (10) in *Langston* [2007b].

Liang and Langston [2009] applied wave gradiometry to USArray data in the western U.S. They assumed that the wavefield parameters are constant across a given subarray, which is of order 200 - 400 km in dimension. In our work, we assume that the spatial gradients, and associated wave parameters, within a subarray define a spatially variable and continuous field. Being spatially continuous, we solve for the local values of wave parameters at each master station (x_0, y_0), and thus B_x and B_y represent the local wave slowness at position (x_0, y_0). It is thus important to have a station spacing capable of resolving spatial gradients in the vicinity of the master station. With the 70 km station spacing in USArray configuration, we are able to apply the wave gradiometry technique to the wavefields sampled by dense USArray TA stations (Figure 1.1). We will show

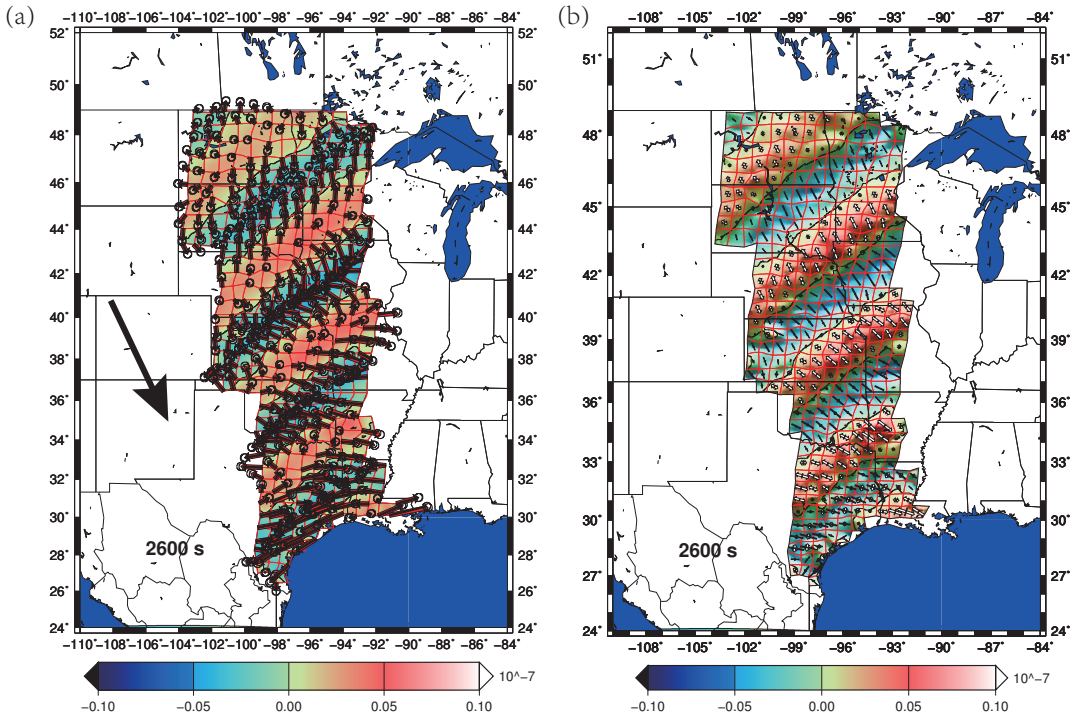

FIGURE 1.1: (a) Snapshot of the horizontal wavefields propagating through USArray TA Stations at 2600 s after the original time, from 2011 March 11 Great Tohoku-Oki earthquake. Red vector is observed horizontal displacement (with 95% confidence error ellipse) and the black vector is the model field predicted by the bi-cubic spline interpolation (described later). The contours show the spatial gradients of displacement field. The black arrow indicates the approximate wave propagation direction. (b) Contoured dilatational component of the strain field (spatial gradients) associated with Rayleigh wave. Principal axes of horizontal strain are also shown (bold = compressional; open = extensional).

later that this station spacing is capable of resolving significant wavefront curvature for periods longer than 20 s, caused by focusing/defocusing of energy.

1.2.1 Reducing Velocity Method

The supporting stations are found within 200 km radius of the master station, which is less than three wavelengths of the shortest period (20 s) to prevent the phase delay between two stations from exceeding the period of observation [*Jin and Gaherty*, 2015].

The reducing velocity method, as introduced by *Langston* [2007b], is applied to each subarray, which may effectively decrease the phase move-out and spatial gradients variations between the master station and its supporting stations [*Liang and Langston*, 2009].

The waveforms of supporting stations within a subarray are shifted relative to the master station, based on the distance and the mean velocity between the master station and its supporting stations. After applying the time shift, any spatial gradients of the displacement field in equations (1.2) and (1.3) are associated with normalized gradients of amplitude ($\vec{A}$-coefficients) and perturbations to the slowness estimate ($\vec{B}$-coefficients) [*Liang and Langston*, 2009]. Initially, we assume a uniform phase velocity across the subarray (3.8 km/s for periods shorter than 50 s and 4.0 km/s for periods longer than 60 s). The perturbation in slowness is estimated to define a new reducing velocity. With updated velocity estimates at all stations, the wavefields are shifted again, followed by new estimates of the spatial gradients and then new least-squares inversion for the coefficients. This process is repeated until convergence is achieved (usually 4 iterations, Figure 1.2).

1.2.2 Determining Spatial Gradient Tensor Field

Wave gradiometry equations (1.2) and (1.3) requires estimation of the spatial gradients of displacement wavefield. We interpolate the displacement field to return continuous estimates of the gradient tensor field within the subarray. The technique is a modification of methods used to analyze GPS data (e.g. [*Holt et al.*, 2000a,b; *Beavan and Haines*, 2001; *Holt and Shcherbenko*, 2013]). The displacement gradient tensor field is determined on a regular grid, with grid area spacing of $0.25^\circ \times 0.25^\circ$. Regularization of the solution

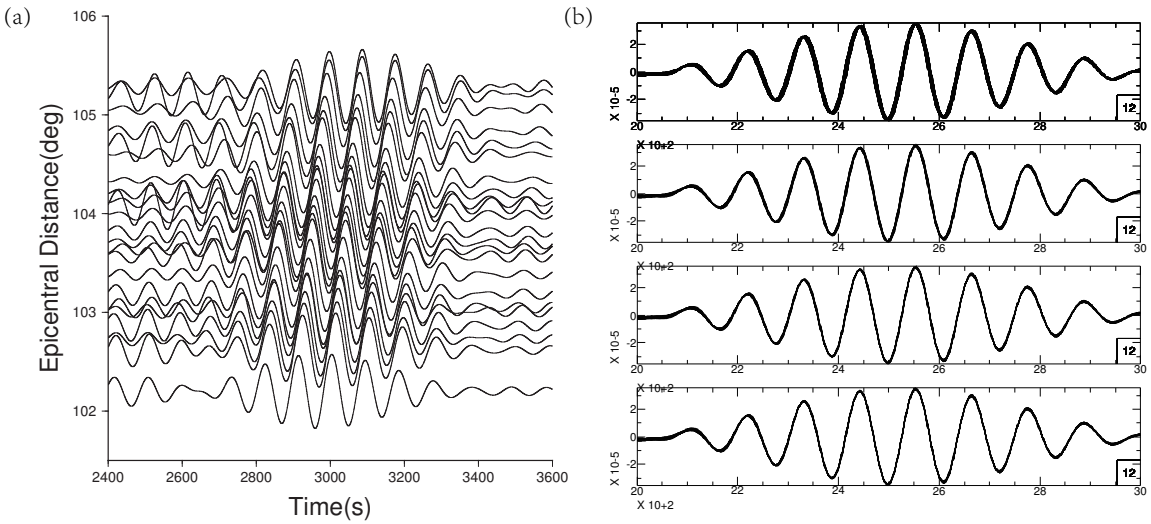

FIGURE 1.2: (a) Bandpass filtered waveforms recorded by USArray TA station D28A and its supporting stations from 2011 October 23, earthquake near Turkey. The dominant phase is Rayleigh wave. (b) Stack of shifted waveforms for the subarray in (a), after applying reducing velocity method, followed by least-squares inversion for slowness perturbation. The bottom panel is the final alignment after 4 iterations. The similarities are significant, but it is the spatial amplitude variations that carry wavefield characteristics along with the structural information across the space [*Liang and Langston*, 2009].

on this grid consists of obtaining the sharpest estimate of displacement gradient tensor field possible that can be supported by the displacement data (shifted wavefields within the subarray). The smoothing of the solution is controlled through optimization of the following functional in a formal least-squares inversion of the displacement field:

$$\chi = \sum_{cells} \sum_{ij,kl} (\hat{e}_{ij})^T V^{-1}_{ij,kl} (\hat{e_{kl}}) + \sum_{knots} \sum_{i,j} (\hat{u}_i - u_i^{obs})^T V^{-1}_{i,j} (\hat{u}_j - u_j^{obs}) \tag{1.12}$$

where $V_{ij,kl}$ is a weighting matrix for model strains, $V_{i,j}$ is the variance-covariance of displacement field, $\hat{e}_{ij}$ is the model strain, and $\hat{u}_i$ and u_i^{obs} are the predicted and observed displacements at a given time, respectively. The fitting algorithm that minimizes equation (1.12) is equivalent to a finite element method that satisfies force balance equations (spherical earth). The solution provides a best fit (in least-squares sense) to the displacement field, while the model second invariant of the strain tensor field is minimized. The methodology solves the weak formulation of the linear problem, where the basis functions for the displacements are higher order elements involving the Bessel form of bi-cubic spline interpolation on a generally curvilinear grid of quadrilateral sub-domains ($0.25^\circ \times 0.25^\circ$ grid) [*De Boor*, 1987; *Beavan and Haines*, 2001]. The final model predicts a continuous displacement gradient tensor field, with a posteriori model variance-covariance matrices [*Haines and Holt*, 1993; *Beavan and Haines*, 2001] for $\frac{\partial u}{\partial x}$ and $\frac{\partial u}{\partial y}$, which can be used to determine wave gradiometry parameter uncertainties [*Aster et al.*, 2011]. Finer grid spacing can be adapted to problems supported by dense station spacing. Furthermore, we have tested different grid spacings for the USArray TA stations configuration and

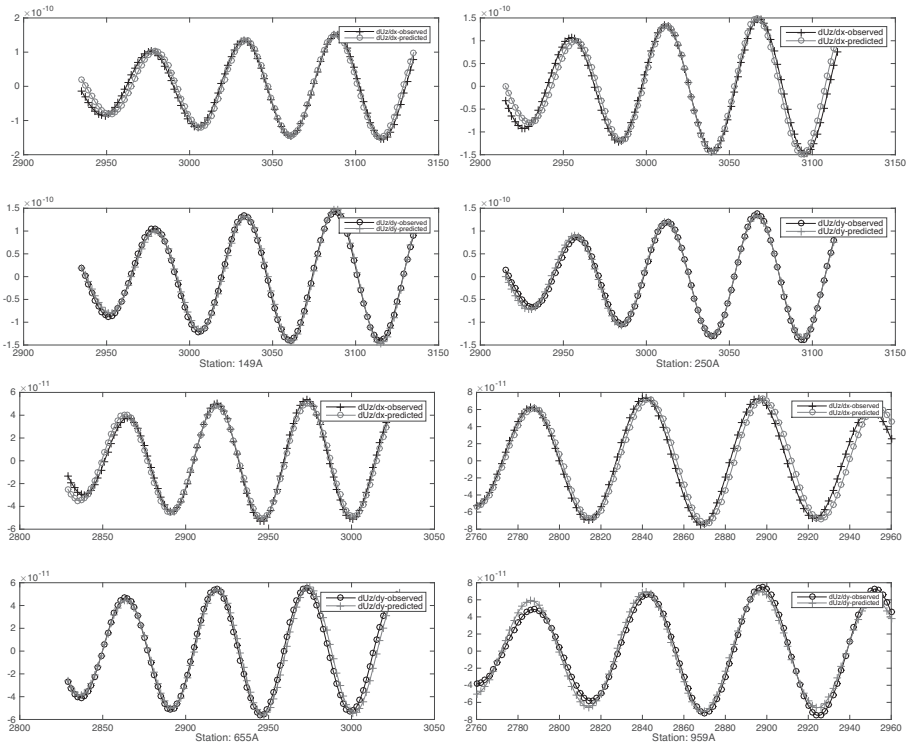

FIGURE 1.3: Observed spatial gradients of displacement field (black crosses) obtained from bi-cubic spline interpolation and the predicted spatial gradients (grey circles) using resolved $\vec{A}$ and $\vec{B}$-coefficients in equations (1.2) and (1.3), for 55 s Rayleigh wave recorded at TA stations: 149A, 250A, 655A and 959A.

found that this chosen spacing is adequate for providing a good match to the time series, along with stable displacement gradient estimates. For each event we analyzed, there are around 600 - 800 time series of straingrams (2 for each station) that are used to provide full gradiometry parameter estimates for the region covered. Figure 1.3 shows the typical match of the predicted and observed straingrams, where the predicted straingrams are determined using gradiometry coefficients (discussed in section 2.3 below).

The weighting matrix $V_{ij,kl}$, has an influence on the smoothing of model parameter estimates for interpolated displacements and inferred model displacement gradients. The weighting matrix is isotropic, which involves the assumption that the elastic medium has

a linear relation between stress and strain. The diagonal elements, controlled by a single adjustable parameter, have an influence on how close the displacement field is fit by the model. It is important not to over-fit the displacements, which can cause strain artifacts in the presence of significant noise. Thus, the size of the isotropic value is adjusted until a reduced chi-squared misfit between predicted and observed displacements reaches 1. This reduced chi-squared misfit depends on the size of the uncertainties in the displacement seismograms, which are unknown. After experimenting with a range of 0.1% - 10% of the maximum magnitude of displacement field for the displacement uncertainties, we assume that the displacements have an uncertainty of 0.5%. Higher assumed uncertainty in displacement yields a smoother solution. We have found with benchmarking tests (discussed in section 2.6) that we are able to best resolve phase velocity variations if we obtain a close match to displacement fields in the USArray data and that a choice of 0.5% works best for this. Such a low assumed error in displacement reflects the high quality of USArray data [*Liang and Langston*, 2009; *Lin et al.*, 2014; *Porritt et al.*, 2014].

1.2.3 Solving for $\vec{A}$ and $\vec{B}$-coefficients

Note that $\vec{A}$ and $\vec{B}$-coefficients define a continuous field, just as the spatial gradients of displacement field define a continuous field. From equations (1.2) and (1.3), we first set up the inversion problem in the time domain:

$$\boldsymbol{Gm} = \boldsymbol{d} \tag{1.13}$$

where $\boldsymbol{G}$ is the matrix for displacements and the time derivatives of the displacement fields, $\boldsymbol{m}$ contains the model coefficients $\vec{A}$ and $\vec{B}$ that we wish to solve for, and $\boldsymbol{d}$ contains the spatial gradients of displacement fields. The typical analysis time window is 200 s and the sampling is 2 s. Thus, the following system of equations can be applied to solve for A_x, A_y, B_x and B_y at each seismic station, using an iterative, damped least-squares inversion.

$$\begin{bmatrix} u|_{t_1} & \frac{\partial u}{\partial t}|_{t_1} \\ \vdots & \vdots \\ u|_{t_{101}} & \frac{\partial u}{\partial t}|_{t_{101}} \end{bmatrix} \times \begin{bmatrix} A_x \\ B_x \end{bmatrix} = \begin{bmatrix} \frac{\partial u}{\partial x}|_{t_1} \\ \vdots \\ \frac{\partial u}{\partial x}|_{t_{101}} \end{bmatrix} \quad \begin{bmatrix} u|_{t_1} & \frac{\partial u}{\partial t}|_{t_1} \\ \vdots & \vdots \\ u|_{t_{101}} & \frac{\partial u}{\partial t}|_{t_{101}} \end{bmatrix} \times \begin{bmatrix} A_y \\ B_y \end{bmatrix} = \begin{bmatrix} \frac{\partial u}{\partial y}|_{t_1} \\ \vdots \\ \frac{\partial u}{\partial y}|_{t_{101}} \end{bmatrix} \tag{1.14}$$

Examination of the fit to hundreds of straingrams like those in Figure 1.3 suggests that the assumptions in the first compatibility relation in equations (1.2) and (1.3) are effective in matching the spatial gradients of the wavefield for each master station.

Singular value decomposition (SVD) shows that the model eigenvector associated with the largest singular value points entirely in the $\vec{A}$-coefficient direction. The other model eigenvector points entirely in the $\vec{B}$-coefficient direction, and its singular value is generally 15 times smaller than the one associated with the $\vec{A}$-coefficients. Therefore, in general the slowness ($\vec{B}$-coefficients) will be more sensitive to errors in the spatial gradients. We have found that the variances for spatial gradients are close to constant for any given time step. Thus we assume that the data covariance: $\mathrm{cov}[\boldsymbol{d}] = \sigma^2 \cdot \boldsymbol{I}$, where σ^2 is the formal estimate for the variance of the spatial gradients and $\boldsymbol{I}$ is the identity matrix. Then the

following simplified equation is used to determine the model covariance matrix:

$$\mathrm{cov}[\boldsymbol{m}] = \sigma^2 \cdot \boldsymbol{V}_p \cdot (\boldsymbol{\lambda}^{-2}) \cdot \boldsymbol{V}_p^T \tag{1.15}$$

where $\boldsymbol{V}_p$ is the matrix containing model eigenvectors and $\boldsymbol{\lambda}$ is a diagonal matrix containing the model eigenvalues.

1.2.4 Solving for Structural Parameters

The phase velocity determined in conventional ray-based surface wave tomographic techniques, like the beam forming [*Birtill and Whiteway*, 1965] and two-station methods [*Knopoff et al.*, 1966; *Meier et al.*, 2004], is actually the local velocity of an individual wavefield based on the assumption of one dominate phase. This dynamic phase velocity, depends not only on the underlying medium, but also on the local geometry of the wavefield [*Wielandt*, 1993; *Friederich et al.*, 1995; *Pollitz and Snoke*, 2010]. *Wielandt* [1993] points out that the dynamic phase velocity cannot be directly attributed to the structure and cannot be used as an input for tomographic structure inversion. Neglecting this fact can systematically bias the structure interpretation [*Yang and Forsyth*, 2006; *Lin et al.*, 2009; *Pollitz and Snoke*, 2010]. The phase velocity in the Helmholtz equation is defined as the structural phase velocity, which is independent of specific geometry of the wavefield or source properties [*Wielandt*, 1993; *Friederich et al.*, 1995; *Lin and Ritzwoller*, 2011a]. Numerous theoretical and numerical studies [*Friederich et al.*, 2000; *Bodin and Maupin*, 2008; *Lin and Ritzwoller*, 2011a; *Jin and Gaherty*, 2015] have shown that, in most cases,

the dynamic phase velocity can differ substantially from the structural phase velocity for a single event. *Wielandt* [1993] showed that the solutions to the Helmholtz equation yield a local relationship: the deviation of the structural phase velocity from dynamic phase velocity depends on the first and second derivatives of logarithmic amplitude. *Lin and Ritzwoller* [2011a] and *Jin and Gaherty* [2015] both showed that surface wave tomography can be improved by using amplitude measurements to construct a geographically localized correction via the Helmholtz equation, which accounts for the finite frequency effects accurately, and this correction should at least be used at periods longer than 50 s for USArray TA stations [*Lin and Ritzwoller*, 2011a].

Lin et al. [2009] and *Lin and Ritzwoller* [2011a] addressed the solutions to the 2-D eikonal equation and the Helmholtz equation, respectively:

$$\frac{1}{c'(x,y)^2} = |\nabla\tau(x,y)|^2 \tag{1.16}$$

$$\frac{1}{c(x,y)^2} = |\nabla\tau(x,y)|^2 - \frac{\nabla^2 G(x,y)}{G(x,y)\omega^2} \tag{1.17}$$

where τ is the phase traveltime, G is the wave amplitude at location (x, y), the same as defined in equation (1.1), and ω is the angular frequency. Note that the Helmholtz equation is a second compatibility relation that we investigate, where the first compatibility relation involves equations (1.1), (1.2) and (1.3). The Helmholtz equation governs the propagation of most classical wavefields in homogeneous, isotropic media [*Wielandt*, 1993]. *Lin and Ritzwoller* [2011a] referred to c' as the apparent velocity (or dynamic

velocity) and c as the corrected velocity (or structural velocity). The difference between equations (1.16) and (1.17) is described by the Laplacian of the amplitude field normalized by the amplitude and square of the angular frequency. This amplitude Laplacian term [*Lin and Ritzwoller*, 2011a], permits a correct structural interpretation of surface waves in laterally homogeneous parts of the medium [*Wielandt*, 1993] .

Here we show that the gradiometry coefficients that we have solved for, can be used to approximate solutions for the Helmholtz equation for structural phase velocity. From equation (1.4), we know that the $\vec{A}$-coefficient corresponds to the gradient of logarithmic amplitude:

$$\vec{A} = \nabla \ln G = \frac{\nabla G}{G} \tag{1.18}$$

thus:

$$\vec{A}^2 + \nabla \cdot \vec{A} = (\frac{\nabla G}{G})^2 + \frac{\nabla^2 G \cdot G - (\nabla G)^2}{G^2} = \frac{\nabla^2 G}{G} \tag{1.19}$$

We have compared our phase velocity results with two separate results ([*Lin and Ritzwoller*, 2011a; *Jin and Gaherty*, 2015]) that used the same data sets (2009 Kuril Islands earthquake and 2007 Easter Island earthquake) and found a remarkable correspondence (discussed in section 2.5). The phase velocities determined from wave gradiometry $\vec{B}$-coefficients through equation (1.8) are almost identical to the dynamic phase velocities determined from the gradients of phase traveltime used in the Helmholtz tomography [*Lin and Ritzwoller*, 2011a]. Thus, we have determined empirically that use of equations (1.2) and (1.3) (the first compatibility relation) provides very similar estimates of wave

slowness to other studies that use gradient of phase traveltime methods [*Lin and Ritzwoller*, 2011a] and multi-channel cross-correlation methods [*Jin and Gaherty*, 2015]. In our investigation of the second compatibility relation in the Helmholtz equation solution (1.17), we make the assumption (based on this similarity with two other studies) that the $\vec{B}$-coefficient can be approximated as the local gradient of phase traveltime:

$$|\vec{B}| = |\vec{p}| \approx |\frac{1}{c}| = |\nabla \vec{\tau}| \tag{1.20}$$

But to be clear, we always relate the $\vec{B}$-coefficient to the local ray parameter as part of its original definition in equations (1.1), (1.2) (1.3) and (1.7). Furthermore, we have found a close match between $\nabla \cdot \vec{B}$ (obtained from the 2009 Kuril Islands event) and the focusing/defocusing correction term in *Lin et al.* [2012] (discussed in section 2.5). This further substantiates our assumption that $\nabla \cdot \vec{B}$ can be approximated as the Laplacian of phase traveltime:

$$\nabla \cdot \vec{B} \approx \nabla^2 \vec{\tau} \tag{1.21}$$

Combining equations (1.17), (1.19) and (1.20), the structural phase velocity is determined by subtracting the amplitude correction term [*Lin and Ritzwoller*, 2011a], involving $\vec{A}$, $\nabla \cdot \vec{A}$ and ω, from the dynamic phase velocity:

$$\frac{1}{c^2} \approx |\vec{B}|^2 - \frac{\vec{A}^2 + \nabla \cdot \vec{A}}{\omega^2} \tag{1.22}$$

In order to find $\nabla \cdot \vec{A}$, we interpolate the $\vec{A}$-coefficient vector field using the bi-cubic splines

[*Beavan and Haines*, 2001], which is the same method used to obtain spatial gradients from the displacement field. *Wielandt* [1993] argued that the amplitude correction term provides real constraints on the structural wavenumber. *Lin and Ritzwoller* [2011a] make these corrections to their estimates of gradient of phase traveltime measurements, and *Jin and Gaherty* [2015] also makes similar corrections to their estimates of local phase velocity. We have found a close match between our corrections compared to theirs for the same data sets (discussed in sections 2.5). However, before applying equation (1.22) to our gradiometry parameters, we assume that the acoustic Helmholtz equation remains approximately valid for elastic surface waves when the structure is slightly or smoothly inhomogeneous compared to the heterogeneity of the wavefield [*Wielandt*, 1993]. This is also born out by our gradiometry parameter results (see results in section 3.0 and summary in section 3.5).

We then address the transport equation [*Cerveny*, 2005] from the imaginary part of the solution to the 2-D Helmholtz equation:

$$2 \cdot \nabla\tau(x,y) \cdot \frac{\nabla G(x,y)}{G(x,y)} - \nabla^2\tau(x,y) = 0 \tag{1.23}$$

Substituting equations (1.18), (1.20) and (1.21) into (1.23) gives us:

$$2 \cdot \vec{B} \cdot \vec{A} - \nabla \cdot \vec{B} = 0 \tag{1.24}$$

The first and second terms in the above equation are defined as "apparent amplitude

decay" and "focusing/defocusing correction term", respectively [*Lin et al.*, 2012]. We observe generally positive correlations between these two terms (Figure 1.4), in accord with the relation in equation (1.24). Furthermore, *Lin et al.* [2012] have used these terms to constrain local amplification factors in the western U.S. regions, which can be used to constrain density variations.

An inspection of gradiometry parameters for 2013 October 12, earthquake near Crete, shows an interesting pattern in relation to regional amplitude variations. The $\vec{A}$-coefficients in Figure 1.5a, obtained from least-squares inversion of equations (1.2) and (1.3), show patterns that are in accord with spatial variations of amplitudes in Figure 1.5b, which makes sense because the $\vec{A}$-coefficients represent the gradient of logarithmic amplitude. These vectors point towards amplitude highs and away from amplitude lows. Note that the $\vec{A}$-coefficient vector fields in Figure 1.5a do not result from taking derivatives of the static maximum amplitudes plotted in Figure 1.5b. Instead these estimates arise from inversion of spatial gradients of displacement field for all time steps at each individual station. The correlation described above, however, provides confirmation that our method for estimating the coefficients from the spatial derivatives of the wavefield is robust.

The Laplacian of logarithmic amplitude ($\nabla \cdot \vec{A}$, contoured in Figure 1.5a), is used in the approximate solution to the Helmholtz equation (1.22). The $\vec{B}$-coefficients (vector field in Figure 1.5c) point opposite to the wave propagation direction ($\vec{B} = -\vec{p}$). Note that this vector field shows systematic bending in places, reflecting focusing and defocusing of energy. Furthermore, $\nabla \cdot \vec{B}$ (contoured in Figure 1.5c) can be further used in solutions to the Helmholtz equation for laterally varying media in both velocity and density (described

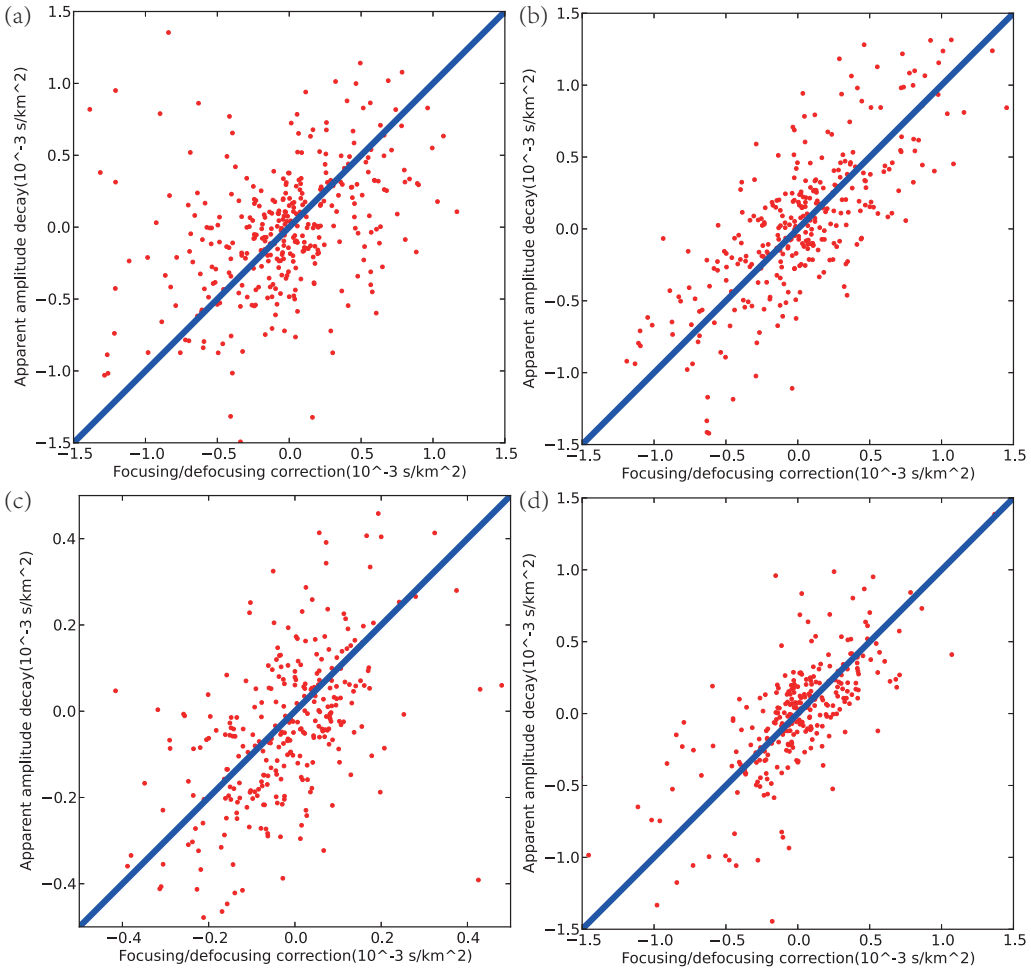

FIGURE 1.4: The correlation between the apparent amplitude decay $(2 \cdot \vec{A} \cdot \vec{B})$ and the focusing/defocusing correction term $(\nabla \cdot \vec{B})$ in the transport equation (1.24) for 55 s Rayleigh wave, where each red dot denotes the result at a station. The blue line is the best fitting straight line. (a) 2013 October 25, earthquake near Honshu ($M_w = 7.3$) (b) 2014 February 2, earthquake near Kermadec Island ($M_w = 6.6$) (c) 2014 March 16, earthquake near Chile ($M_w = 6.7$) (d) 2014 May 24, earthquake in Aegean Sea ($M_w = 6.9$).

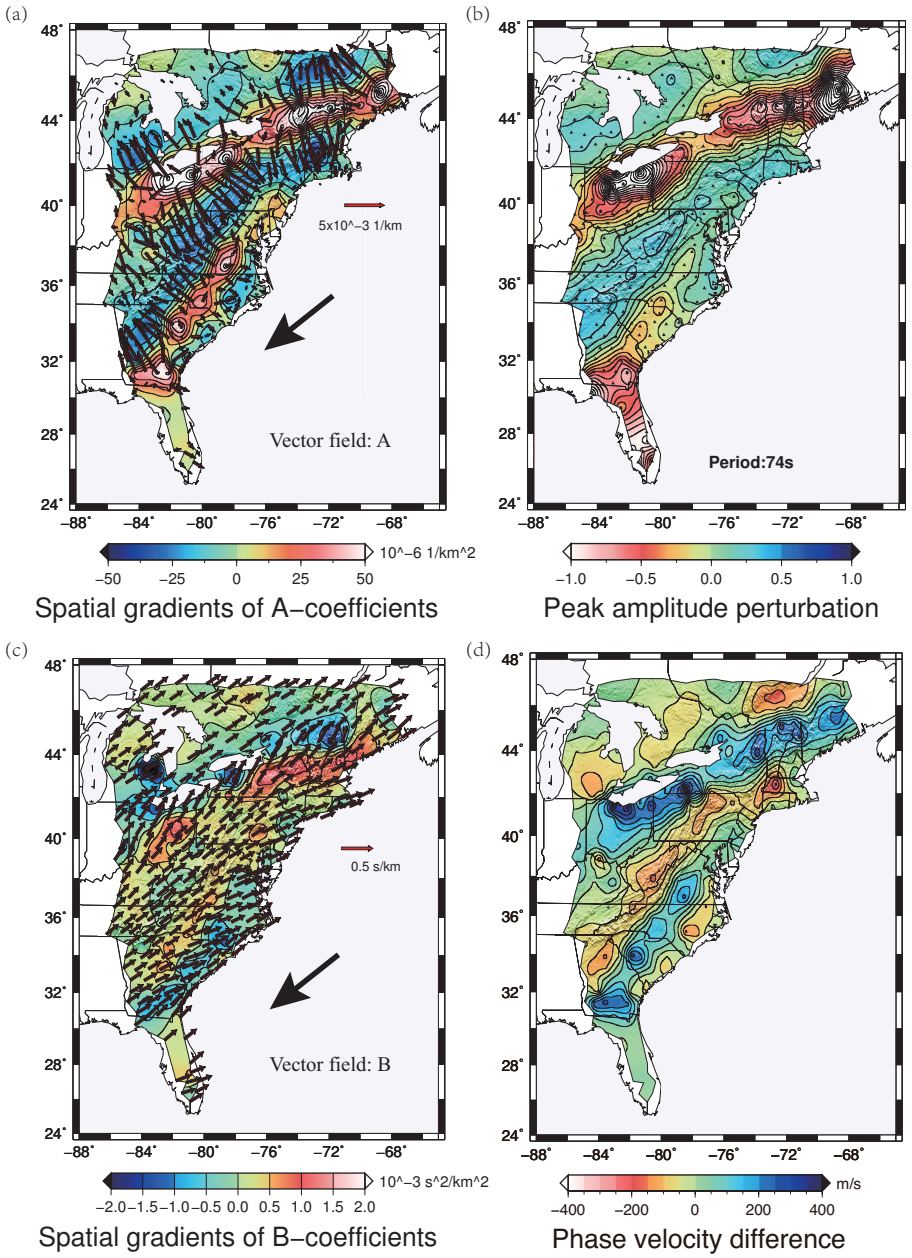

FIGURE 1.5: The vectors in (a) and (c) represent the $\vec{A}$-coefficients (gradients of logarithmic amplitude) and the $\vec{B}$-coefficients field (horizontal slowness), respectively, for 74 s Rayleigh wave from 2013 October 12 earthquake near Crete. The contours correspond to $\nabla \cdot \vec{A}$ (Laplacian of logarithmic amplitude) and $\nabla \cdot \vec{B}$, which are separated by intervals of $25 \times 10^{-6} km^{-2}$ and $0.5 \times 10^{-3} s^2/km^2$, respectively. Note that the $\vec{A}$-coefficient vectors generally point along steepest gradient towards amplitude highs and away from amplitude lows, and the $\vec{B}$-coefficient vectors point opposite to wave propagation direction, which show systematic deflection of energy. The arrow indicates the approximate ray path.(b) The peak amplitude perturbation for Rayleigh wave phase. The stations are shown as triangles. (d) Dynamic and structural phase velocity differences, calculated from amplitude correction terms in equation (1.22).

below). We will show later that $\nabla \cdot \vec{B}$ have a strong correlation with changes in geometrical spreading. The amplitude correction term that depends on the $\vec{A}$-coefficients and $\nabla \cdot \vec{A}$ in Figure 1.5a, can result in a velocity difference between dynamic and structural phase velocity as high as 0.4km/s (Figure 1.5d).

The blue areas in Figure 1.5a shows locations where the amplitudes have maximum relative values. In such areas, $\vec{A} = 0$ and $\nabla \cdot \vec{A} < 0$, and the amplitude correction term yields a structural phase velocity less than dynamic phase velocity (red areas in Figure 1.5d). In the red areas of Figure 1.5a, where the amplitudes have minimum relative values, we have $\vec{A} = 0$ and $\nabla \cdot \vec{A} > 0$, and the amplitude correction term yields a structural phase velocity greater than dynamic phase velocity (blue areas in Figure 1.5d) [*Wielandt*, 1993].

Figure 1.6 shows the probability density functions, mean value and standard deviation for dynamic and structural phase velocity results at two TA stations. The distribution of structural phase velocities are generally more concentrated than the dynamic phase velocities, which may reflect the reduction of local wavefield geometry effects and random noise bias [*Lin and Ritzwoller*, 2011a].

If both the phase velocity and the density are variable in a medium, the equivalent solutions to the Helmholtz equation for the acoustic case in such medium are:

$$\frac{1}{c^2} = |\vec{B}|^2 - \frac{\vec{A}^2 + \nabla \cdot \vec{A} - \vec{A} \cdot \nabla(\ln \rho)}{\omega^2} \tag{1.25}$$

$$2 \cdot \vec{B} \cdot \vec{A} - \nabla \cdot \vec{B} = \vec{B} \cdot \nabla(\ln \rho) \tag{1.26}$$

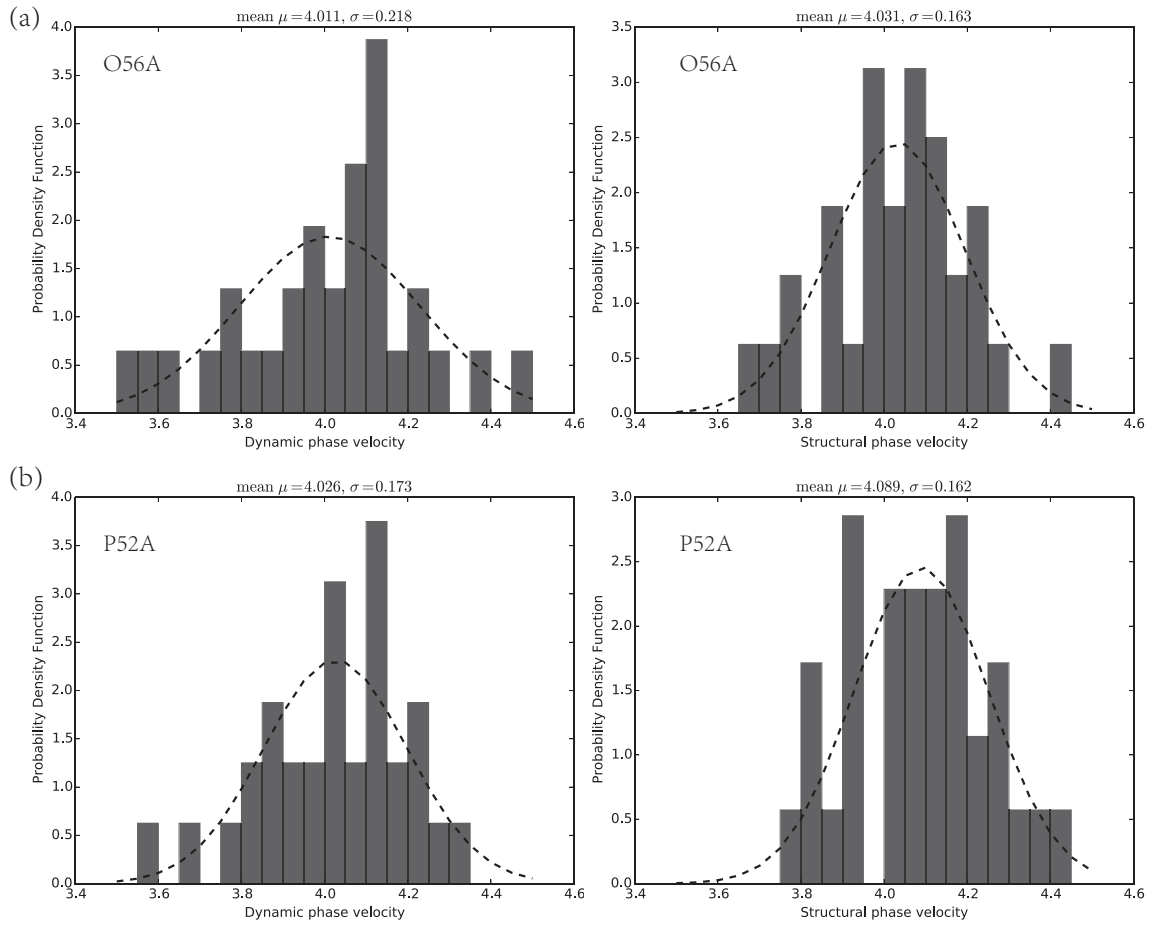

FIGURE 1.6: Percentage density function for 55 s Rayleigh wave dynamic and structural phase velocity at TA stations O56A (a) and P52A (b). The mean velocity and standard deviation are also shown. The dashed lines indicate Gaussian fitting curves.

This enables us to estimate the density by integrating in the direction of wave propagation [*Wielandt*, 1993]. Thus in the future the gradiometry coefficients and the divergence of these coefficients (Figures 1.5a, 1.5c) can be used to obtain constraints on density variations when considering the acoustic case.

1.2.5 Benchmarking

We have experimented with two events: 2009 April 7, earthquake near Kuril Islands and 2007 February 14, earthquake near Easter Island, for 60 s Rayleigh wave. The close match between $\nabla \cdot \vec{B}$ (contoured in Figure 1.7a, 1.8a) and the focusing/defocusing maps in *Lin et al.* [2012] supports the approximate relation in equations (1.20) and (1.21). The patterns in amplitude Laplacian terms we obtain for both events (Figure 1.7b and 1.8b) are also quite similar to results from *Lin and Ritzwoller* [2011a] and *Jin and Gaherty* [2015], and we thus share similar amplitude correction terms. Both the dynamic and structural phase velocity maps (Figure 1.7c, 1.7d and 1.8c, 1.8d) obtained using wave gradiometry parameters show very close consistencies with the results from *Lin and Ritzwoller* [2011a] and *Jin and Gaherty* [2015] for the same data sets, which they obtain using different methods (Helmholtz tomography and multi-channel cross-correlation method). Small differences (less than 10%) can be attributed to the possible differences in estimation of spatial derivatives of the amplitude field.

The least-squares inversion requires a starting model. To find out how the starting velocity influences our final result, we have applied another two starting phase velocities (3.8 km/s and 4.2 km/s) to 60 s Rayleigh waves for Kuril Islands event. After four

iterations, both the dynamic and structural velocity maps (Figure 1.9) are nearly identical to the ones starting with 4.0 km/s (Figure 1.7c, 1.7d). This confirms that the final solution for gradiometry parameters is not sensitive to the starting velocity guess.

For periods less than 40 s, there is a possibility of spatial aliasing of the wavefield because there are fewer than two stations covering the wavelength dimension. We have experimented with different starting velocities (3.4 km/s, 3.6 km/s and 3.8 km/s) for 20 s period Rayleigh waves and found only slight sensitivity for velocity results to starting model guess. However, for periods less than 40 s we do see that the gradients of logarithmic amplitude estimates ($\vec{A}$-coefficients) are generally not as smooth as for longer period results, although similar trend distributions are still observed for these shorter periods (discussed in section 2.6). Spatial variations in amplitudes must be more than twice the station spacing (140 km) in order to be smoothly resolved. We will show later that our isotropic velocity results for short periods 20 - 40 s agree well with results from *Jin and Gaherty* [2015].

1.2.6 Data Processing

We select teleseismic earthquakes with M_w larger than 6.0 and focal depth shallower than 50 km from IRIS Data Management Center. Earthquakes with significant-sized aftershocks that followed within less than one hour of the main shock are not analyzed to avoid Rayleigh phase interferences. Only vertical component seismograms are analyzed, because they are not contaminated by Love wave or higher mode Rayleigh waves, and

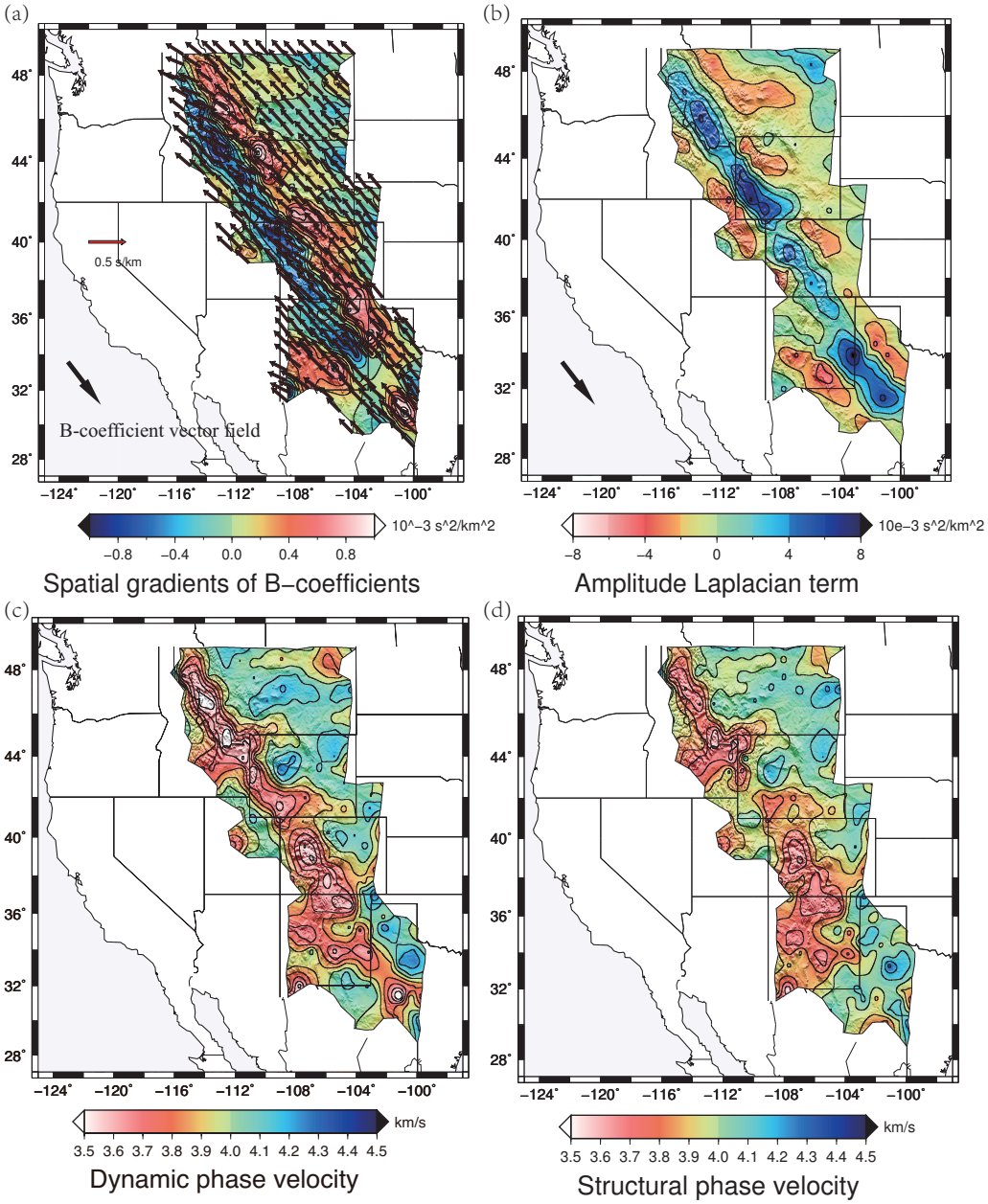

FIGURE 1.7: (a) $\vec{B}$-coefficient vector fields, along with contoured $\nabla \cdot \vec{B}$ for 60 s Rayleigh wave from 2009 April 7, earthquake near Kuril Islands ($M_w = 6.8$). Contours are separated by intervals of $0.2 \times 10^{-3} s^2/km^2$.(b) Amplitude Laplacian term in equation (1.17), calculated from $\vec{A}$-coefficient field and its first derivative. Contours are separated by intervals of $2 \times 10^{-3} s^2/km^2$. (c)(d) Dynamic (apparent) and structural (corrected) phase velocity maps. Contours are separated by intervals of 0.1 km/s.

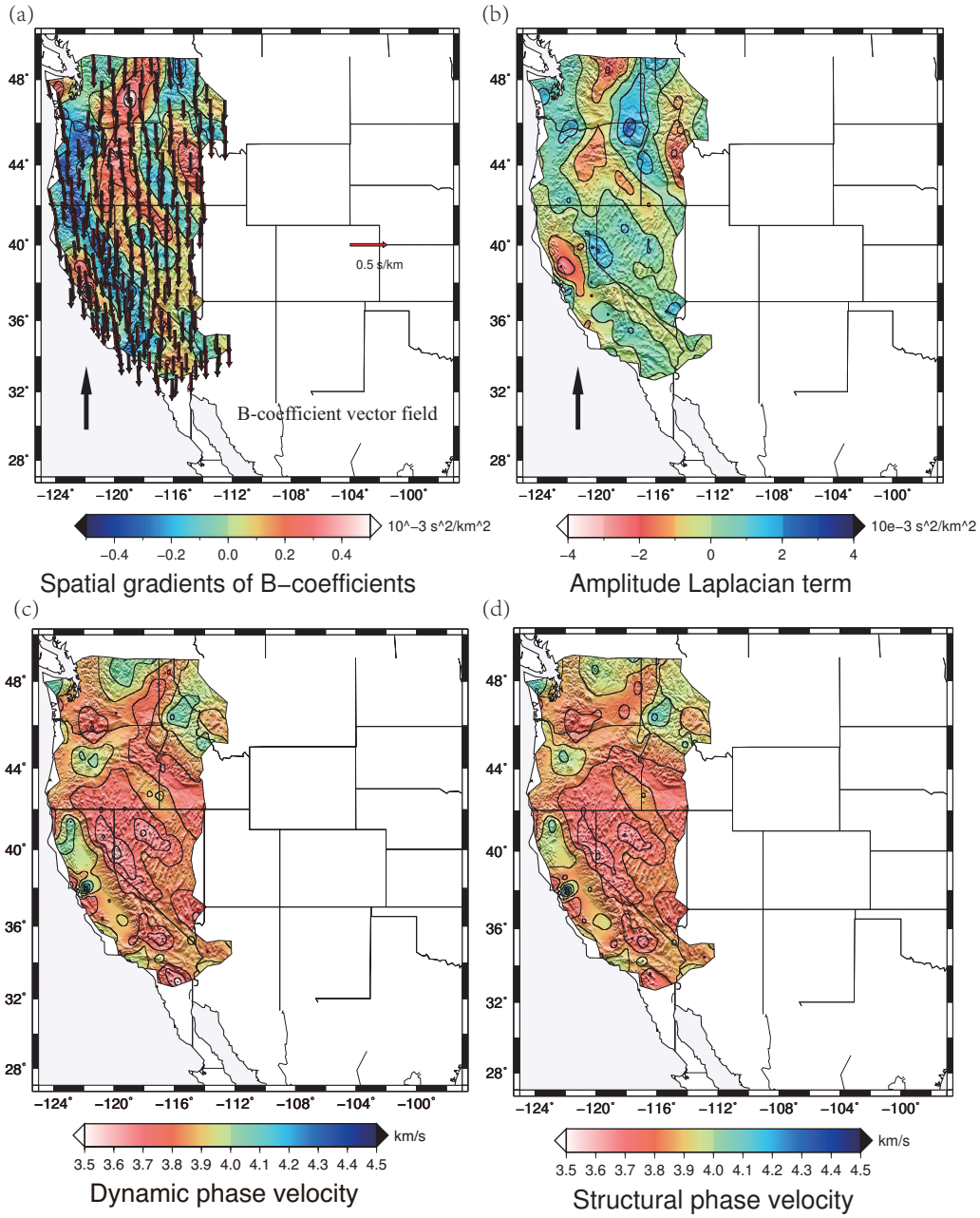

FIGURE 1.8: The same with Figure 1.7 but for the 2007 February 14, earthquake near Easter Island ($M_w = 5.7$).

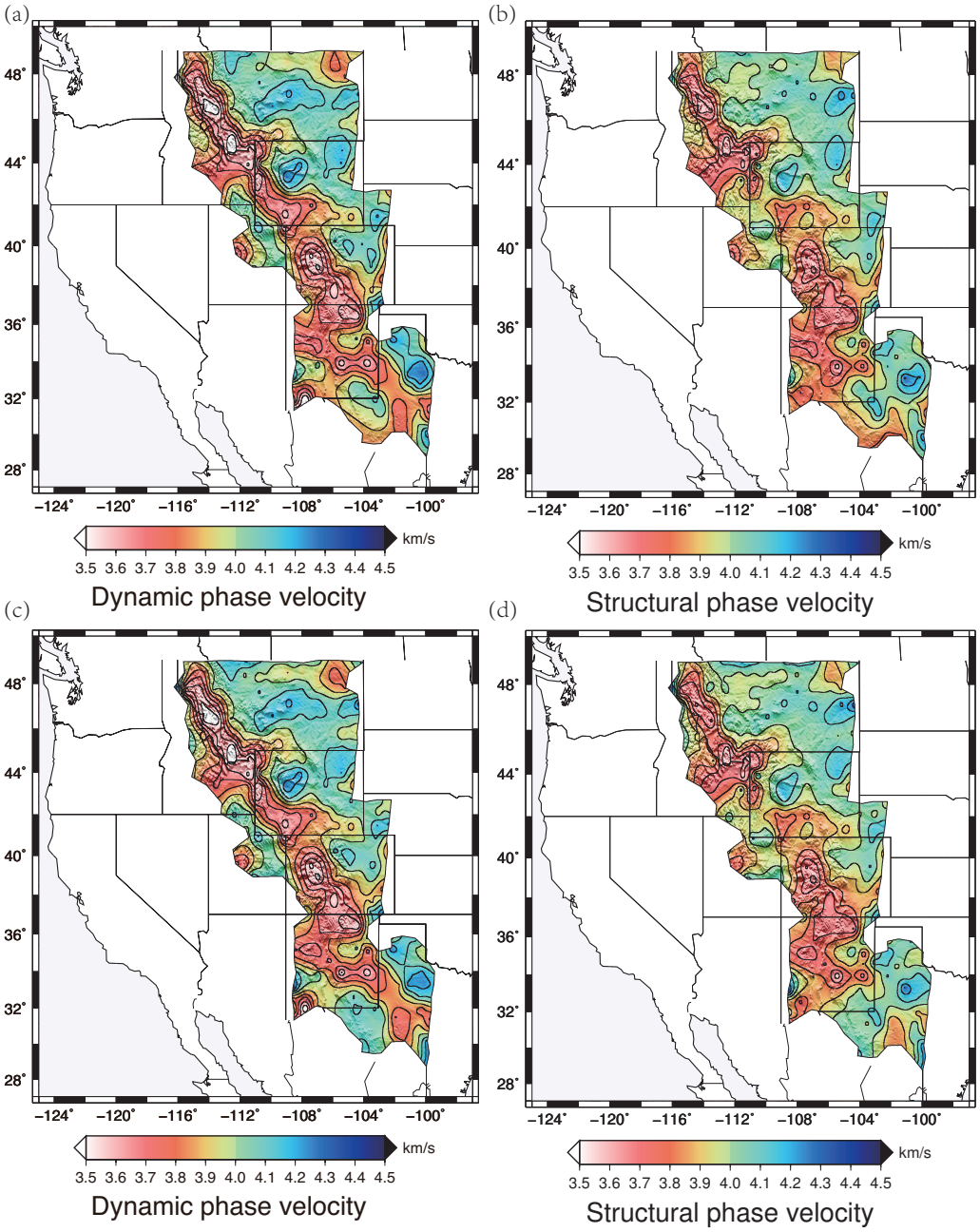

FIGURE 1.9: Dynamic and structural phase velocity maps for 60 s Rayleigh wave from earthquake near Kuril Islands, using 3.8 km/s (a, b) and 4.2 km/s (c, d) as starting phase velocity, respectively. Contours are separated by intervals of 0.1 km/s.

the noise levels are typically lower than horizontal components [*Friederich et al.*, 1995; *Yang and Forsyth*, 2006].

The broadband seismograms for each event are processed with the following procedures: [1] discard waveforms with the largest displacements more than 2 standard deviations beyond the mean values; [2] remove instrumental response, wave trends and means; apply narrow bandpass filters to the displacement waveforms for 15 passbands with center periods ranging from 20 s to 150 s; [3] examine the waveforms and make sure the Rayleigh phase is clean and strong; [4] upload data to XSEDE parallel computing center [*Towns et al.*, 2014]; [5] generate 200 s time window for analysis based on Rayleigh phase arrival time ; [6] remove subarrays with less than 5 supporting stations and apply reducing velocity method to shift waveforms within each subarray; [7] obtain the displacements, the spatial gradients and the time derivatives of displacement field, [8] invert for $\vec{A}$ and $\vec{B}$-coefficients using least-squares inversion; [9] use the iterated velocity as a new reducing velocity and repeat processes from steps [6] to [8] until the velocity differences between the two successive loops are smaller than 0.01 km/s [*Liang and Langston*, 2009]; [10] interpolate the $\vec{A}$ and $\vec{B}$-coefficient fields to estimate the amplitude correction and focusing/defocusing terms, respectively; [11] calculate the structural phase velocity, back-azimuth, radiation pattern, and geometrical spreading; [12] estimate structural phase velocity standard deviation from formal error estimates of spatial gradients of displacement field and $\vec{B}$-coefficients [*Aster et al.*, 2011]; [13] stack structural phase velocity results from all events for isotropic phase velocity maps.

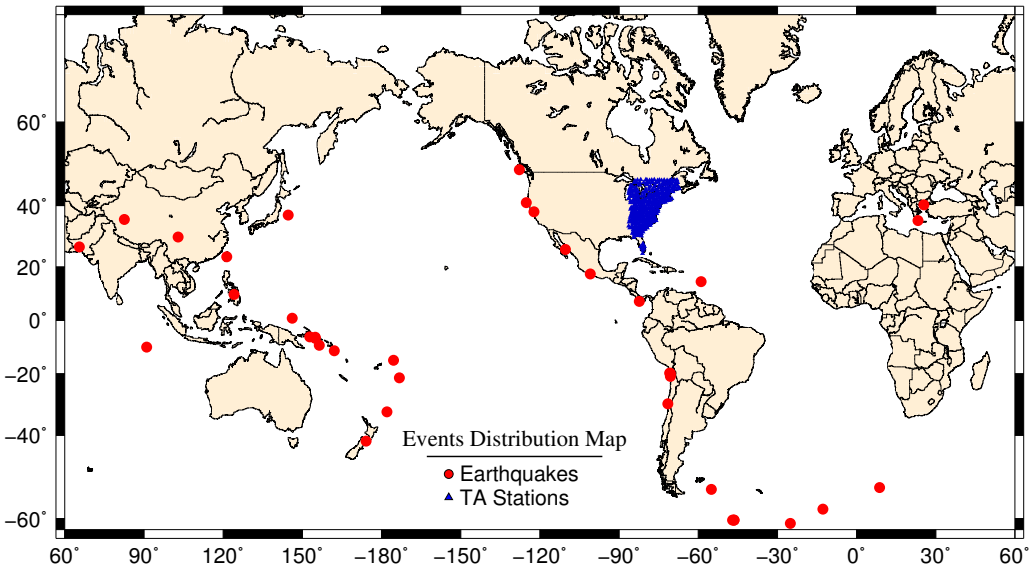

FIGURE 1.10: Earthquakes and USArray TA stations distribution map. The red dots mark the earthquake locations and the blue triangles indicate the USArray TA Stations.

1.3 Gradiometry Results

Seismic records from 37 earthquakes are processed for around 450 USArray TA stations in the eastern U.S. (Figure 1.10, partial list in Table 1.1). The wave gradiometry method is only applied to Rayleigh waves here, but it can also be applied to Love waves, or even body waves [*Liang and Langston*, 2009; *Sun and Helmberger*, 2011; *Jin and Gaherty*, 2015].

The results of wave gradiometry parameters for four events are presented in Figure 1.11 and 1.12. Vector fields and contours in Figure 1.11 represent the $\vec{A}$-coefficients (gradient of logarithmic amplitude) and $\nabla \cdot \vec{A}$ (Laplacian of logarithmic amplitude), respectively. The $\vec{A}$-coefficients are associated with amplitude variations across space (geometrical spreading and radiation pattern), which can provide information related to focusing and defocusing of energy [*Dahlen and Tromp*, 1998; *Liang and Langston*, 2009].

TABLE 1.1: Partial seismic events used in this project.

Time	Lat	Lon	Depth	Mag	Location	Stations
2013/04/20	30.31	102.89	14.0	6.6	Sichuan	346
2013/07/15	-60.86	-25.07	11.0	7.3	Sandwich	331
2013/09/24	26.97	65.52	15.0	7.7	Pakistan	357
2013/10/12	35.51	23.25	40.0	6.6	Crete	363
2013/10/25	-13.71	166.51	35.0	7.3	Honshu	353
2013/10/31	23.59	121.44	10.0	6.6	Taiwan	365
2013/11/16	-60.26	-47.06	9.9	6.8	Scotia	362
2013/11/17	-60.27	-46.40	10.0	7.7	Scotia	350
2013/11/25	-53.95	-55.00	11.8	7.0	Falkland	358
2014/02/02	-32.91	-177.88	44.3	6.6	Kermadec	328
2014/02/12	37.16	144.66	12.4	6.8	Xizang	369
2014/05/24	40.29	25.39	6.4	6.9	Aegean	370
2014/07/04	-6.23	152.81	20.0	6.5	Britain	267
2014/08/24	-122.31	38.22	11.3	6.0	Napa	234
2014/09/04	-173.26	-21.40	11.8	6.0	Tonga	246

The vector fields and contours in Figure 1.12 represent the $\vec{B}$-coefficients (local wave slowness) and $\nabla \cdot \vec{B}$, respectively. From transport equation (1.24), when $\nabla \cdot \vec{B}$ is relatively small, $\vec{A}$ and $\vec{B}$-coefficient vectors must be orthogonal to each other [*Wielandt*, 1993]. We indeed find that the $\vec{A}$-coefficients (Figure 1.11) are in general perpendicular to the $\vec{B}$-coefficients (Figure 1.12), except in regions with large values of $\nabla \cdot \vec{B}$, where we argue that wavefields are either focusing or defocusing. $\vec{A}$-coefficient vectors diverge (positive values of Laplacian of logarithmic amplitude) from regions of low relative amplitude and converge toward regions of higher relative amplitude (negative values of Laplacian of logarithmic amplitude in Figure 1.11). The large variations of the $\vec{A}$ and $\nabla \cdot \vec{A}$ are attributed to high amplitude change across space, since they involve the derivatives of logarithmic amplitudes.

We also show the $\vec{A}$ and $\vec{B}$-coefficient fields for 20 s Rayleigh waves obtained from two

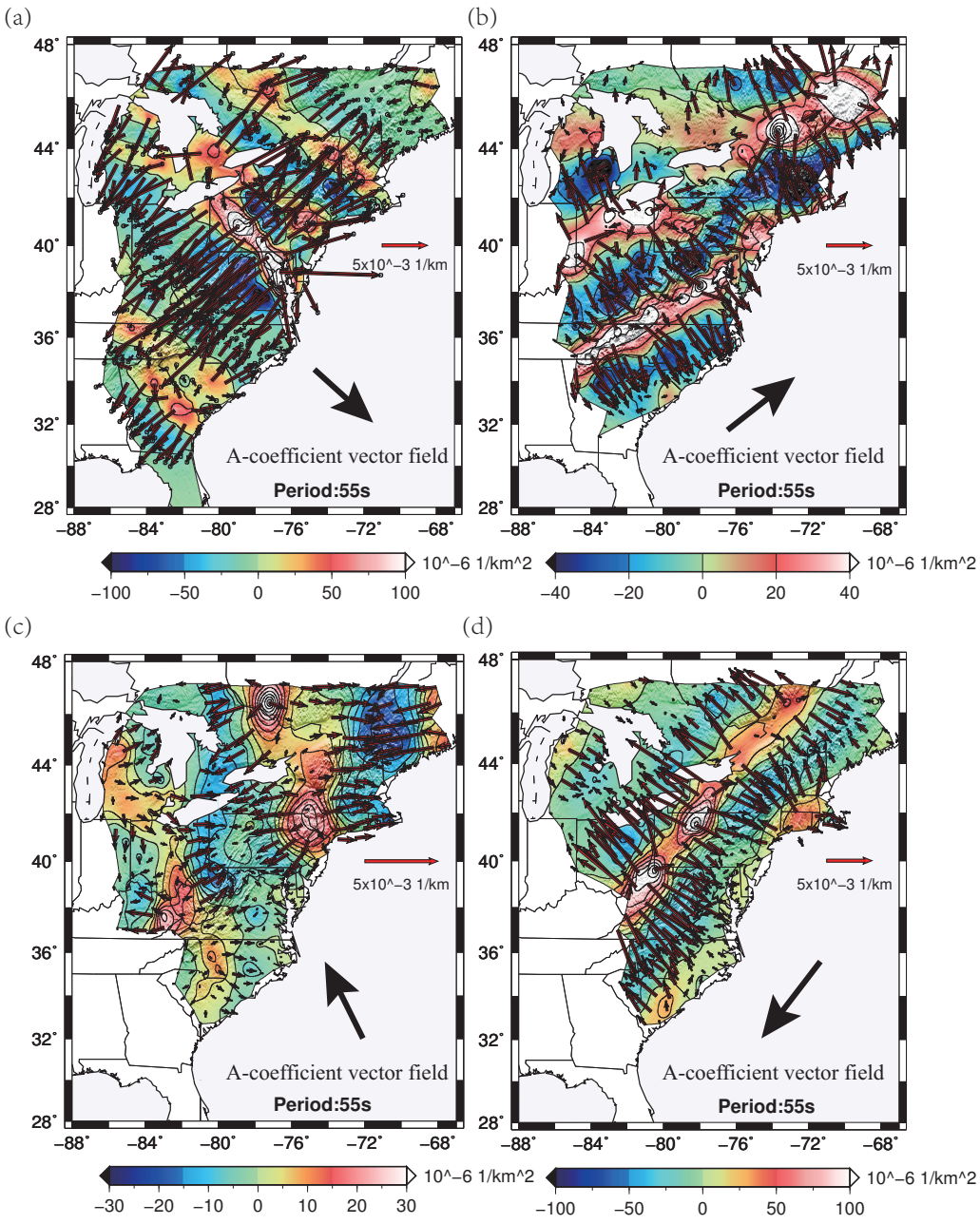

FIGURE 1.11: Vector fields are associated with $\vec{A}$-coefficients and contours show $\nabla \cdot \vec{A}$ for 55 s Rayleigh wave from (a) 2013 October 25, earthquake near Honshu (b) 2014 February 2, earthquake near Kermadec Island (c) 2014 March 16, earthquake near Chile (d) 2014 May 24, earthquake in Aegean Sea. The large black arrows show approximate ray paths.

events we analyzed earlier (Figure 1.13). Both vector fields show characteristics similar to 55 s period energy, though not as smooth as the latter. Namely, the $\vec{A}$-coefficients are generally orthogonal to the $\vec{B}$-coefficients. The Laplacian of logarithmic amplitudes ($\nabla \cdot \vec{A}$) show trends roughly parallel to the direction of energy propagation and peak values of the Laplacian correspond to amplitude minima and maxima (Figure 1.13a, 1.13c). Peak values of Laplacian of logarithimic amplitude also show regions where major focusing and defocusing of energy occurs (coincident with deflections of $\vec{B}$-coefficient in Figure 1.13b, 1.13d). These spatial variations in peak-to-peak amplitude are apparently captured by USArray TA stations spacing (70 km) for 20 s energy. The reason for this is that the length scales of peak-to-peak amplitude variations (measured orthogonal to propagation direction) are generally captured by more than four TA stations. The systematic deflection of $\vec{B}$-coefficient is constrained over distances of only one station spacing along a trend line connecting central New Jersey to eastern Kentucky (Figure 1.13d), and this deflection is consistent with a closely adjacent ridge along the same trend where there are major amplitude lows.

Similar to *Liang and Langston* [2009], we show four wave propagation parameters: phase velocity, radiation pattern, geometrical spreading and back-azimuth variation for the same events. These events show a range of source azimuths, but represent typical behaviors observed for most events. We have advanced the gradiometry method to explore approximate solutions to the Helmholtz equation, which provide estimates of the structural phase velocity. Estimates of structural phase velocities differ substantially for some regions, obtained from different events (Figure 1.14a, 1.15a, 1.16a, 1.17a), which is

commonly observed with surface wave analysis [*Liang and Langston*, 2009; *Lin and Ritzwoller*, 2011a]. The heterogeneous structure along the ray path may introduce strong phase velocity discrepancies for earthquakes coming from different azimuths [*Lin and Schmandt*, 2014]. However, the azimuthal variation in phase velocities obtained here can provide constraints for azimuthal anisotropy within this region. Furthermore, the presence of anisotropy can produce complexity in the wavefield [*Park and Yu*, 1993; *Yang and Forsyth*, 2006; *Lin and Schmandt*, 2014], and wave gradiometry methods may hold promise for yielding insight into these effects.

1.3.1 October 25, 2013 M_w=7.3 Honshu Event

The Honshu event of October 25, 2013 involves a back-azimuth from the northwest. The radiation patterns in Figure 1.14b show a distribution of ridges that run roughly parallel to the ray path direction. This can be understood by examining Figure 1.11a, which shows gradients of logarithmic amplitude ($\vec{A}$-coefficients) that are in general orthogonal to propagation direction. Where the $\vec{A}$-coefficient vectors show components that are not orthogonal to the propagation direction, one expects to observe a non-zero value of geometrical spreading, and by transport equation (1.24) we expect to see non-zero values for $\nabla \cdot \vec{B}$ for these regions. Indeed we observe a very close positive correlation between the geometrical spreading in Figure 1.14c and $\nabla \cdot \vec{B}$ in Figure 1.12a. Positive values of $\nabla \cdot \vec{B}$ highlight regions where the vectors show some divergence, corresponding to curvature of the wavefront. However, because the $\vec{B}$-coefficients point opposite to the direction of wave propagation, positive values for $\nabla \cdot \vec{B}$ represent regions where the energy is converging

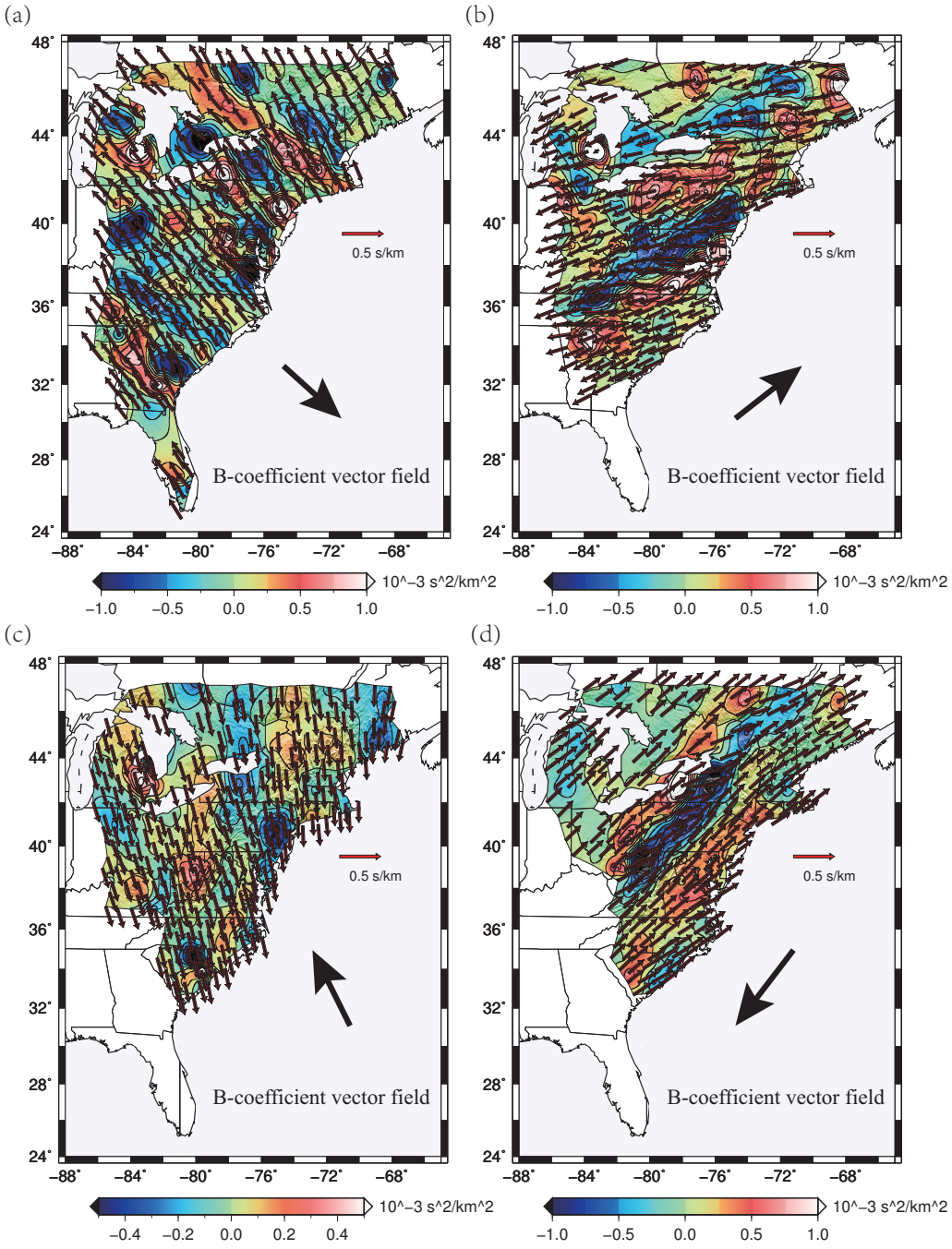

FIGURE 1.12: Vector fields are associated with $\vec{B}$-coefficients and contours show $\nabla \cdot \vec{B}$ for 55 s Rayleigh wave from the same earthquakes in Figure 1.11.

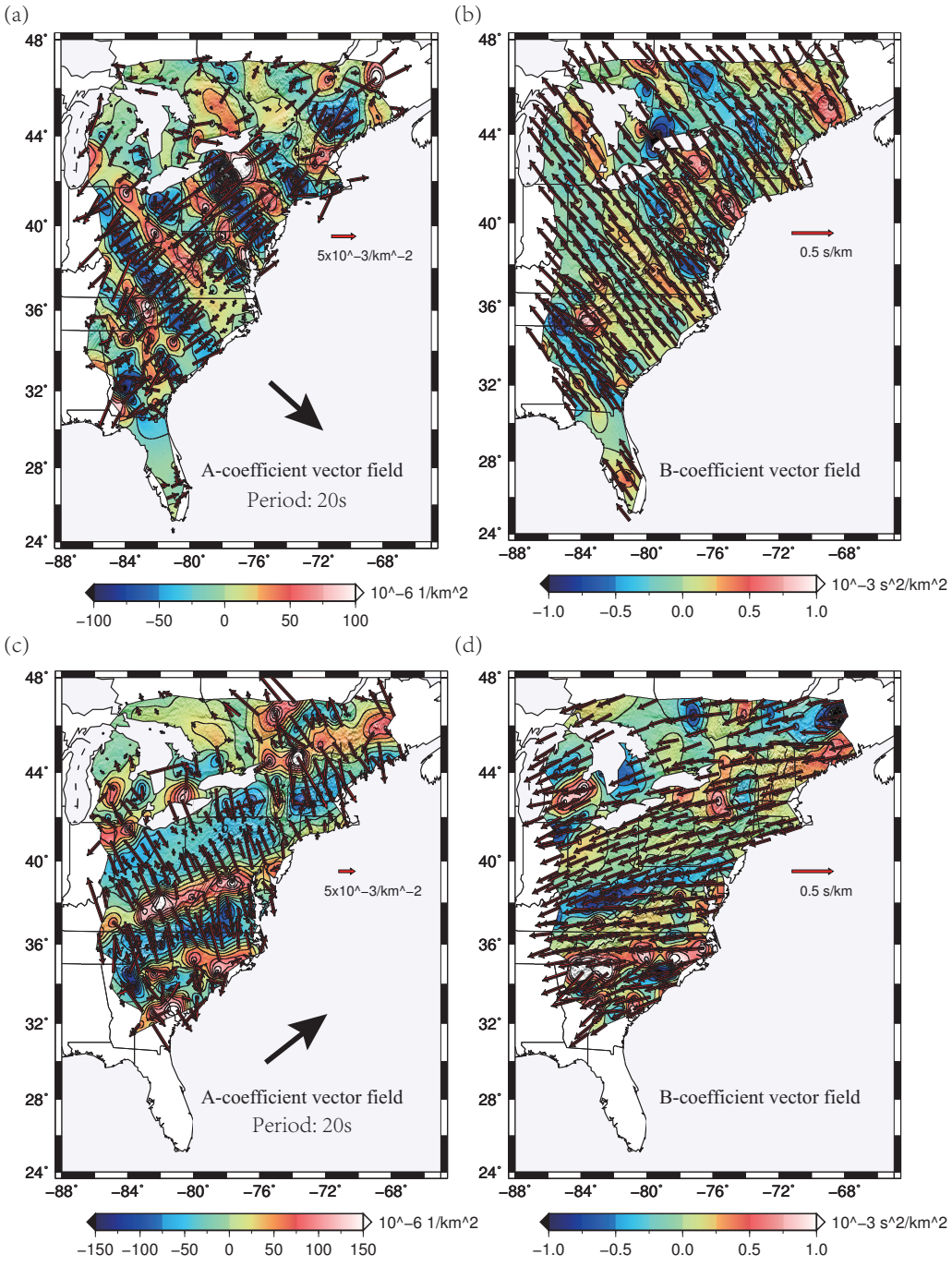

FIGURE 1.13: (a,c) Vector fields are associated with $\vec{A}$-coefficients and contours show $\nabla \cdot \vec{A}$ for 20 s Rayleigh wave from 2013 October 25, earthquake near Honshu and 2014 February 2, earthquake near Kermadec Island, respectively. (b,d) Vector fields are associated with $\vec{B}$-coefficients and contours show $\nabla \cdot \vec{B}$ for the same events in (a,c).

or focusing and negative values represent regions where the energy is defocusing (Figure 1.12a). It is known that heterogeneous structure results in off great circle arrivals [*Evernden*, 1954]. The back-azimuth variation ($-30°$ to $30°$) in Figure 1.14d can be compared with $\vec{B}$-coefficient vectors in Figure 1.12a to show whether energy is arriving clockwise or anti-clockwise to the expected great circle path [*Liang and Langston*, 2009; *Foster et al.*, 2013]. In general, the geometrical spreading (Figure 1.14c) and $\nabla \cdot \vec{B}$ (Figure 1.12a) are both anti-correlated with the Laplacian of logarithmic amplitude (Figure 1.11a) for most regions. Within regions of energy focusing (i.e., the positive northwest trending band in the U.S. Northeast and Canada (Figure 1.12a, 1.14c), we observe negative values for Laplacian of logarithmic amplitude (Figure 1.11a), which corresponds to areas of amplitude highs. Within regions of energy defocusing, we generally observe positive values for Laplacian of logarithmic amplitude.

1.3.2 February 2, 2014 M_w=6.6 Kermadec Island Event

The event of February 2, 2014 from Kermadec Island has a back-azimuth from the southwest. The Laplacian of logarithmic amplitude (Figure 1.12b) and the radiation pattern (Figure 1.15b) both show strong banding with trends that are primarily parallel to propagation direction, which suggests that amplitude variations are dominantly orthogonal to propagation direction. The geometrical spreading (Figure 1.15c) again shows a strong correlation with $\nabla \cdot \vec{B}$ (Figure 1.12b), and they are both anti-correlated with the Laplacian of logarithmic amplitude (Figure 1.11b). For example, there is a strong positive band of Laplacian of logarithmic amplitude extending from eastern Tennessee, trending

northeast up into Maryland and southern New Jersey. Examination of Figures 1.12b and 1.15c shows that there is a strong defocusing of energy (negative values for geometrical spreading (Figure 1.15c) and $\nabla \cdot \vec{B}$ (Figure 1.12b) along this band). Note that path directions are also directed clockwise (Figure 1.15d)) of expected great circle directions along this band. This deflection of energy clockwise, the negative values for geometrical spreading and $\nabla \cdot \vec{B}$, the positive values for Laplacian of logarithmic amplitude, and the amplitude lows, are all consistent with defocusing along this trend.

1.3.3 March 16, 2014 M_w=7.0 Chile Event

The March 16, 2014 Chile earthquake has a back-azimuth from the southeast and again shows similar banding patterns for Laplacian of logarithmic amplitude (Figure 1.11c) and the radiation pattern (Figure 1.16b) that suggest strong gradients in amplitude orthogonal to propagation direction. In north and northwest of New Jersey regions, $\nabla \cdot \vec{B}$ is extremely low (Figure 1.12c), where the geometrical spreading is negative (Figure 1.16c), and the Laplacian of logarithmic amplitude is strongly positive (Figure 1.11c), which suggests a strong defocusing of energy.

1.3.4 May 24, 2014 M_w=6.9 Aegean Sea Event

The event of May 24, 2014 in Aegean Sea shows a back-azimuth of energy from the northeast. This event may present the most compelling correlation of geometrical spreading (Figure 1.17c) with $\nabla \cdot \vec{B}$ (Figure 1.12d), covering the region from West Virginia to northern New York. Negative values for $\nabla \cdot \vec{B}$ indicates a strong defocusing of energy along

this belt, where there are strong positive values for Laplacian of logarithmic amplitude in Figure 1.11d, or amplitude minima.

1.3.5 Summary from Gradiometry Analysis of Individual Events

In summary, gradiometry parameters provide a rich field of information for each event. A consistent pattern observed to date involves amplitude variations that are primarily in directions orthogonal to wavefield propagation direction. The remarkable correlation between geometrical spreading and $\nabla \cdot \vec{B}$, predicted by transport equation (1.24), suggests a self-consistent link between the $\vec{A}$ and $\vec{B}$-coefficients that yield information on characteristics of the wavefield, such as where focusing and defocusing of energy is occurring, and how it is linked with azimuth of arriving energy and amplitude variations. The apparent satisfaction of equation (1.24) provided by these several examples of observed wavefields suggests that these measured Rayleigh wave parameters are generally in accord with the second compatibility relation in the Helmholtz equation (see also Figure 1.4). The positive correlation between $\nabla \cdot \vec{B}$ and geometrical spreading also suggests that $\nabla \cdot \vec{B}$ may be robust enough to use in future work to provide constraints for density variations [*Lin et al.*, 2012].

1.4 Isotropic Phase Velocity Results

Surface wave azimuthal anisotropy has been observed in the crust [*Lin and Schmandt*, 2014] and upper mantle [*Beghein et al.*, 2010; *Lin and Ritzwoller*, 2011a] across the United States. We expect the stacking of results from multiple events is able to reduce the effect

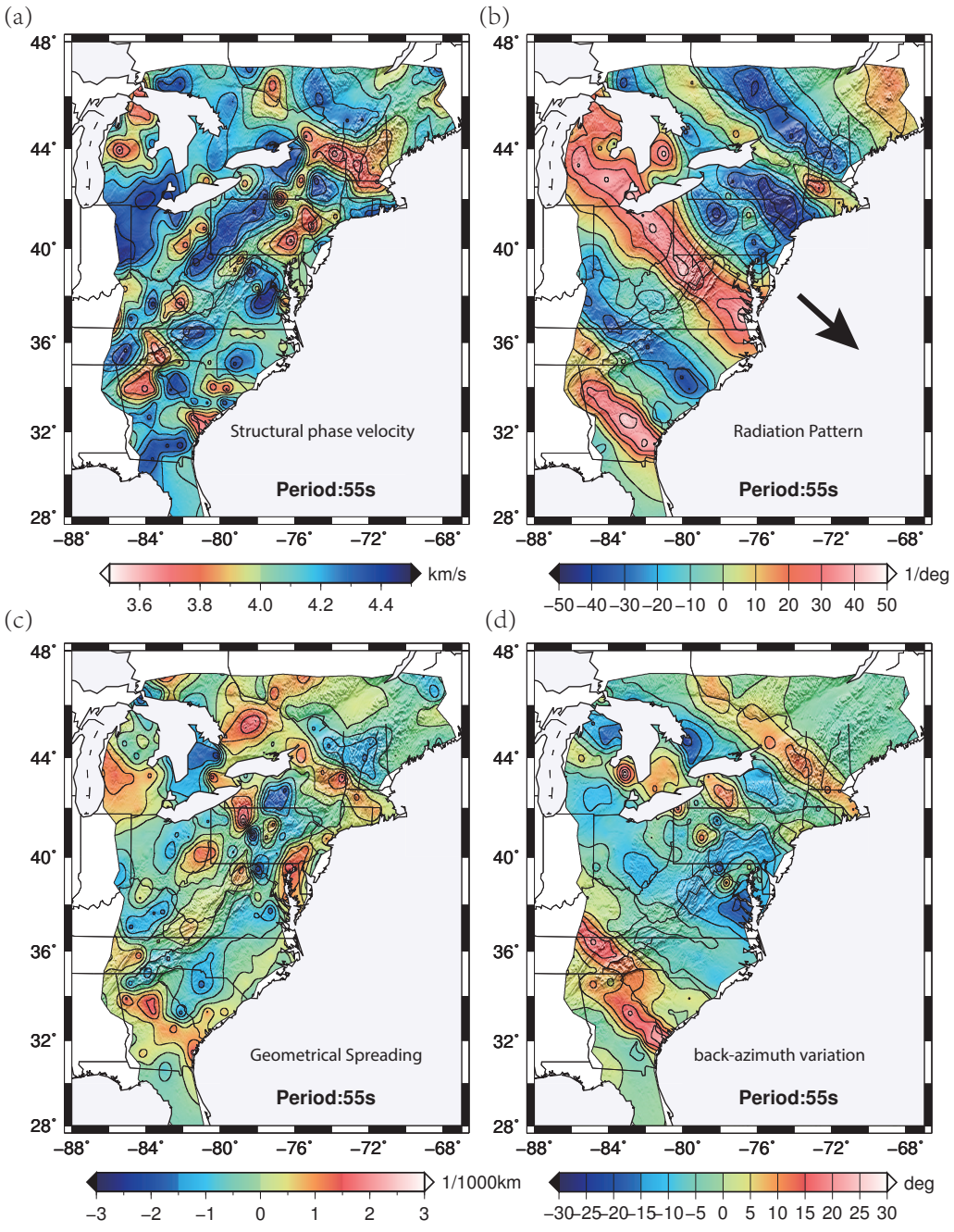

FIGURE 1.14: Wave propagation parameters for 55 s Rayleigh wave, estimated from the 2013 October 25, earthquake near Honshu.

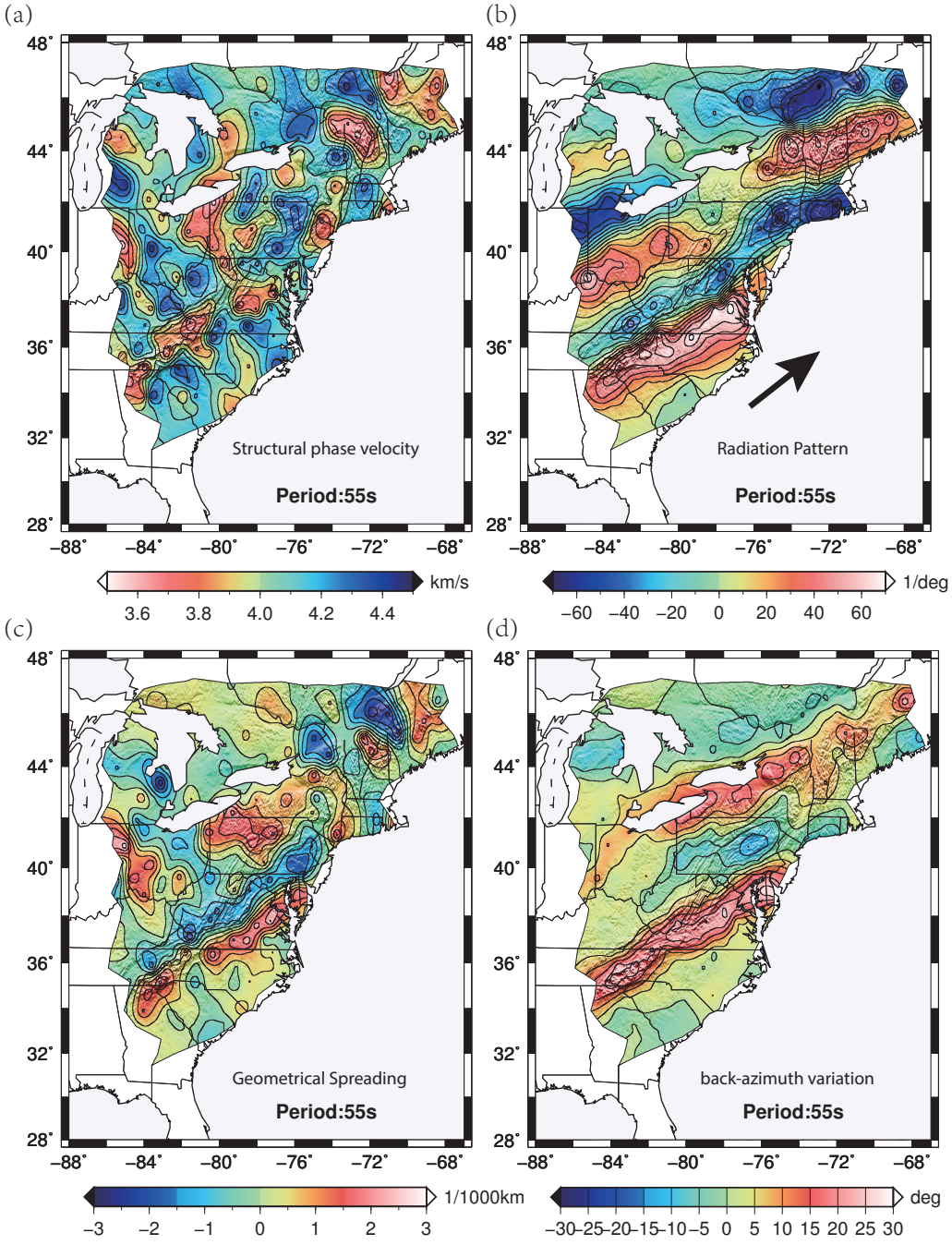

FIGURE 1.15: Wave propagation parameters for 55 s Rayleigh wave, estimated from the 2014 February 2, earthquake near Kermadec Island.

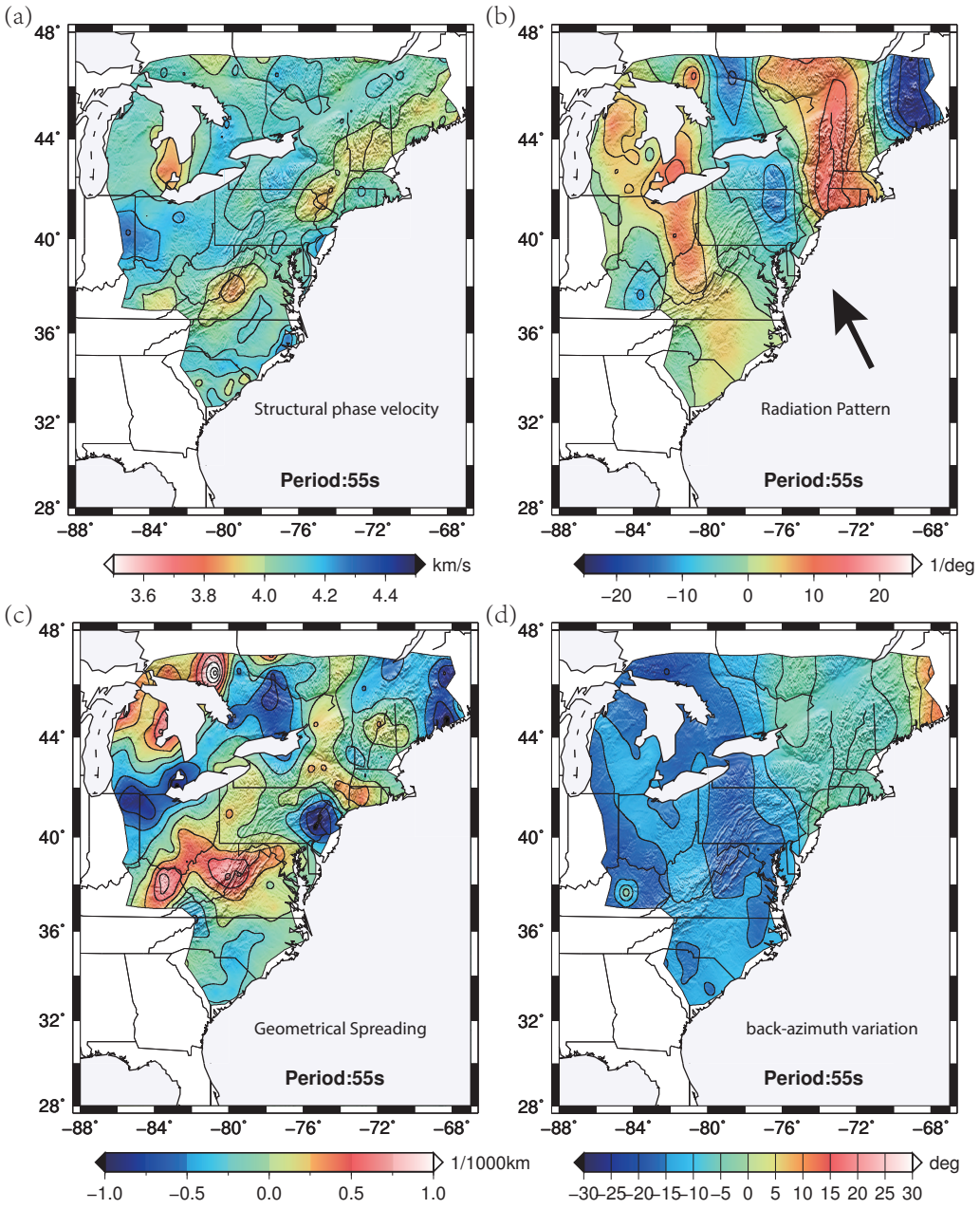

FIGURE 1.16: Wave propagation parameters for 55 s Rayleigh wave, estimated from the 2014 March 16, earthquake near Chile.

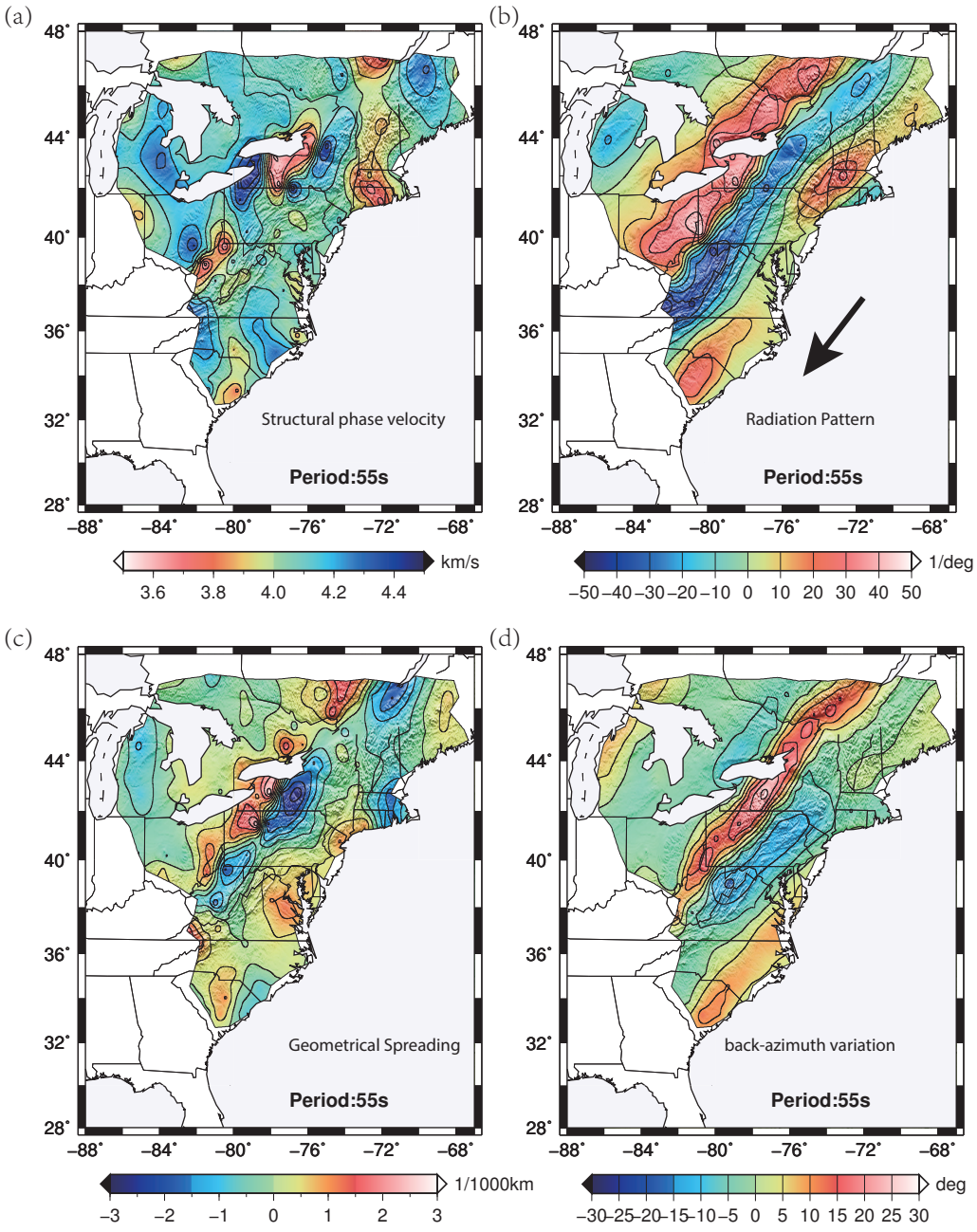

FIGURE 1.17: Wave propagation parameters for 55 s Rayleigh wave, estimated from the 2014 May 24, earthquake in Aegean Sea.

of azimuthal anisotropy [*Liang and Langston*, 2009; *Foster et al.*, 2013]. The isotropic phase velocity results for 12 period bands are shown in Figure 1.18, 1.19 and 1.20. The phase velocity generally increases with period from 3.5 km/s to 4.5 km/s and is consistent with the theoretical dispersion curve [*Dahlen and Tromp*, 1998]. The formal standard error of phase velocity for any given event is less than 1%. However, the dispersion of data from multiple azimuths yields a variation in phase velocity with standard errors of around 3%. The dynamic and structural phase velocity differences decrease from 0.4 km/s for individual events to 0.1 - 0.2 km/s for isotropic results. However, we do observe that these differences increase with period, especially for periods longer than 50 s, which may account for finite frequency effects. *Lin and Ritzwoller* [2011a] also draw similar conclusions from observations in the western U.S.

Results for 20 s, 24 s, 28 s and 31 s periods show a clear transition from higher to lower velocity along the easternmost boundary of the Appalachian topography, corresponding approximately to the location of the early Paleozoic continental margin boundary [*Cook and Oliver*, 1981]. We also observe two distinct low-velocity zone anomalies for 37 s, 40 s, 44 s and 49 s periods: one centered along the Virginia - West Virginia state boundary, and the other one located in Vermont, New Hampshire and easternmost New York. The anomalies persist within both regions for longer periods out to 112 s, but they are weaker for these longer periods. The anomaly in Virginia/west Virginia border region may be associated, in part, with the thicker crust beneath the Appalachians [*Parker et al.*, 2013], but the presence for the longer periods may suggest a persistence of this anomaly within the upper mantle. These low velocity zones are consistent with surface wave tomography

results from *Jin and Gaherty* [2015], and P and S wave velocity models at depths of 60 - 300 km obtained by *Schmandt and Lin* [2014]. *Liang and Langston* [2008] observed the 15 s Rayleigh wave low group velocity anomalies around the center part of the Appalachian Mountains. A 3-D S-velocity model of upper mantle beneath U.S., NA04, [*van der Lee and Frederiksen*, 2005] also revealed the northern anomaly feature even prior to the arrival of USArray to the northeastern U.S. *Eaton and Frederiksen* [2007] and *Villemaire et al.* [2012] claim this anomaly coincides with the inferred track of Great Meteor hotspot, which extends from northern Hudson bay to the northeast U.S. coast, and continues southeast as a chain of seamounts in the Atlantic ocean [*Duncan*, 1984]. *Schmandt and Lin* [2014] pointed out that the passive margin region has experienced Eocene basaltic volcanism at 48 Ma [*Mazza et al.*, 2014], and the center of the low velocity anomaly we observe beneath the border of Virginia - West Virginia corresponds to the location of this volcanism. We discard several bad stations located around southern Alabama and Northern Kentucky, which are the least-well resolved regions due to edge effects.

1.5 Discussion and Conclusions

We use a modified wave gradiometry method to process 37 events recorded by around 450 USArray TA stations in the eastern U.S. Compared to traditional ray-based tomographic techniques, the advantage of wave gradiometry is that the spatial variations of wave amplitudes across the whole array are taken into account, which further provides an approximate solution to the Helmholtz equation. Consequently, the effects from local geometry of the wavefield and phase interferences are greatly decreased [*Wielandt*,

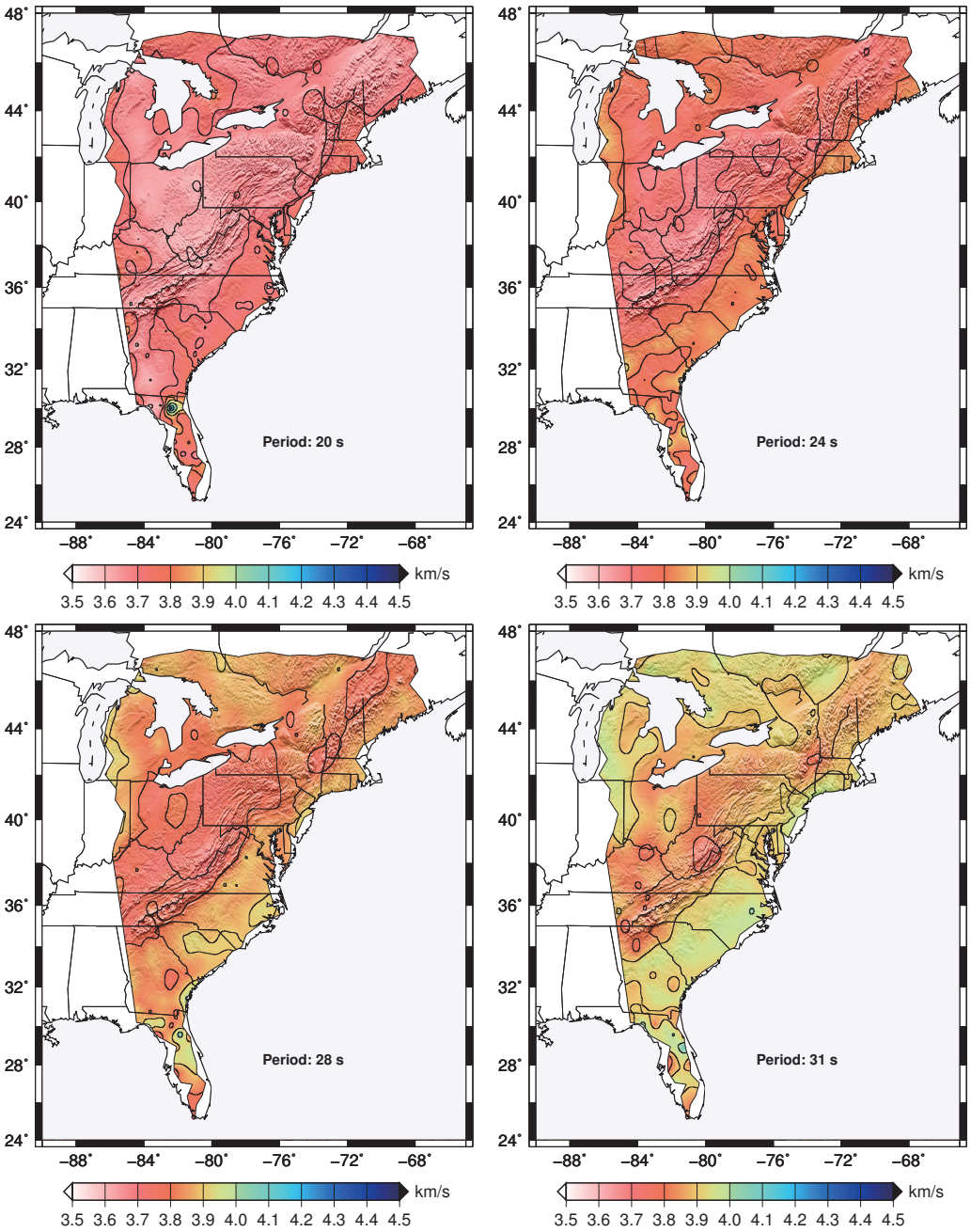

FIGURE 1.18: Isotropic phase velocities for 20 s - 31 s Rayleigh wave. Contours are separated by intervals of 0.1 km/s.

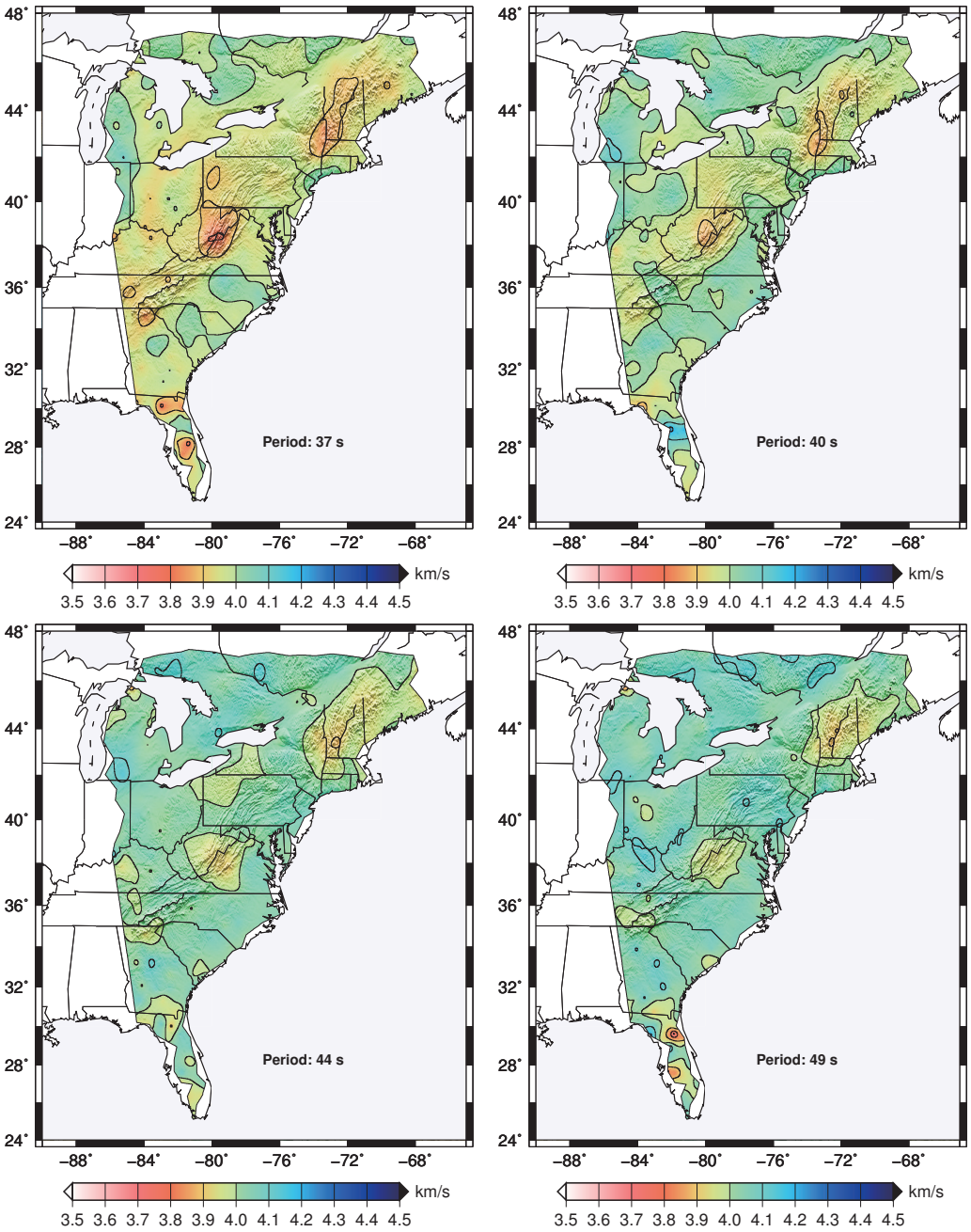

FIGURE 1.19: Isotropic phase velocities for 37 s - 49 s Rayleigh wave. Contours are separated by intervals of 0.1 km/s.

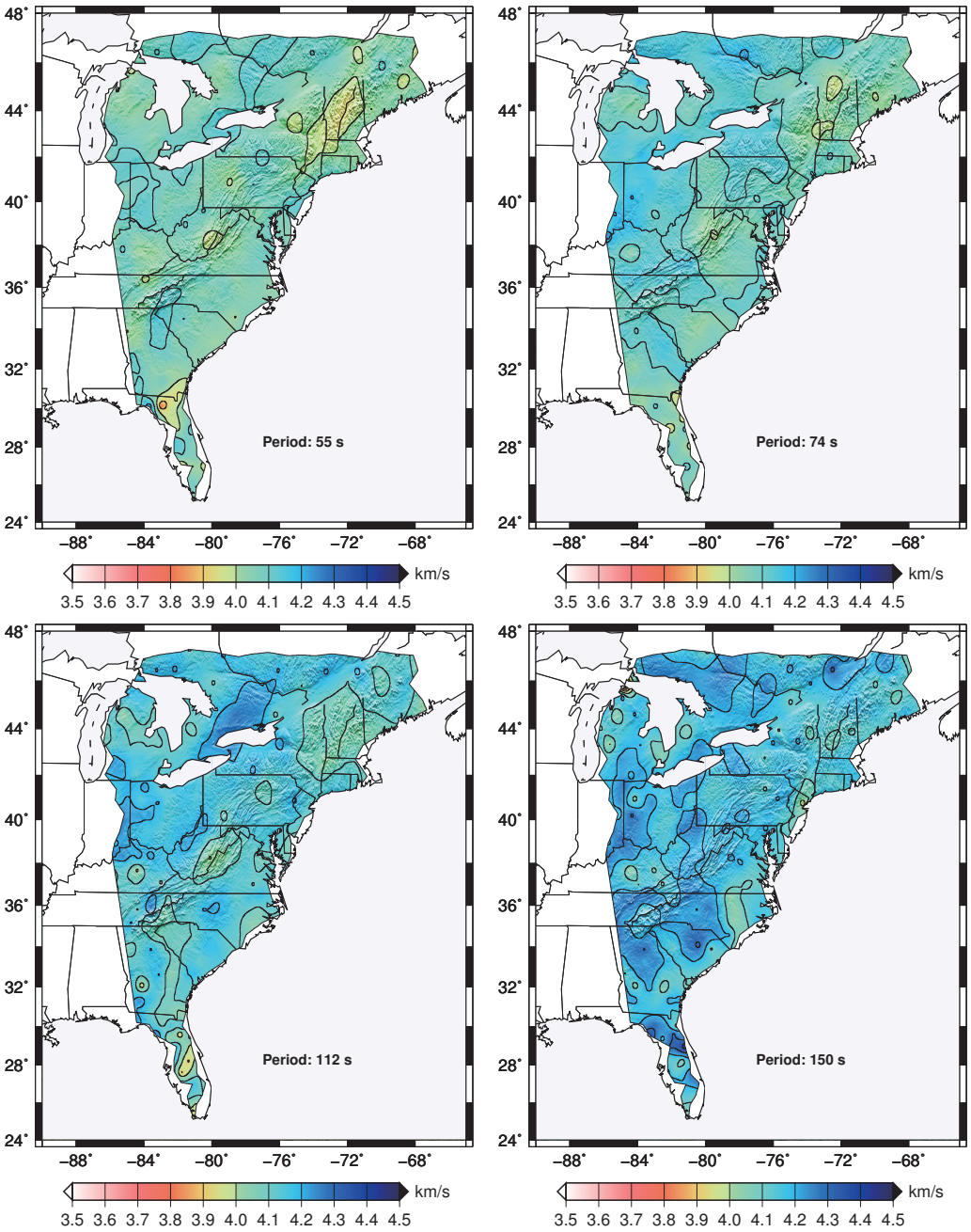

FIGURE 1.20: Isotropic phase velocities for 55 s - 150 s Rayleigh wave. Contours are separated by intervals of 0.1 km/s.

1993]. The gradiometry results for any given event provide insight into the link between variations in geometrical spreading, back-azimuth variations, focusing and defocusing of energy, radiation patterns, and amplitude variations.

In the wave gradiometry method we first obtain the displacements and the time derivatives of displacement field, then calculate the spatial gradients of displacement field through bi-cubic spline interpolation, for the shifted waveforms within a subarray. We then solve for the $\vec{A}$ and $\vec{B}$-coefficients iteratively, using damped least-squares inversion with smoothing, which enables us to estimate phase velocity, changes in geometrical spreading, radiation pattern, and back-azimuth variations. It turns out that the $\vec{A}$-coefficient corresponds to the gradient of logarithmic amplitude and the inverse of $\vec{B}$-coefficient provides an approximation to the dynamic phase velocity. Thus we interpolate $\vec{A}$ and $\vec{B}$-coefficient vectors using the same bi-cubic spline method, to obtain $\nabla \cdot \vec{A}$, corresponding to the Laplacian of logarithmic amplitude, and $\nabla \cdot \vec{B}$, corresponding to an approximation to the Laplacian of phase traveltime. The $\vec{A}$-coefficients, along with $\nabla \cdot \vec{A}$, enable us to calculate the amplitude correction term for structural phase velocity.

Finally, we stack Rayleigh wave structural phase velocity results from 37 earthquakes for 15 passbands with center periods ranging from 20 s to 150 s to get isotropic phase velocity maps, which show an interesting contrast between the the Piedmont and Coastal Plain regions and the interior Appalachian chain. This velocity contrast is observed close to the boundary of the early Paleozoic continental margin location [*Cook and Oliver*, 1981] and is present for periods 20 s - 31 s. We also observe two prominent low velocity zones for periods 37 s - 49 s: one in the central Appalachians, centered along the Virginia

- West Virginia boarder region, and the other in the northeast located in Vermont, New Hampshire and easternmost New York. The anomalies persist for the longer periods out to 112 s, but are not as strong. The central Appalachian anomaly is located in the region of Eocene basaltic volcanism [*Mazza et al.*, 2014; *Schmandt and Lin*, 2014] and the northeast low velocity anomaly is thought to correspond to the meteor hotspot track [*Eaton and Frederiksen*, 2007; *Villemaire et al.*, 2012].

In general, geometrical spreading and $\nabla \cdot \vec{B}$ are strongly correlated, but these two are anti-correlated with Laplacian of logarithmic amplitude or $\nabla \cdot \vec{A}$. The angle difference between the energy propagation direction and the expected great circle path can be as large as $\pm 30^{\circ}$ (back-azimuth variations). The links between radiation pattern, geometrical spreading and structural phase velocity represents areas of energy focusing/defocusing that still require exploration. We find that the gradiometry parameter distributions are unique for any given event and associated ray path. A complete structural interpretation for the diverse distributions of gradiometry parameters obtained from 37 events, with 15 period bands for each event, is beyond the scope of this paper. However, one future application, involving solutions to the wave equation for full 3-D structure [*Tape et al.*, 2009; *Zhu et al.*, 2015], may be to model such spatial variations in radiation, geometrical spreading, back-azimuth, and structural phase velocity for any given event. That is, a match between synthetic and observed gradiometry parameters has the potential to rigorously ensure a viable structural interpretation by providing a broader set of wavefield observables. The azimuthal anisotropy can also be explored by studying the phase velocity maps obtained from individual earthquakes. Moreover, $\vec{A}$, $\vec{B}$, $\nabla \cdot \vec{A}$ and $\nabla \cdot \vec{B}$ can be

used to infer density information along the ray path.

We have investigated two separate compatibility relations: one in the wave equation solution (1.1) and the other in the Helmholtz equation solution (1.17), and have shown that each relation can provide useful information on the characteristics of the wavefield. The assumptions embedded in equation (1.1) involve a single dominant phase [*Langston*, 2007a], and the slowness for this phase can be recovered using the gradiometry method. The Helmholtz equation results in an amplitude correction term that can be substantial if the amplitude variations are large. The question arises as to the link between the slowness embedded in the gradiometry $\vec{B}$-coefficient and the structural phase velocity arising from the Helmholtz treatment. The slowness defined in equation (1.7) is not necessarily equal to the gradient of phase traveltime embedded in equation (1.17), unless this gradient precisely defines the local ray slowness for a single phase. In general, this is unlikely to be true due to finite frequency, multi-pathing, and scattering effects. However, we find that the slowness field obtained using gradiometry assumptions generally provides excellent agreement with results obtained using gradient of phase traveltime methods [*Lin and Ritzwoller*, 2011a]. This empirical result has led us to make the approximation that the $\vec{B}$-coefficient is approximately equal to the gradient of phase traveltime, and thus it is valid to explore the amplitude correction term embedded in Helmholtz treatment. Both *Wielandt* [1993] and *Lin and Ritzwoller* [2011a] have shown that there are substantial amplitude correction terms where there is strong wavefront curvature.

It important to keep in mind that both equations (1.1) and (1.17) involve approximations of the real wavefield, yet employing both provide important insights into the

nature of that wavefield. We have shown that the gradiometry method can provide realistic estimates of the slowness of the local wavefield along with estimates of amplitude correction terms. Our results show a strong link between amplitude variations and the focusing/defocusing of energy (reflected in $\nabla \cdot \vec{B}$) associated with the wavefront curvature, which we are able to resolve over length scales about twice the station spacing. We argue that in the presence of wavefront curvature it is valid to investigate the second compatibility relation in the Helmholtz equation in order to explore the effects of the amplitude correction terms. These corrections may be justified due to the strong local curvature of the wavefront [*Friederich et al.*, 1995]. We find that only where there is strong curvature of the wavefront are there significant amplitude correction terms, providing significant differences between dynamic and structural phase velocity. In regions where wave gradiometry shows no curvature, we find little to no amplitude correction and dynamic phase velocity equals structural phase velocity. One great value of gradiometry, therefore, is to show where the wavefield has complexity. Further work is needed to better understand the link between gradiometry parameters obtained from assumptions in equation (1.1), the amplitude correction terms associated with the separate Helmholtz treatment in equation (1.17), and the effects of true structural complexity on the inferred results. Again, the investigation with full 3-D synthetics associated with structural complexity will be necessary to fully explore this link.

Chapter 2

Analysis of Six Events in Gulf of California

2.1 Introduction

The USArray has yielded numerous detailed studies of the crust and upper mantle structure in the western U.S. [*Burdick et al.*, 2008; *Sigloch et al.*, 2008; *Liang and Langston*, 2009; *Schmandt and Humphreys*, 2010; *Pollitz and Snoke*, 2010; *Porritt et al.*, 2014] and in the Central and Eastern U.S. [*Shen et al.*, 2013b; *Schmandt and Lin*, 2014; *Liu and Holt*, 2015; *Pollitz and Mooney*, 2016]. The USArray has also enabled the developments and applications of new methods that utilize the spatial derivatives of wavefield parameters (amplitudes, phase travel times), such as wave gradiometry, Eikonal tomography, and Helmholtz equation solution methods [*Liang and Langston*, 2009; *Lin et al.*, 2009; *Pollitz and Snoke*, 2010; *Lin and Ritzwoller*, 2011b,a; *Lin et al.*, 2012; *Liu and Holt*, 2015; *Jin and Gaherty*, 2015; *Porter et al.*, 2016]. *Liu and Holt* [2015] showed that wave gradiometry parameters provide insights into the relationship between amplitude variations and the focusing and defocusing of wavefield energy. They observed large variations in wavefield behavior for different events, depending upon event location. *Liu and Holt*

[2015] also argued that wave gradiometry parameters may provide additional constraints for crust and upper mantle structure with 3-D forward and inversion methods. A significant and related question is how amplitude variations and the focusing and defocusing of energy are linked with Earth structure and how they are related to source processes?

The configuration of the USArray determines that the variations of the wave gradiometry parameters for any given earthquake are only captured over relatively short spatial scales, limiting the ability to study both the continuities and variations of wavefield characteristics across the continent. Therefore, in this study we use six earthquakes located in the Gulf of California that have similar locations, depths, magnitudes and focal mechanisms. These events are selected such that the entire USArray configuration captured energy from one or more of these earthquakes. Applications of wave gradiometry methods to wavefields emitted from similar sources, provides us the opportunity to investigate the spatial coherence and characteristics of the wavefield attributes from a relatively consistent radiation source across the contiguous U.S. We want to address the following questions: do the gradiometry parameters reflect coherent patterns for changes in geometrical spreading, radiation pattern, and propagation directions? Are the variations of amplitudes correlated with the patterns of energy focusing and defocusing? Do the gradiometry patterns vary from event to event and are they dependent on event magnitude? How well do gradiometry parameters derived from synthetic seismograms based on 3-D Earth model agree with observed gradiometry parameters? Are gradiometry estimates sensitive to the input lithosphere structure?

We first briefly review the wave gradiometry theory. The reader is referred to *Liu*

and Holt [2015] for further details. We then apply wave gradiometry to 60 s Rayleigh wave wavefields that originated from six earthquakes in the Gulf of California. The resolved gradiometry parameters $\vec{A}$, $\vec{B}$, $\nabla \cdot \vec{A}$ and $\nabla \cdot \vec{B}$ show the attributes of the wavefield, with the assumption that the wavefield is dominated by a single phase [*Langston*, 2007a,b,c; *Liu and Holt*, 2015]. The gradiometry parameters provide details on the local curvature of the wavefield, the focusing and defocusing of energy and its relation to amplitude variations. We investigate the details of these variations across the contiguous U.S. These new constraints can potentially improve our understanding of the actual wavefields and the viable structural interpretations from sources to receivers. The wave gradiometry method is then applied to synthetic waveforms from two different models, US_{00}, a relatively smoothed model with 3-D mantle model S362ANI [*Kustowski et al.*, 2008] in combination with crustal model Crust2.0 [*Bassin*, 2000], and US_{22}, an updated Earth model constructed based on adjoint tomography. We show that the gradiometry parameters are sensitive to the Earth structure and focal mechanism. Given these observations we argue that the gradiometry patterns may provide further constraints for the lithosphere structure utilizing 3-D full waveform synthetics.

2.2 Wave Gradiometry Methodology

Liu and Holt [2015] have described the wave gradiometry technique and its link with the Helmholtz equation solutions in detail. We provide some of the key components below that are linked with our specific analysis of the Gulf of California events.

In a Cartesian coordinate system, differentiating the wave equation solution gives us

a set of equations (2.1) and (2.2), which link the displacements u, the spatial gradients $\frac{\partial u}{\partial x}$, $\frac{\partial u}{\partial y}$, and the time derivatives of displacement field $\frac{\partial u}{\partial t}$, to gradiometry coefficients A_x, A_y, B_x, B_y [*Langston*, 2006, 2007a,b,c; *Liang and Langston*, 2009].

$$\frac{\partial u}{\partial x} = A_x \cdot u + B_x \cdot \frac{\partial u}{\partial t} \tag{2.1}$$

$$\frac{\partial u}{\partial y} = A_y \cdot u + B_y \cdot \frac{\partial u}{\partial t} \tag{2.2}$$

Once these coefficients are solved iteratively at each seismic station, the following relations can be used to estimate four gradiometry products: dynamic phase velocity v [*Wielandt*, 1993; *Liu and Holt*, 2015], back-azimuth θ, radiation pattern $A_\theta(\theta)$, and geometrical spreading $A_r(\theta)$ [*Liang and Langston*, 2009]:

$$v = \frac{1}{\sqrt{B_x^2 + B_y^2}} \tag{2.3}$$

$$\theta = tan^{-1}(\frac{B_x}{B_y}) \tag{2.4}$$

$$A_\theta(\theta) = r(A_x \cos\theta - A_y \sin\theta) \tag{2.5}$$

$$A_r(\theta) = A_x \sin\theta + A_y \cos\theta \tag{2.6}$$

where r is the epicentral distance.

The real part of the Helmholtz equation solutions, as defined by *Lin and Ritzwoller* [2011b], can be written using gradiometry parameters [*Liu and Holt*, 2015]:

$$\frac{1}{c^2} \approx |\vec{B}|^2 - \frac{\vec{A}^2 + \nabla \cdot \vec{A}}{\omega^2} \tag{2.7}$$

where c is the structural phase velocity, $\vec{B}$ gives the approximation to the dynamic phase slowness, and ω is the angular frequency. *Liu and Holt* [2015] have shown that $\vec{A}$-coefficients and $\nabla \cdot \vec{A}$, are equivalent to the gradient of logarithmic amplitude and Laplacian of logarithmic amplitude, respectively. This solution is written as an approximation because it depends on the assumption that the $\vec{B}$-coefficient can be approximated as the negative of gradient of phase travel time [*Liu and Holt*, 2015] and $\nabla \cdot \vec{B}$ is thus equivalent to the Laplacian of phase travel time. These parameters, along with radiation pattern and geometrical spreading (Equations (2.5) and (2.6)), will be used to evaluate the characteristics of the wavefields emitted from six Gulf of California events below.

Wielandt [1993] pointed out that the dynamic phase velocity cannot be directly attributed to the structure and cannot be used as an input for tomographic structure inversions. The second term on the right hand side of equation (2.7) is the amplitude correction term [*Lin and Ritzwoller*, 2011a], containing the square of the $\vec{A}$-coefficient (gradient of logarithmic amplitude), and $\nabla \cdot \vec{A}$ (Laplacian of logarithmic amplitude). *Wielandt* [1993] argued that this correction term is significant and can be used to estimate the structural phase velocity, which should be used for structure interpretation instead of dynamic phase velocity, at least for periods longer than 50 s for the USArray TA station configuration (70 km station spacing) [*Lin and Ritzwoller*, 2011a; *Liu and*

Holt, 2015].

The imaginary part of the Helmholtz equation solutions [*Wielandt*, 1993], is referred to as the transport equation [*Cerveny*, 2005]:

$$2 \cdot \vec{B} \cdot \vec{A} - \nabla \cdot \vec{B} = 0 \tag{2.8}$$

This compatibility relation gives us insights into how the patterns of gradiometry parameters are related to energy focusing and defocusing [*Liu and Holt*, 2015] (discussed later in Section 3.3). *Lin et al.* [2012] referred to the first and second term on the left hand side of equation (2.8) as apparent amplitude decay and focusing/defocusing correction, respectively. The combination of the apparent amplitude decay and the focusing/defocusing correction is the corrected amplitude decay, which is linked directly to the local amplification factor and intrinsic attenuation [*Lin et al.*, 2012]. *Lin et al.* [2012] argued this new surface wave observable - the corrected amplitude decay - provides potential new constraints to the phase velocity, attenuation, and density within the crust and upper mantle.

2.3 Derivation of Models Used to Test Sensitivity of Gradiometry Parameters to Structural Input

In this paper we argue that the gradiometry parameters can be used as additional constraints, when combined with 3-D synthetic modeling, to refine structural models. For example, adjoint tomography methods [*Tromp et al.*, 2005; *Tape et al.*, 2009; *Zhu et al.*, 2012] take advantage of full wavefield calculations from 3-D Earth models. In this paper

we investigate sensitivity of derived gradiometry parameters associated with synthetics generated from two distinct Earth models, US_{00} and US_{22}, which are described below.

Adjoint tomography [*Tromp et al.*, 2005; *Tape et al.*, 2009; *Zhu et al.*, 2012] is used to iteratively invert for crust and upper mantle structure beneath the North American continent. 180 earthquakes with magnitudes ranging from 5 to 6.5, and 4,516 seismographic stations are used in this study. Most stations are collected from the USArray. For the first iteration, we obtain 460,539 frequency-dependent phase measurements by comparing synthetic and observed seismograms. The initial 3-D model US_{00} is constructed based on crustal model Crust2.0 [*Bassin*, 2000] and mantle model S362ANI [*Kustowski et al.*, 2008]. Radially anisotropic (frequency-dependent) sensitivity kernels are employed in the structure inversion to image anisotropic features within the upper mantle [*Zhu et al.*, 2015]. Three component body and surface waves are combined to simultaneously constrain shallow and deep structures. No crustal correction is applied in the inversion since crust and upper mantle are updated simultaneously. Higher frequency signals are gradually incorporated in the inversion in order to resolve small scale heterogeneities and avoid cycle-skipping problems [*Bunks et al.*, 1995]. The updated model, US_{22}, is constructed after 22 nonlinear conjugate gradient iterations [*Fletcher and Reeves*, 1964], which involves numerous interesting features in the North American continent, for instance, significant contrast between eastern and western North America, slab features beneath the Cascadia subduction zone and Caribbean, slow anomalies related to the Asthenosphere beneath the North Atlantic ocean, etc.

TABLE 2.1: The six Gulf of California events used in this study.

Time	Lat	Lon	Depth	Mag	Strike	Dip	Slip
2007/09/01	24.76	-109.89	14.9	6.1	26	81	-4
2009/07/03	25.20	-109.87	14.4	5.9	46	87	-1
2010/10/21	24.83	-109.29	14.2	6.7	41	85	-1
2011/07/26	25.06	-109.63	17.5	6.0	42	79	-9
2012/10/06	25.17	-109.73	19.7	6.0	39	84	-10
2013/10/19	26.17	-110.53	15.1	6.6	42	86	6

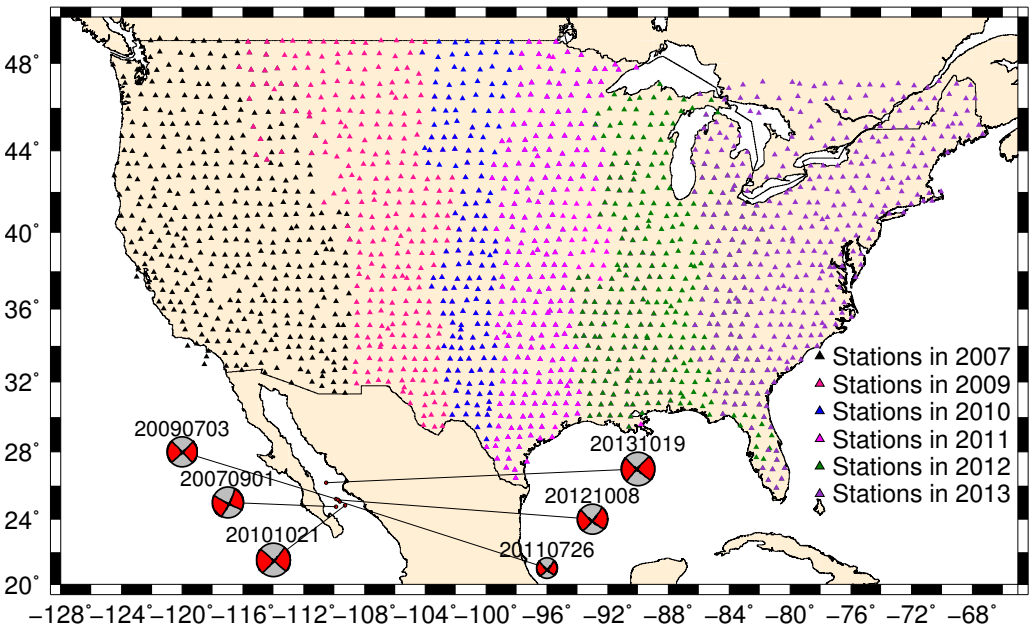

FIGURE 2.1: Red circles indicate the locations of the six Gulf of California earthquakes. Triangles with difference colors indicate USArray TA station locations and the sources of the seismic records.

2.3. Derivation of Models Used to Test Sensitivity of Gradiometry Parameters to Structural Input

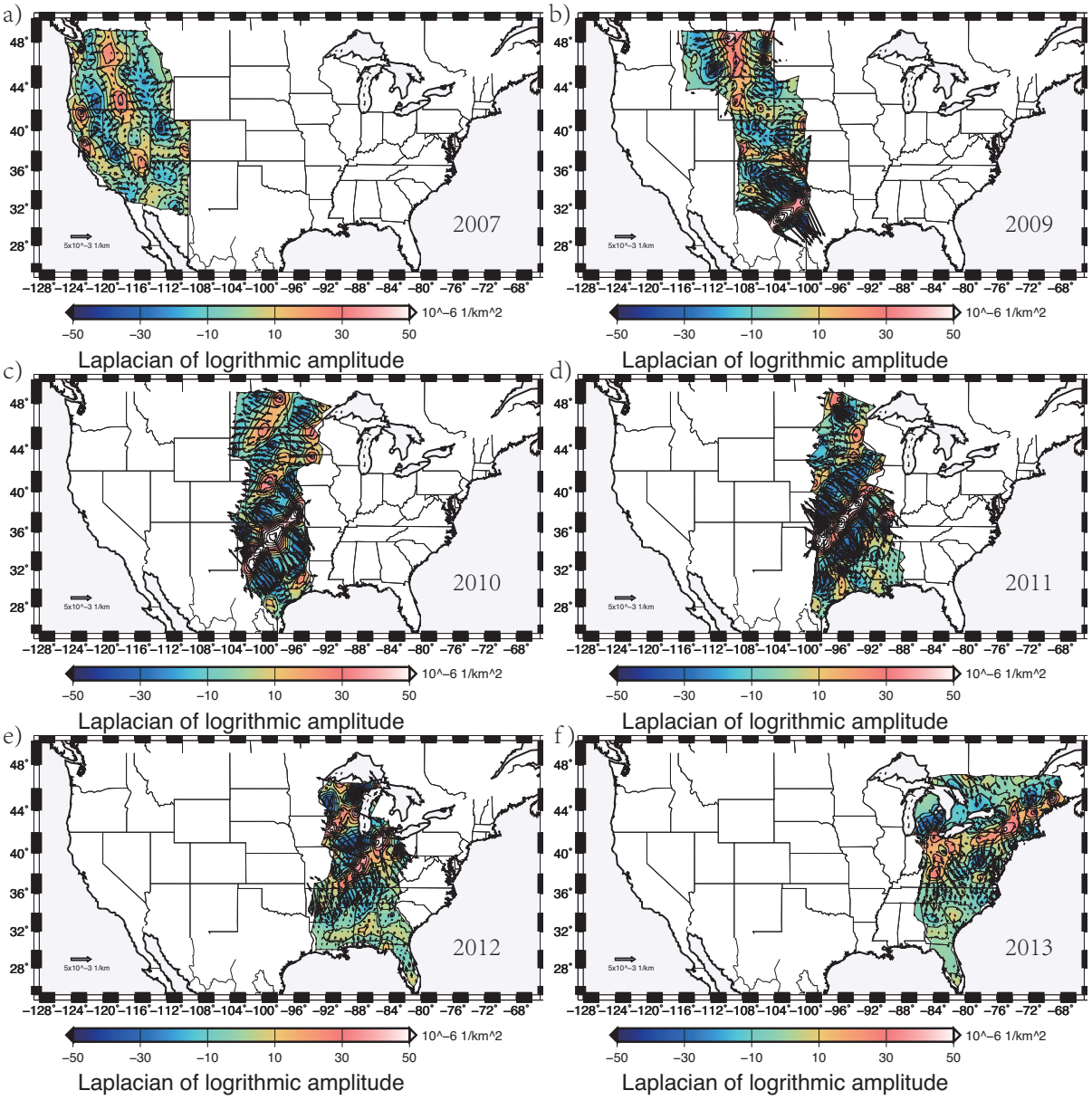

FIGURE 2.2: The 60 s Rayleigh wave gradiometry parameter $\vec{A}$-coefficients obtained from the six Gulf of California events. Vector fields are associated with $\vec{A}$-coefficients and contours show $\nabla \cdot \vec{A}$.

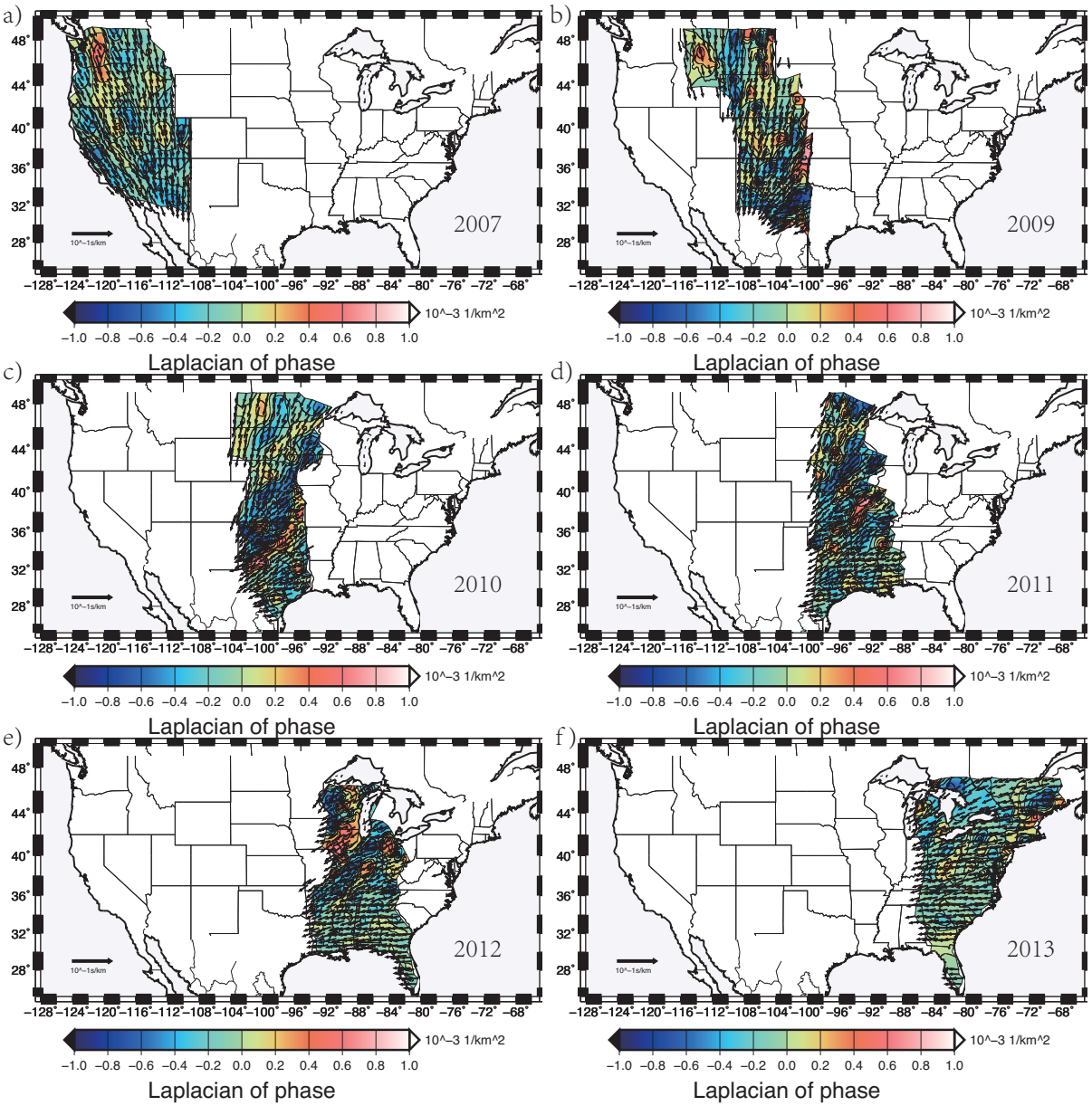

FIGURE 2.3: The 60 s Rayleigh wave gradiometry parameter $\vec{B}$-coefficients obtained from the six Gulf of California events. Vector fields are associated with $\vec{B}$-coefficients and contours show $\nabla \cdot \vec{B}$.

2.4 Analysis of Six Gulf of California Events

2.4.1 Gradiometry Parameters Obtained from Real Records

The location, depths, magnitudes and focal mechanisms of six Gulf of California events used in this study are shown in Table 2.1, which involve the same back-azimuth from southwest. The USArray coverage at the time of the event is displayed by the station distribution map (Figure 2.1). We have computed gradiometry parameters $\vec{A}$ and $\vec{B}$-coefficient vector fields separately from these events (Figures 2.2, 2.3), which show significant complexity for all events and regions. A dominant northeast trending ridge of positive values of $\nabla \cdot \vec{A}$, with diverging $\vec{A}$ vectors (Figure 2.2) appears for events in 2009 - 2013, where USArray coverage is within the midwest and eastern U.S. Along this same northeast trend the $\vec{B}$ vector fields show a prominent ridge of low values of $\nabla \cdot \vec{B}$ (Figure 2.3), which correspond to the strong bending of wavefront away from the expected great circle path. Because the $\vec{B}$ vectors point opposite to the wave direction, this ridge corresponds to a region of strong energy defocusing.

2.4.2 Gradiometry Parameters Obtained from Synthetic Waveforms

One goal in this investigation is to observe the changes and coherence of the gradiometry parameters across the U.S., derived from these similar events. There are some overlaps of stations that measured different events. We find a consistency for the directions of $\vec{A}$-coefficients and the sign of $\nabla \cdot \vec{A}$ in regions where overlapping arrays captured two different events. We also observe such a consistency for the overlapping zones for $\vec{B}$-coefficients and

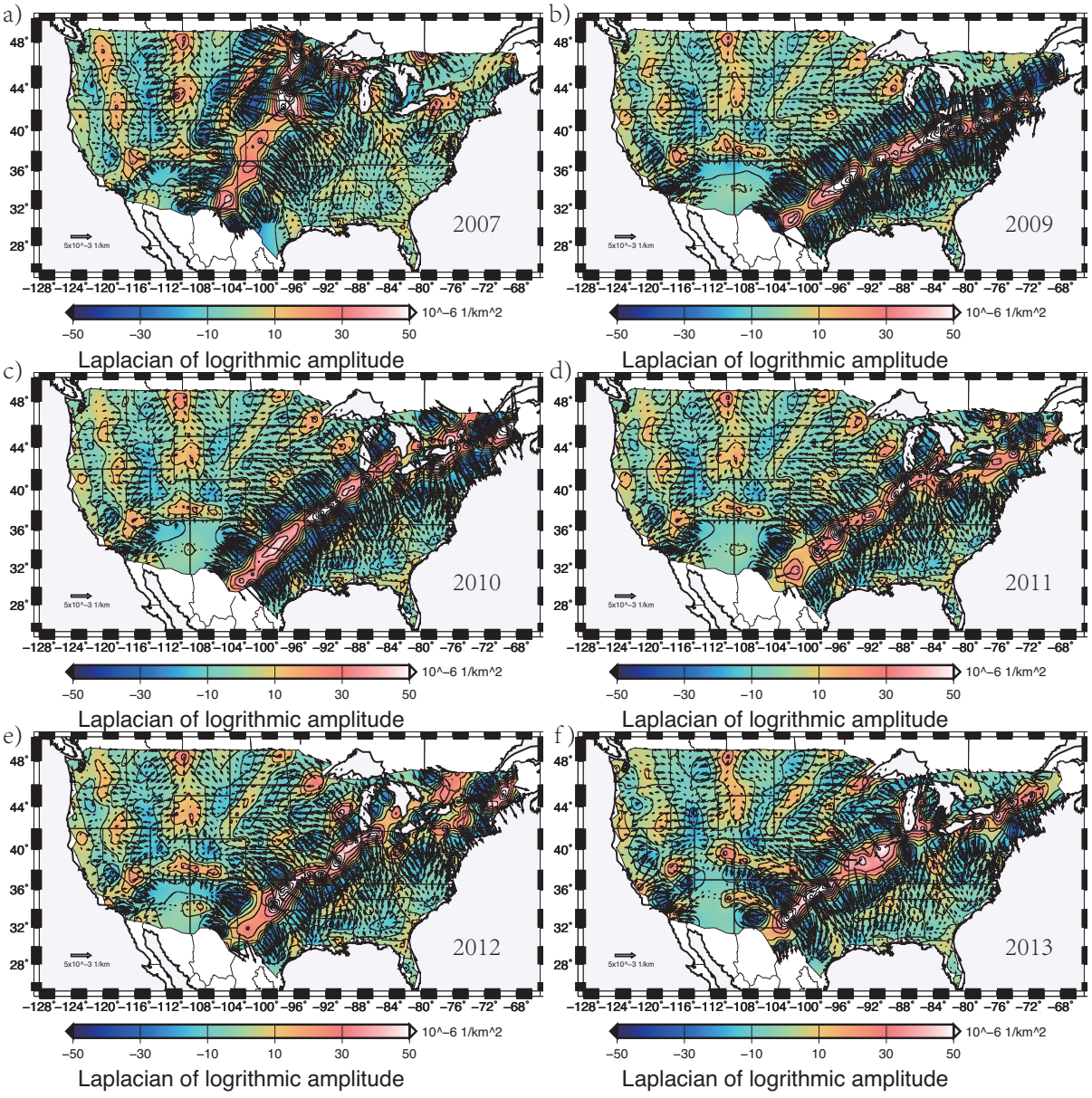

FIGURE 2.4: 60 s Rayleigh wave gradiometry parameter $\vec{A}$-coefficients obtained from synthetic wavefields based on US_{22}.

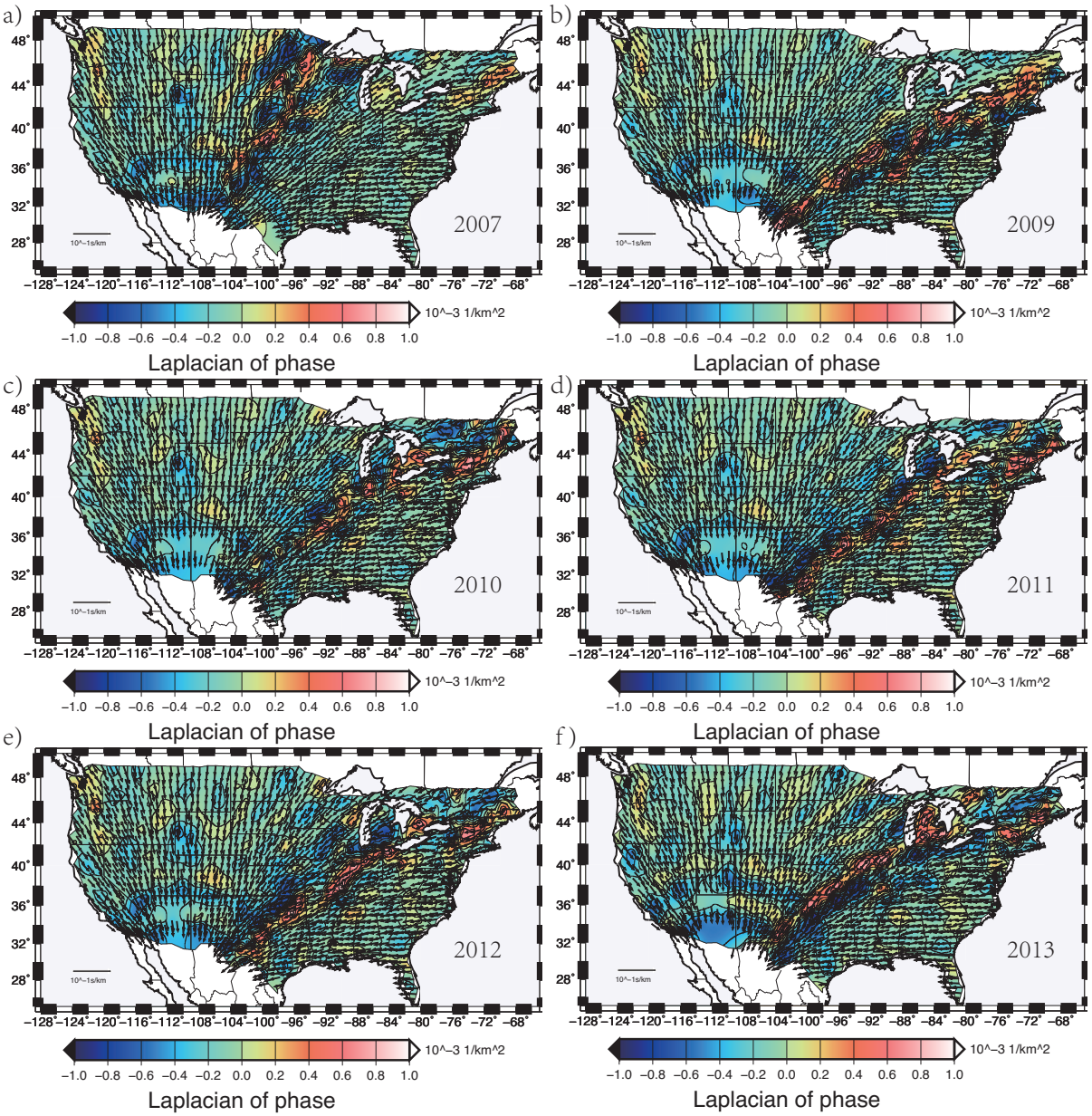

FIGURE 2.5: 60 s Rayleigh wave gradiometry parameter $\vec{B}$-coefficients obtained from synthetic wavefields based on US_{22}.

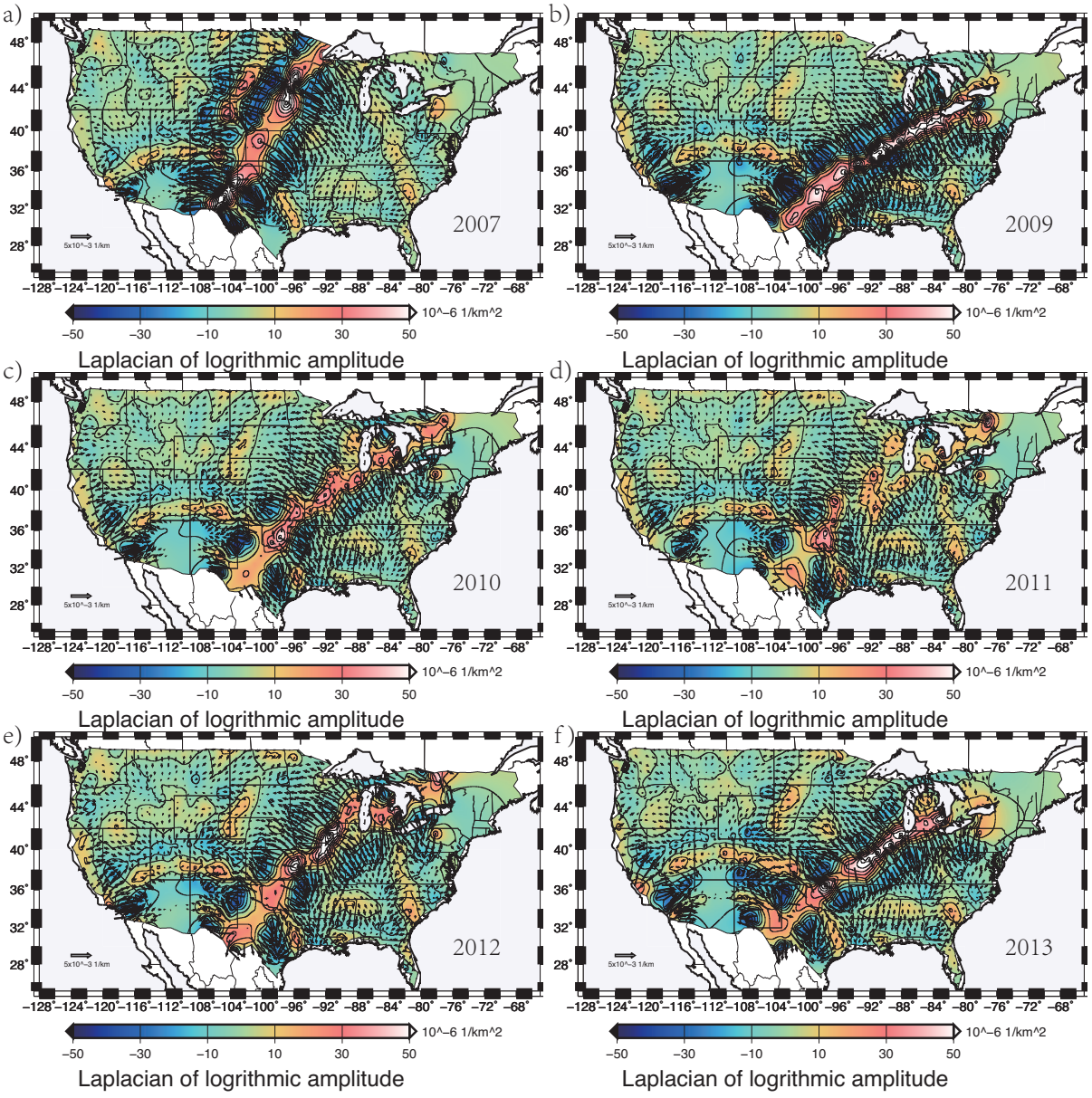

FIGURE 2.6: 60 s Rayleigh wave gradiometry parameter $\vec{A}$-coefficients obtained from synthetic wavefields based on US_{00}.

$\nabla \cdot \vec{B}$. Given this consistency, and the similarity of source mechanisms for these six events (strike, dip and slip angles as shown in Table 2.1), we argue it is justified to combine the gradiometry parameters for all events to view the characters of the wavefields across the entire U.S. region. We first investigate the gradiometry parameters measured from synthetic wavefields based on an updated U.S. tomography model US_{22}. The gradiometry parameters are also estimated for synthetic waveforms from US_{00} [*Tromp et al.*, 2010], a relatively smoothed model. The synthetic seismograms were calculated at the exact locations of the entire USArray (Figure 2.1) for each event. Event data were processed and analyzed in the same way as real data. We determine the gradiometry parameters from these synthetics across entire U.S. region and compare, event-by-event, results with those obtained from the real data (Figure 2.2 and 2.3).

The $\vec{A}$ and $\vec{B}$ vector fields obtained from the synthetic wavefields (Figure 2.4 and 2.5) for all events show overall patterns to the parameters derived from the real data (Figure 2.2 and 2.3). Comparing the $\vec{A}$-coefficient and $\nabla \cdot \vec{A}$ field from the 2007 event (Figure 2.4a) with the observation in Figure 2.2a, there is a good correlation for $\nabla \cdot \vec{A}$, although the observed fields have higher amplitudes. For example, there are agreements of high positive amplitudes in Northern California, southern Nevada, northern Nevada/southern Oregon, and eastern Washington state. NNW oriented troughs of negative values agree well in eastern California - through Oregon and Washington, and along a trend from northwestern Utah through Idaho. The $\vec{A}$ vectors also agree well in directions. For the comparison of $\vec{B}$-coefficient vector fields for the 2007 event (Figure 2.3a and 2.5a) we observe excellent agreement in the directions of vector fields as well as the positions of

positive and negative values for $\nabla \cdot \vec{B}$. However, similar to the case of the $\vec{A}$-coefficient field, the amplitudes of $\nabla \cdot \vec{B}$ for the synthetic wavefields are underestimated when compared with observations. In contrast to model US_{22} the smoothed model US_{00} (Figure 2.6a) does not produce a good match in the areas described above for the 2007 event, indicating that detailed Earth input structure is playing a role in contributing toward the distributions of $\nabla \cdot \vec{A}$ and directions of $\vec{A}$.

The comparison of $\vec{A}$ fields for the 2009 event (Figure 2.2b and 2.4b) again shows excellent agreement for the directions of $\vec{A}$ and the positions of positive and negative values for $\nabla \cdot \vec{A}$, except that the amplitudes of the synthetic wavefield are underestimated. The large ridge of positive $\nabla \cdot \vec{A}$, with diverging values for $\vec{A}$ within west Texas agrees well with the pattern resolved from the synthetics. Comparison of $\vec{B}$ fields for 2009 (Figure 2.3b and 2.5b) show good agreement in directions, but again the amplitudes of $\nabla \cdot \vec{B}$ for the synthetics are generally small in comparison with the observation. There are high amplitude anomalies associated with $\nabla \cdot \vec{B}$ in west Texas, where $\vec{B}$ fields for both synthetics and observation show strong defocusing of energy. For the smoothed model synthetics from US_{00} (Figure 2.6b) the positive predicted zones of $\nabla \cdot \vec{A}$ in west Texas, southern Colorado and western Oklahoma agree well with synthetics, but unlike model US_{22} the smoothed model fails to predict the positive ridge within Montana.

Comparing the 2010 event (Figure 2.2c and 2.4c), we see good agreement with the positive ridge of $\nabla \cdot \vec{A}$ for observation and synthetic within Texas panhandle, Oklahoma, and southeastern Kansas. Likewise, the ridges of the positive and negative values of $\nabla \cdot \vec{A}$ within North and South Dakota, Nebraska, and Minnesota agree in position, but

amplitudes are underestimated in synthetics compared with observations. Comparing the $\vec{B}$ vector fields for the 2010 event (Figure 2.3c and 2.5c), general directions for $\vec{B}$ agree, but a consistent zone of relatively strong defocusing (negative values of $\nabla \cdot \vec{B}$) within Kansas, western Iowa, and southern Minnesota is generally not well predicted by the synthetics. Faint patterns of $\nabla \cdot \vec{B}$ agree in rough position within North and South Dakota, but again amplitudes in the synthetics are small in comparison with observations. The strong band of defocusing along the low amplitude ridge in Oklahoma shows more systematic azimuths (from station to station) in comparison with the more chaotic directions in the synthetics. Other than the positive ridge of $\nabla \cdot \vec{A}$ in Texas and Oklahoma, the smoothed model (Figure 2.6c) fails to predict values of $\nabla \cdot \vec{A}$ outside of these regions.

Comparing 2011 event (Figure 2.2d and 2.4d), we see good agreement for the positions of the positive field of $\nabla \cdot \vec{A}$ through Oklahoma, southeast Nebraska and Missouri. Amplitudes of this field are generally underestimated by the synthetics, but the positions of the anomalies agree well with observations. Comparing the $\vec{B}$ fields and the distributions of $\nabla \cdot \vec{B}$ (Figure 2.3d and 2.5d), we see good agreement in Oklahoma, but the synthetic fields of positive values of $\nabla \cdot \vec{B}$ offset to the southeast within Missouri, whereas the observed fields do not have this offset. Likewise, areas with strong defocusing are not well predicted by synthetics within Iowa and southern Minnesota. The smoothed model (Figure 2.6d) in general provides a poor fit to distributions of $\nabla \cdot \vec{A}$ for the 2011 event.

The positive and negative distributions of $\nabla \cdot \vec{A}$ for the 2012 event synthetics from US_{22} (Figure 2.4e) agree well with fields obtained from observed seismograms (Figure

2.2e). Even regions west of central Lake Michigan and south of Lake Erie within Ohio are matched by the synthetics. The $\vec{B}$ field for 2012 (Figure 2.3e) shows a channel of defocusing energy through Illinois and Indiana in the observation that is predicted slightly offset to the north by the synthetics (Figure 2.5e). The smoothed model (Figure 2.6e) predicts a ridge of positive values of $\nabla \cdot \vec{A}$ west of Lake Michigan, but fails to predict a northeast trending ridge found in the observed field within Illinois and Indiana.

The distributions of $\nabla \cdot \vec{A}$ obtained from the synthetics for the 2013 event (Figure 2.4f) do not agree as well with that obtained from observation (Figure 2.2f) in comparison with other examples discussed above. For example, the synthetics predict a positive region for $\nabla \cdot \vec{A}$ just south of Lake Erie that is not present in the real records, which involves negative values there. The $\vec{B}$ field in the synthetics (Figure 2.5f) shows a strong defocusing of energy just south of Lake Erie that was not present in the observed field (Figure 2.3f). The synthetics from the smoothed model (Figure 2.6f) again provide a relatively poor match with observations for the 2013 event.

2.5 Combination of Gradiometry Parameters from Real Records

Based on similarities in observed gradiometry parameters within regions of array overlap, we combine results from 2009 - 2013 events and interpret them as a single wavefield. Similarities in gradiometry parameters for 2009 - 2013 events in the synthetics provide further support for this step in combining the observed fields together. Although the strike of nodal plain for the 2007 event differs by about 20° from the strikes other events

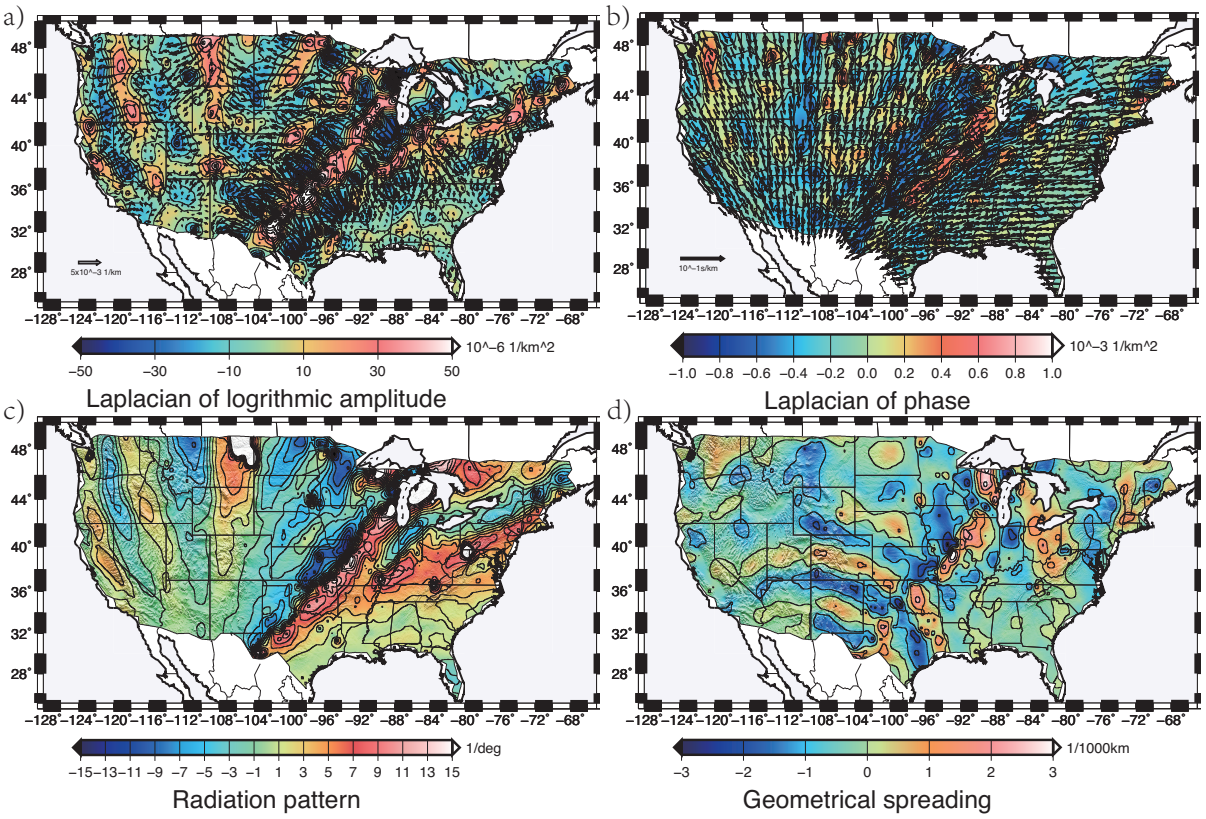

FIGURE 2.7: Gradiometry parameters and products yielded from real records of six Gulf of California events. (a) and (b) show $\vec{A}$ and $\vec{B}$-coefficient fields. (c) and (d) show radiation pattern and geometrical spreading.

(Table 2.1), comparisons of synthetic gradiometry parameters for the 2007 event in the western U.S. with results from the other events show only small differences in the western U.S. region. We thus include results from the 2007 event to obtain complete coverage, from coast-to-coast, for an approximated single wavefield.

2.5.1 Analysis of the $\vec{A}$-coefficients

The $\vec{A}$-coefficient vectors (Figure 2.7a) show interesting patterns, a primary feature is an adjacent ridge of positive $\nabla \cdot \vec{A}$ appears to bifurcate away from the main trend at about southern Illinois and into the northeast U.S. There are several sub-parallel bands

of positive and negative values of $\nabla \cdot \vec{A}$. This combined field allows us to compare with the synthetics from US_{22} more easily.

Comparing Figure 2.7a with the 2009 - 2013 events in Figure 2.4, we observe good agreement, particularly for the western U.S. and west and central Great Plains. Disagreement with the two fields is most pronounced from the mid-continent eastward where the observed ridge of positive values for $\nabla \cdot \vec{A}$ trends along a roughly linear zone and intersects with the central portion of Lake Michigan. There is a smaller, less continuous band of positive $\nabla \cdot \vec{A}$ that trends through southern Illinois, Indiana, Ohio, northern Pennsylvania, eastern New York and parts of New England. The synthetics from US_{22} (Figure 2.4) do not show the linear trend of positive values for $\nabla \cdot \vec{A}$ that intersects with western Lake Michigan. Instead the synthetics show this positive ridge bending in southeast Kansas and southern Missouri and then tracking to the south of Lake Michigan. Matching this observed field with synthetics holds promise for refining structural models in the future, as indicated by the much poorer match that the smoothed model US_{00} provides for this field.

2.5.2 Analysis of the $\vec{B}$-coefficients

The $\vec{B}$-coefficients vectors in Figure 2.7b represent the negative of dynamic wave slowness, which point to the opposite direction of wave propagation. Positive values of $\nabla \cdot \vec{B}$ (contours in Figure 2.7b) highlight regions where the $\vec{B}$ vectors diverge, corresponding to the curvature of wavefront. However, because the $\vec{B}$-coefficients actually point opposite to the slowness directions, positive values for $\nabla \cdot \vec{B}$ represent regions where the energies

converge or focus, while negative values for $\nabla \cdot \vec{B}$ represent regions where the energies diverge or defocus. Energy traveling northward in the western U.S. show increasing complexity to the north of 40 N. From the transport equation (2.8), when $\nabla \cdot \vec{B}$ is relatively small, $\vec{A}$ and $\vec{B}$-coefficient vectors are orthogonal to each other [*Wielandt*, 1993]. We indeed find that the $\vec{A}$-coefficient vectors (Figure 2.7a) are in general perpendicular to the $\vec{B}$-coefficient vectors (Figure 2.7b), except in regions with large values of $\nabla \cdot \vec{B}$, where we argue that wavefields are either focusing or defocusing. An interesting question is what particular lithospheric zones of complexity lead to these amplitude perturbations, the specific energy focusing and defocusing patterns, as the wavefield propagates away from the source?

Comparing the composite $\vec{B}$-coefficients (Figure 2.7b) with the synthetics from US_{22} (Figure 2.5), the observed field shows more complexities in the distribution of $\nabla \cdot \vec{B}$. In particular, the strong zone of energy defocusing in the observed field is placed further north than in the synthetic cases for the 2009 - 2013 events. Because the smoothed model US_{00} does not generally provide nearly as close of a match with details in the field of gradiometry parameters, we do not discuss results from this model any further.

2.5.3 Analysis of the Gradiometry Products

The radiation pattern reflects the amplitude variation orthogonal to the wave propagation direction (Equation (2.5)). We observe several ridges that run roughly parallel to the ray path direction across the contiguous U.S (Figure 2.7c), suggesting that amplitude variations are dominantly orthogonal to propagation direction. The most remarkable

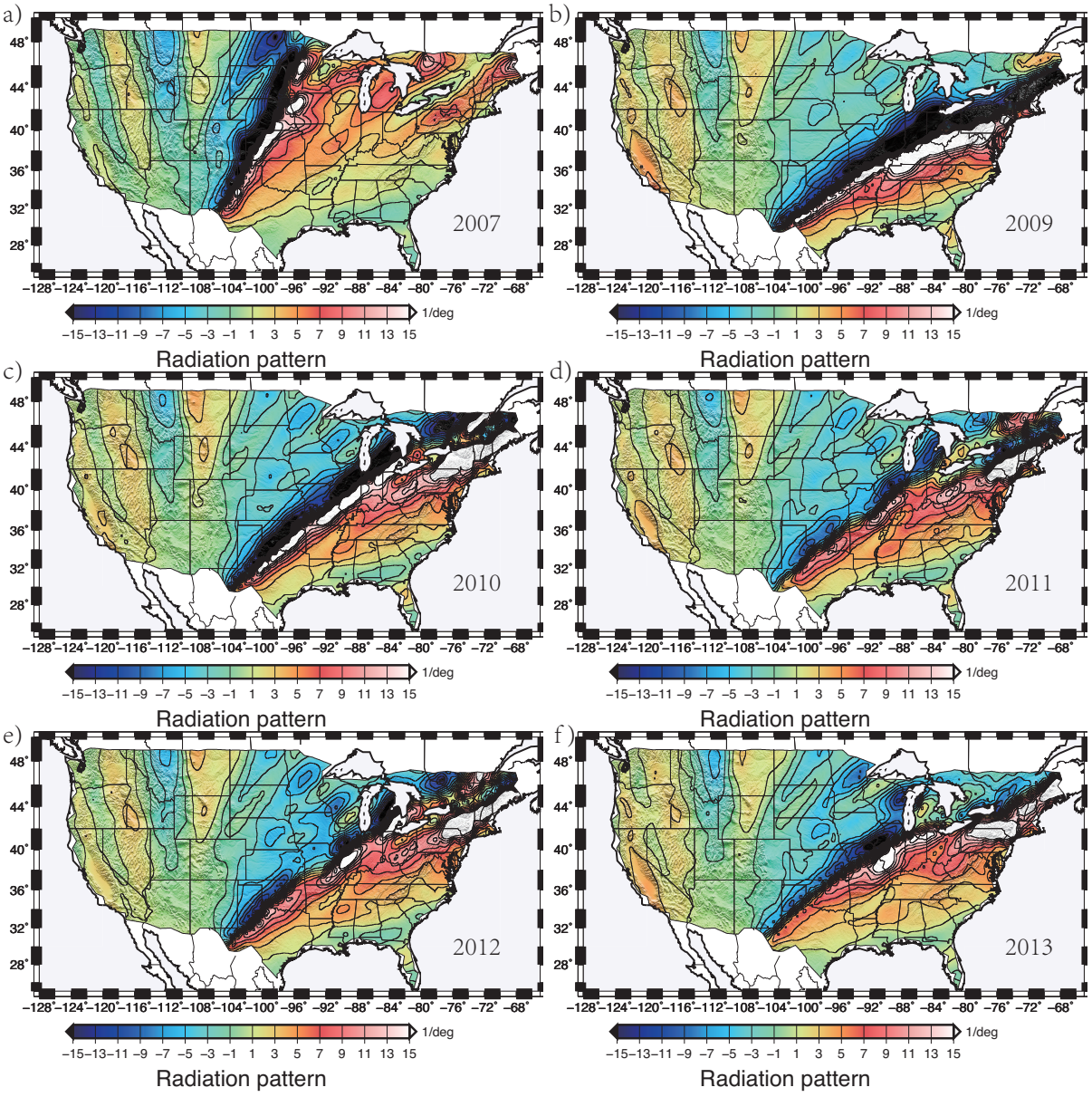

FIGURE 2.8: 60 s Rayleigh wave gradiometry parameter radiation pattern obtained from synthetic wavefields based on US_{22}.

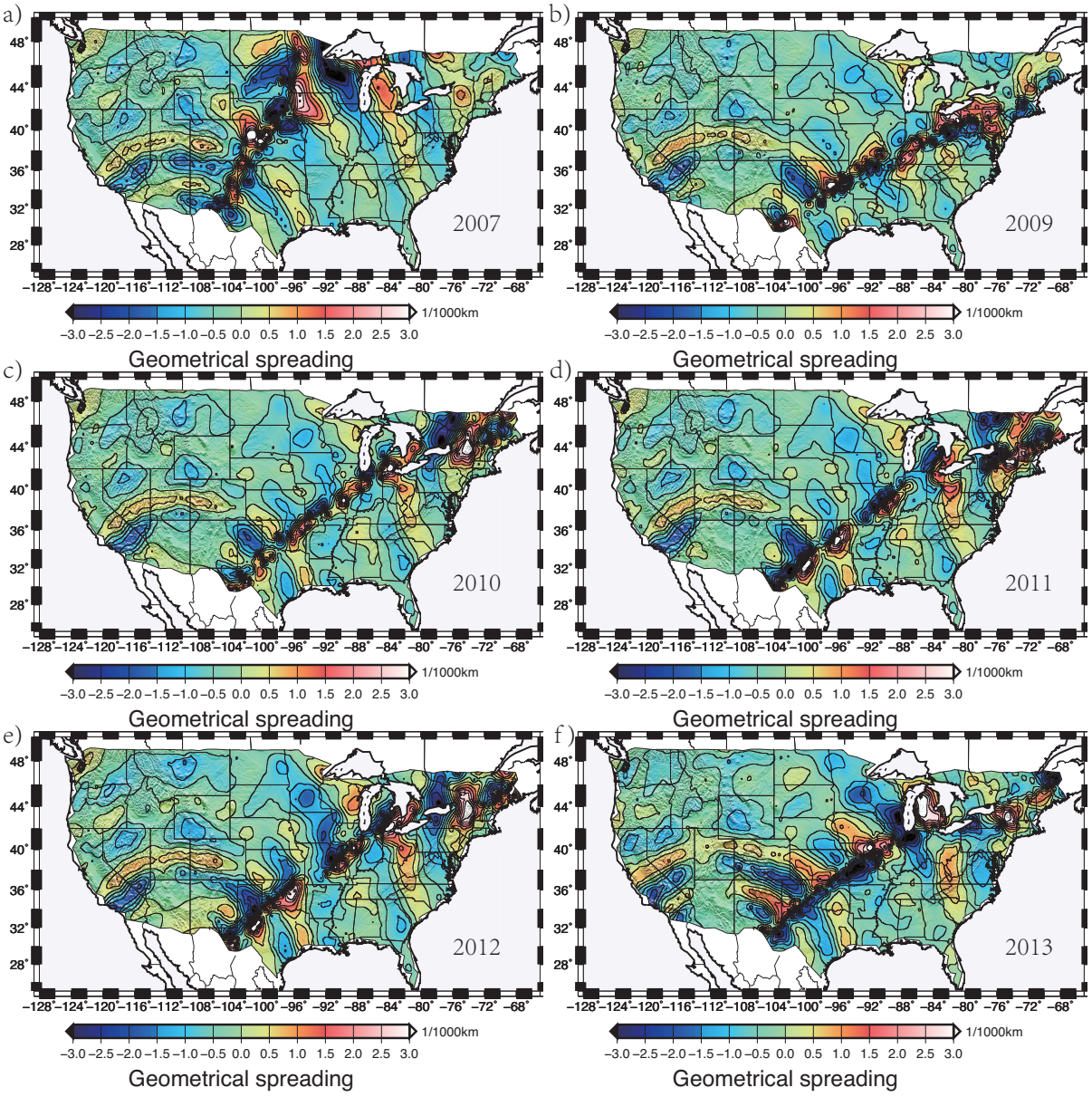

FIGURE 2.9: 60 s Rayleigh wave gradiometry parameter geometrical spreading obtained from synthetic wavefields based on US_{22}.

features in the central U.S. are two positive and negative trends from western Texas up into the northeast Great Lakes region. This can be understood by examining the same regions in Figure 2.7a, where $\vec{A}$-coefficient vectors (gradients of logarithmic amplitude) are in general orthogonal to propagation direction, radiating off of a major amplitude low.

Comparison of the radiation pattern in the composite solution (Figure 2.7c) with the patterns obtained from the high resolution synthetics (Figure 2.8) we observe very good agreement in the western U.S. and western Great Plains. In accord with the misfit of both the $\vec{A}$ and $\vec{B}$-coefficient fields (along with their respective gradient fields) with the synthetics, the composite patterns of radiation also show significant differences with the synthetics to the north, south, and east of the Great Lakes region.

The geometrical spreading reflects the amplitude variation parallel to the wave propagation direction (Equation (2.6)). Where the $\vec{A}$ vectors show components that are not orthogonal to the propagation direction, we expect to observe a non-zero value of geometrical spreading, and by the transport equation (2.8) we also expect to see non-zero values for $\nabla \cdot \vec{B}$. Indeed we observe a very close positive correlation between the geometrical spreading (Figure 2.7d) and $\nabla \cdot \vec{B}$ (Figure 2.7b), and they are both anti-correlated with the Laplacian of logarithmic amplitude (Figure 2.7a) for most regions.

Comparing the composite geometrical spreading patterns (Figure 2.7d) with the synthetic high resolution results (Figure 2.9) we observe very good agreement within the western U.S. The bifurcation of positive geometrical spreading zones within the the region of southern Missouri, along with the general patterns in the Great Lakes regions,

are not as well matched by the synthetics.

2.6 Local Amplification Factor

The transport equation [*Cerveny*, 2005] can be used to calculate the corrected amplitude decay for fundamental mode Rayleigh waves, which is linked directly to both the local amplification and intrinsic attenuation [*Lin et al.*, 2012]. *Lin et al.* [2012] used the local amplification to constrain phase velocity, density within the crust and upper mantle. There is a strong correlation (Figure 2.10c) between apparent amplitude decay (Figure 2.10a) and focusing/defocusing correction (Figure 2.10b). The same gradiometry parameters are estimated for 2011 synthetic event provided by Hejun Zhu, as shown in Figure 2.11. The apparent amplitude decay (Figure 2.11a) is also consistent with focusing/defocusing corrections (Figure 2.11b), as shown in Figure 2.11c. These patterns of apparent amplitude decay, focusing/defocusing corrections, and corrected amplitude decay can be used as additional constraints in the future to refine structural models when combined with full 3-D synthetic calculations.

2.7 Discussion and Conclusion

In summary, gradiometry parameters provide information that can be used for present and future structural studies. Analysis of the wavefields from six events that occurred in the Gulf of California show remarkable features that link the focusing and defocusing of energy with amplitude variations. A consistent pattern involves amplitude variations

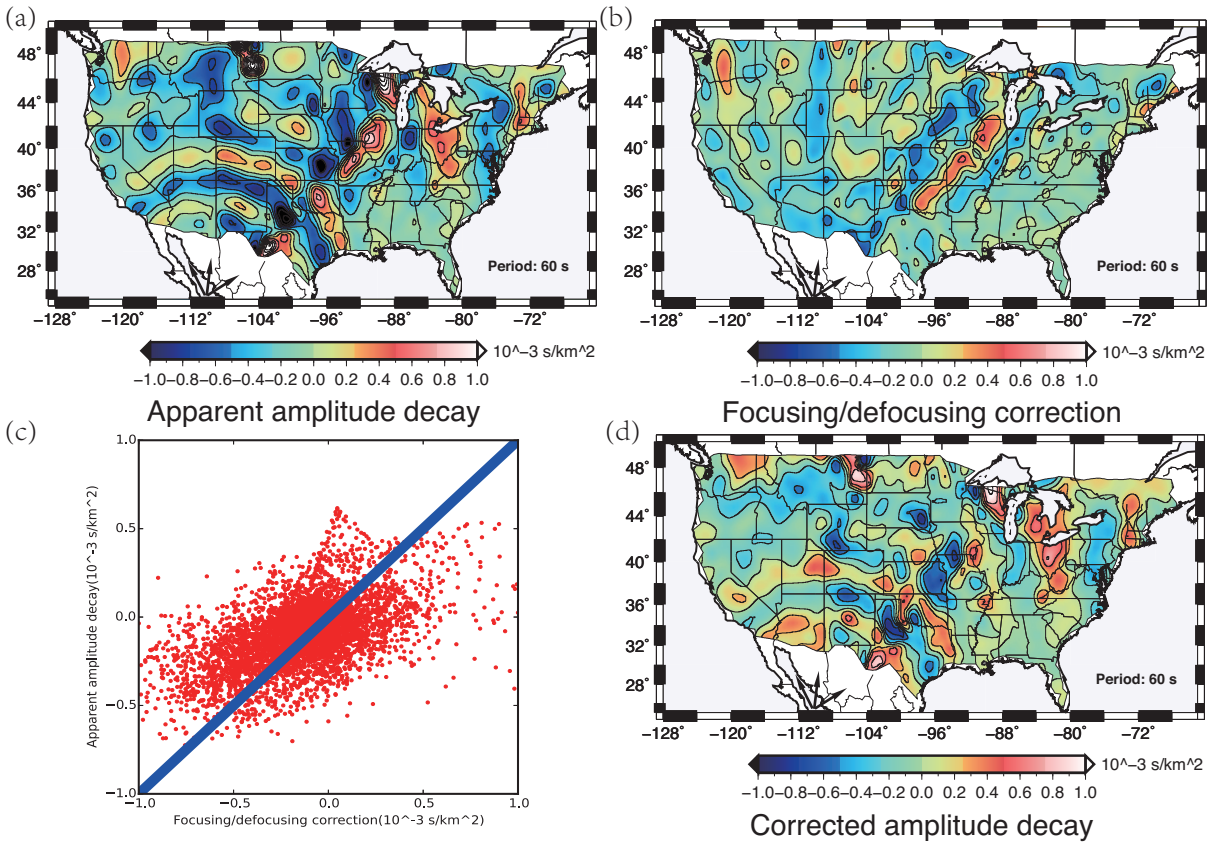

FIGURE 2.10: 60 s Rayleigh wave gradiometry products from real records of six Gulf of California events. (a) shows apparent amplitude decay and (b) shows focusing/defocusing correction, calculated from Figure 2.7a and 2.7b. (c) shows the correlation between apparent amplitude decay and focusing/defocusing correction, each red point corresponds to a grid point in the map. The blue line has a slope of 1. (d) shows the corrected amplitude decay, representing the differences between the apparent amplitude decay and the focusing/defocusing correction. The arrows represent the approximate wave propagation directions radiating from the sources.

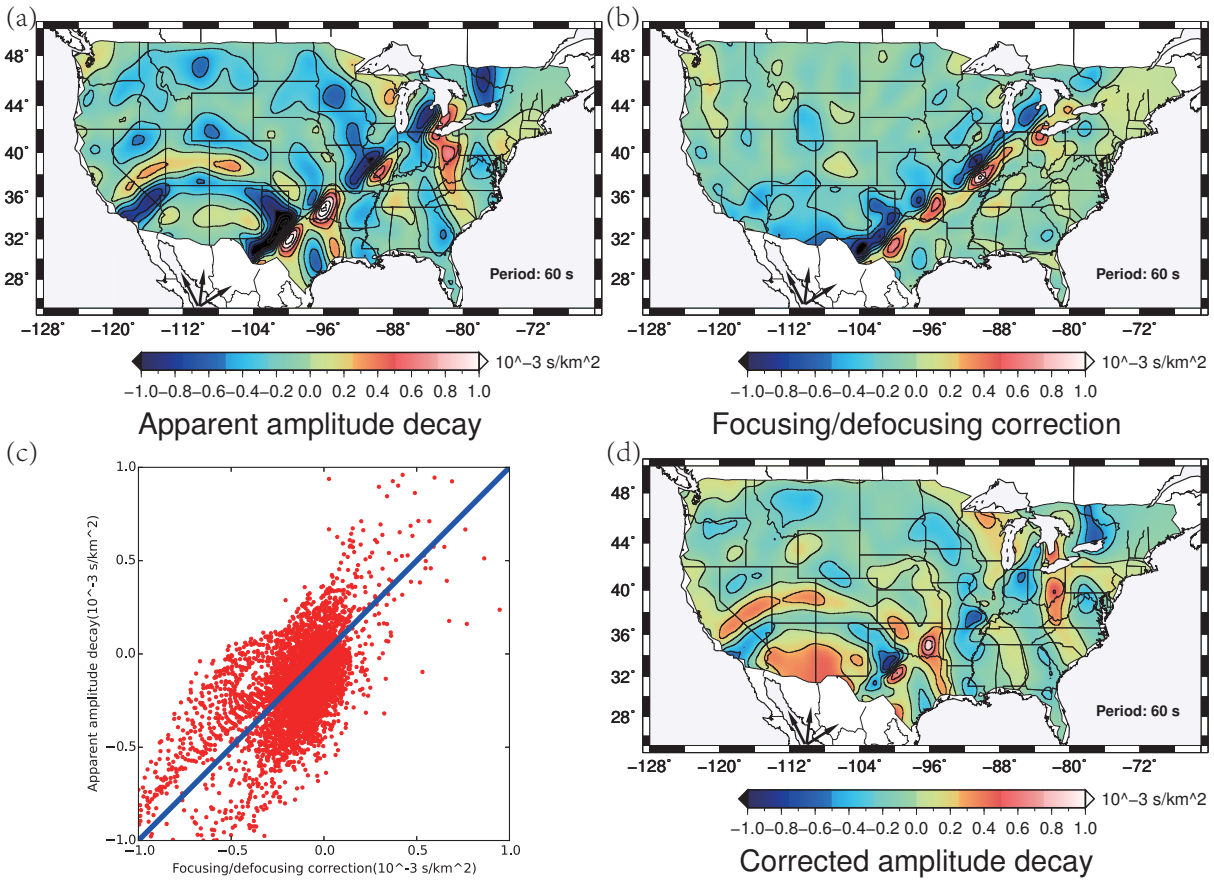

FIGURE 2.11: The same gradiometry parameters as in Figure 2.10, but obtained from synthetics of 2011 event based on US_{22}.

that are primarily in directions orthogonal to the propagation directions of the wavefields. Note that the $\vec{A}$ and $\vec{B}$-coefficients obtained separately from individual events show continuous patterns that are roughly independent to the absolute magnitudes of energy. The gradiometry products: radiation pattern and geometrical spreading can thus provide useful information about structures along the ray paths.

In general, by combining wavefields from six Gulf of California events, we are able to capture a single full wavefield radiated from a general source. The edges of amplitude lows dominate most zones of focusing/defocusing (Figure 2.5 and 2.3b). Major zones of focusing and defocusing, with large values of $\nabla \cdot \vec{A}$ and $\nabla \cdot \vec{B}$, start within central Texas and trend along a roughly linear zone to the Great Lakes region. The distributions of amplitudes recorded along this path are consistent with energies radiating out from directions corresponding to the strikes of the nodal plane ($\sim 40°$). We also found some disagreement between the observed trends of $\nabla \cdot \vec{A}$ and $\nabla \cdot \vec{B}$ along this low amplitude zone and trends predicted by the synthetics, particularly within the Great lakes regions. Outside the low amplitude zones, particularly within the western U.S. and western Great Plains, we found very good agreement between observed and synthetic patterns of gradiometry fields from US_{22}, but amplitudes of these fields are generally underestimated by the synthetics.

Compared with the gradiometry parameters obtained from real records, the synthetics from US_{00} [*Tromp et al.*, 2010], a smoothed Earth model, generally do not fit as well as synthetics from US_{22} [*Zhu et al.*, 2012], an updated Earth model. This suggests that the input structural model plays an important role in predicting both pattern and amplitude

of gradiometry parameters. The misfits of the gradiometry parameters in zones with strong focusing/defocusing can be viewed as an opportunity to refine the underlying structure, as we have shown by comparing results from two sets of synthetic calculations. Because the gradiometry parameters are sensitive to the input Earth structure, future studies can optimize the fit between predicted and observed gradiometry parameters. Because this will provide a broader set of wavefield observables, incorporating gradiometry technique has the potential to provide more rigorous structural interpretations from the full wavefield.

Chapter 3

Analysis of Rayleigh Wave Isotropic Structural Phase velocity

3.1 Introduction

One of the major goals of global, regional or locally deployed seismic arrays is to record seismic wavefields for the studies of earthquake source mechanisms and earth interior structures. With an average station spacing of 70 km, the USArray Transportable Array (TA) has provided an opportunity to study the evolution of the North America continent using various techniques. With the coverage of USArray arriving in the eastern U.S., the latest studies coming out of traditional inversion techniques have revealed many exciting details about the crust and upper mantle structure beneath the eastern U.S. [*Burdick et al.*, 2014; *Lin et al.*, 2014; *Schmandt and Lin*, 2014; *Jin and Gaherty*, 2015; *Liu and Holt*, 2015; *Porter et al.*, 2016; *Pollitz and Mooney*, 2016]. *Liang and Langston* [2009] first applied wave gradiometry in the western U.S. to extract dynamic phase velocity, azimuth variation, geometrical spreading and radiation pattern for 60 s - 150 s Rayleigh waves. *Liu and Holt* [2015] further advanced the gradiometry technique by estimating spatial gradients in a continuous field and combining it with Helmholtz equation solutions

to estimate structural phase velocities for 20 s - 150 s Rayleigh waves in the eastern U.S.

In this study, we first briefly review the primary components of gradiometry theory and the reader is referred to *Liu and Holt* [2015, 2016a] for further details. Wave gradiometry is then applied to 696 earthquakes between 2007 and 2014, with magnitudes greater than 5.0 and focal depths shallower than 50 km. During this period, a total amount of 1,739 USArray TA stations were deployed across the contiguous U.S. After stacking, averaging, and smoothing the structural phase velocities from all events, we present the 20 s - 150 s Rayleigh wave isotropic velocities across the contiguous U.S., as a new data product that can be used in shear velocity inversion studies [*Porter et al.*, 2016]. The isotropic phase velocity variances and standard deviations are also estimated at each seismic station. We then discuss the isotropic velocities in light of some of the major structural features and the evolution of the lithosphere within the contiguous U.S. for various period bands.

One goal of this study is to provide data products of the gradiometry parameters obtained from the 696 events recorded by the entire USArray for future analysis. For each event within each period we provide archives of gradiometry parameters: $\vec{A}$, $\vec{B}$, $\nabla \cdot \vec{A}$, $\nabla \cdot \vec{B}$ and gradiometry products: radiation pattern and geometrical spreading, which provide details on the local curvature of the wavefield, the focusing/defocusing of energy and its relation to amplitude variations. These new constraints can potentially improve our understanding of the actual wavefields and the viable structural interpretations from source to receiver.

3.2 Methodology

The link between wave gradiometry and Helmholtz equation solution, and their applications to the USArray TA stations in the eastern U.S., have been discussed in detail in *Liu and Holt* [2015]. For the convenience of discussion, some equations and techniques are reviewed below.

In a Cartesian coordinate system, differentiating wave equation solution gives us a set of equations, which link the displacements, the spatial gradients and the time derivatives of displacement field, to important wavefield propagation parameters [*Langston*, 2006, 2007a,b,c; *Liang and Langston*, 2009]:

$$\frac{\partial u}{\partial x} = A_x \cdot u + B_x \cdot \frac{\partial u}{\partial t} \tag{3.1}$$

$$\frac{\partial u}{\partial y} = A_y \cdot u + B_y \cdot \frac{\partial u}{\partial t} \tag{3.2}$$

$$A_x = \frac{\partial G}{\partial x} \cdot \frac{1}{G} \qquad A_y = \frac{\partial G}{\partial y} \cdot \frac{1}{G} \tag{3.3}$$

$$B_x = -\Big[p_x + \frac{\partial p_x}{\partial x}(x - x_0)\Big] \qquad B_y = -\Big[p_y + \frac{\partial p_y}{\partial y}(y - y_0)\Big] \tag{3.4}$$

where u represents the displacement field, G represents the wave amplitude variation across space, $\vec{A}$ and $\vec{B}$ are two unknown coefficients that we are trying to solve for, and p_x and p_y are components of the horizontal slowness in the x and y directions, respectively. By assuming that the spatial gradients and associated wave parameters define a spatially

variable and continuous field, we solve for the local values of phase velocity at each seismic station (x_0, y_0):

$$B_x(x_0) = -p_x(x_0) \qquad B_y(y_0) = -p_y(y_0) \tag{3.5}$$

Each subarray consists of one master station and around twenty supporting stations within 200 km radius. The reducing velocity method is applied to shift the waveforms of supporting stations relative to the master station, which may effectively decrease the phase move-out and spatial gradients variations within the subarray [*Langston*, 2007b]. As a result, any spatial gradients of the displacement field in equations (3.1) and (3.2) are associated with normalized gradients of amplitude ($\vec{A}$-coefficients) and perturbations to the initial slowness estimate ($\vec{B}$-coefficients) [*Liang and Langston*, 2009]. The spatial gradients of displacement fields are estimated using a bi-cubic spline interpolation [*Haines and Holt*, 1993; *Beavan and Haines*, 2001]. The time derivatives of displacements are obtained by differentiating displacement waveforms with respect to time. Given the spatial gradients, displacements, and time derivatives of displacements, we are able to solve for A_x, A_y, B_x and B_y using an iterative, damped least-squares inversion through equations (3.1) and (3.2).

Liu and Holt [2015] have shown that the phase velocities determined from gradiometry parameter $\vec{B}$-coefficients through equation (3.5) are almost identical to the dynamic phase velocities determined from the gradients of phase traveltime method employed by [*Lin and Ritzwoller*, 2011a]. Based on this empirical similarity, *Liu and Holt* [2015] have made the assumption that the $\vec{B}$-coefficient gives the approximate value of the dynamic phase velocity. However, the dynamic phase velocity depends not only on the underlying

medium, but also on the local geometry of the wavefield [*Wielandt*, 1993]. Thus, it can neither be directly attributed to the structure nor be used as an input for tomographic structure inversion [*Friederich et al.*, 1995; *Pollitz and Snoke*, 2010]. The structural phase velocity, however, is independent of the specific geometry of the wavefield or source properties and it's more appropriate for surface wave tomography studies [*Wielandt*, 1993; *Friederich et al.*, 1995; *Lin and Ritzwoller*, 2011a; *Jin and Gaherty*, 2015]. *Liu and Holt* [2015] showed the local relationship between the dynamic and structural phase velocity in terms of gradiometry parameters. The structural phase velocity involves a geographically localized correction to the dynamic phase velocity via the real part of the Helmholtz equation solution:

$$\frac{1}{c^2} = |\nabla\tau|^2 - \frac{\nabla^2 G}{G} \cdot \frac{1}{\omega^2} \tag{3.6}$$

where c is the structural phase velocity, τ is the phase traveltime, $\nabla\tau$ is the gradient of phase traveltime, G is the wave amplitude variation as in equation (3.3), and ω is the angular frequency. The term $\nabla\tau$ gives the dynamic phase velocity [*Wielandt*, 1993] and it's approximately equal to the $\vec{B}$-coefficients [*Liu and Holt*, 2015]. Meanwhile from equation (3.3), we know:

$$\vec{A}^2 + \nabla \cdot \vec{A} = (\frac{\nabla G}{G})^2 + \frac{\nabla^2 G \cdot G - (\nabla G)^2}{G^2} = \frac{\nabla^2 G}{G} \tag{3.7}$$

Combining equations (3.6) and (3.7), the structural phase velocity can be calculated by subtracting the amplitude correction term [*Wielandt*, 1993; *Lin and Ritzwoller*, 2011a]

from the dynamic phase velocity:

$$\frac{1}{c^2} \approx |\vec{B}|^2 - \frac{\vec{A}^2 + \nabla \cdot \vec{A}}{\omega^2} \tag{3.8}$$

Liu and Holt [2015] experimented with two events: 2009 April 7, earthquake near Kuril Islands and 2007 February 14, earthquake near Easter Island for 60 s Rayleigh wave. They found a close match between dynamic/structural phase velocities obtained using wave gradiometry and estimates obtained from Helmholtz tomography [*Lin and Ritzwoller*, 2011a] and multi-channel cross-correlation methods [*Jin and Gaherty*, 2015]. This not only validates our previous assumption that the $\vec{B}$-coefficient gives us the approximate value of the dynamic phase velocity, but also confirms that the structural phase velocity is more appropriate for surface wave studies. *Liu and Holt* [2015] also found that the starting velocity model has little effect on the final model after 4 iterations.

The structural phase velocities are calculated separately for each earthquake, and then combined, stacked, averaged, and smoothed to obtain the isotropic velocities. The smoothing technique applied here involves several steps: 1) The averaged velocities at the station locations are fitted with the Generic Mapping Tool [*Wessel et al.*, 2013] (GMT) Surface command. This provides estimates of structural phase velocity at all points but some irregularities persist. 2) We thus average the values obtained from the previous step within a $0.5^\circ \times 0.5^\circ$ grid network that spans the contiguous U.S. region. 3) We then apply a smoothing method [*Haines et al.*, 1998] to these averaged values that preserves total integrals over the areas. The velocity at each knotpoint on the grid network is calculated based on averages of velocities within four surrounding grid areas. 4) The velocity within

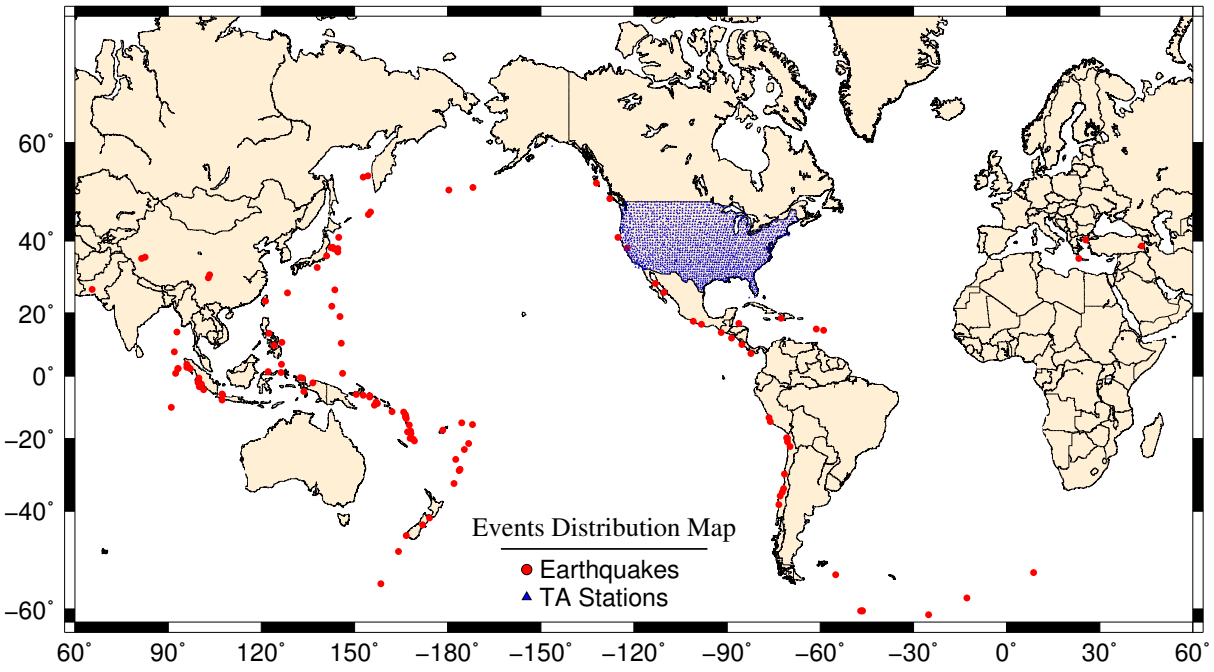

FIGURE 3.1: Earthquakes analyzed in this study and USArray TA stations distribution map.

each grid area is estimated based on the average of the velocities of the knotpoints at four corners of the grid.

The imaginary part of the Helmholtz equation solution (also referred to as the transport equation [*Cerveny*, 2005]) can be written, using gradiometry parameters, as follows:

$$2 \cdot \vec{B} \cdot \vec{A} - \nabla \cdot \vec{B} = 0 \tag{3.9}$$

This compatibility relation not only gives us insights into how the patterns of gradiometry parameters are related to energy focusing/defocusing, but also provides constraints on a new observable - the local amplification factor, which can be used for elastic velocity and density variation analysis [*Lin et al.*, 2012].

3.3 Analysis of Isotropic Structural Phase Velocity Maps

We have applied wave gradiometry to 696 earthquakes from 2006 to 2014 recorded by 1,739 USArray TA stations (Figure 3.1). The 20 s - 150 s Rayleigh wave structural phase velocities are stacked, averaged, and then smoothed to obtain isotropic velocities, which are presented in 4 separate 4-panel figures where the color scale is adjusted for each period. The variances and standard deviations for structural phase velocities are estimated at each seismic station by combining results from all earthquakes. In addition, gradiometry parameters: $\vec{A}$, $\vec{B}$, $\nabla \cdot \vec{A}$, $\nabla \cdot \vec{B}$ and gradiometry products: radiation pattern and geometrical spreading for all events are archived and can be freely accessed from `https://github.com/mickeyliu5/gradiometry_results`.

In average, the differences between the dynamic and structural phase velocities decrease from 0.4 km/s for individual events to 0.1 km/s for the stacked isotropic results. However, we do observe that these differences increase with period (Figure 3.2), especially for periods longer than 50 s. The standard deviations of dynamic phase velocity (Figure 3.3a, 3.3c) are also larger than that of structural phase velocity (Figure 3.3b, 3.3d) for periods longer than 50 s. We thus argue that the structural phase velocity should be used for structure interpretation instead of dynamic phase velocity, at least for periods longer than 50 s for the USArray TA station configuration [*Lin and Ritzwoller*, 2011a; *Liu and Holt*, 2015].

Rayleigh wave isotropic structural phase velocities in the western and central U.S.

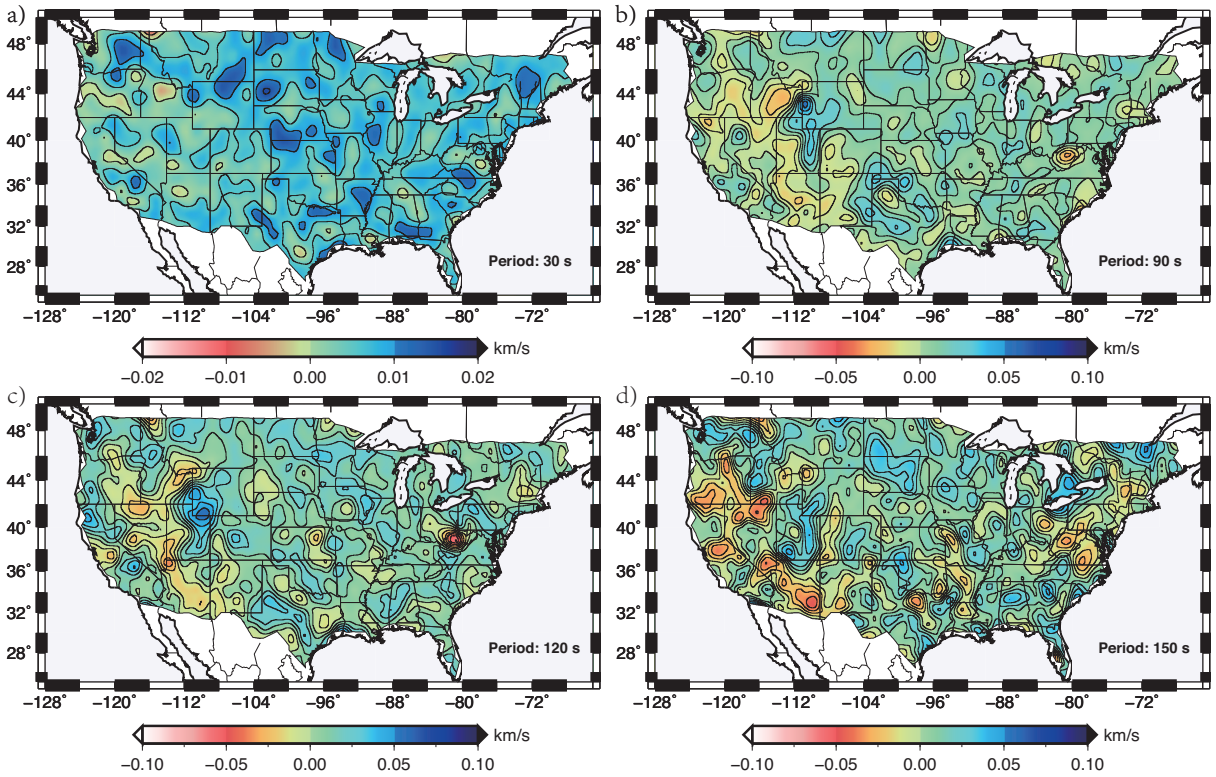

FIGURE 3.2: The difference between isotropic structural and dynamic phase velocities for the 30 s - 150 s Rayleigh waves. Contours are separated by intervals of 0.01 km/s.

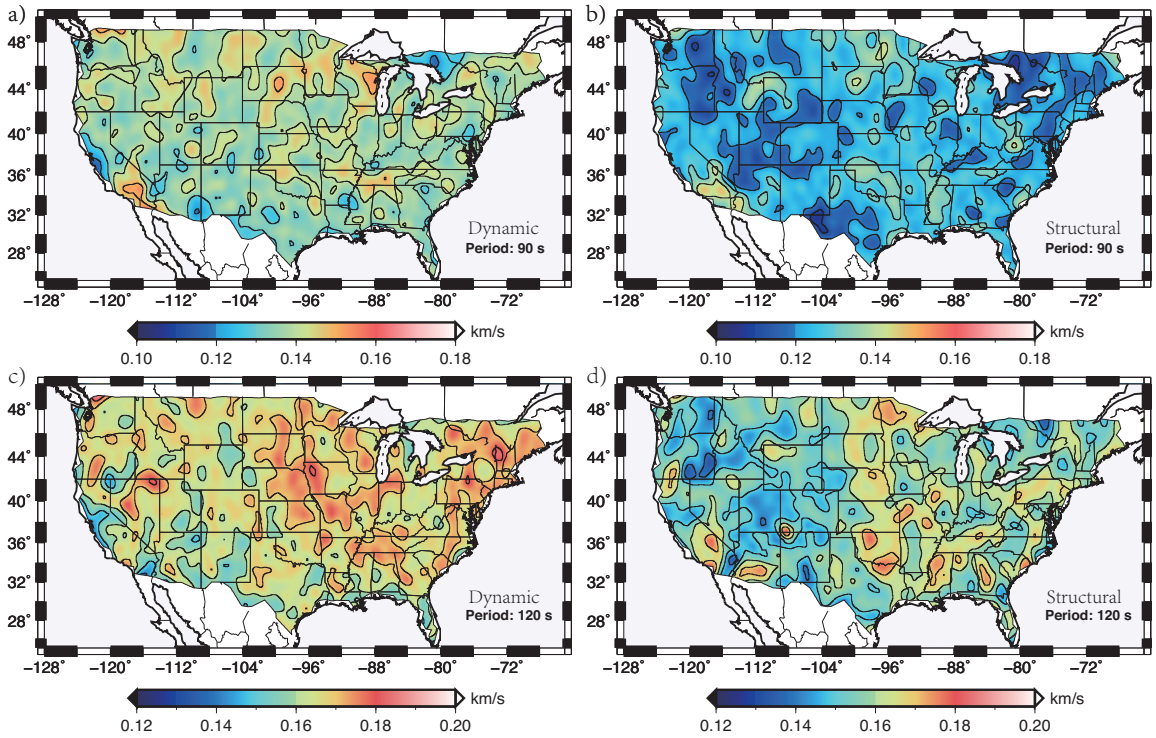

FIGURE 3.3: The standard deviations for the 90 s Rayleigh wave (a) dynamic and (b) structural phase velocities. The standard deviations for the 120 s Rayleigh wave (c) dynamic and (d) structural phase velocities. Contours are separated by intervals of 0.01 km/s.

are similar to previously published results [*Lin and Ritzwoller*, 2011a; *Pollitz and Snoke*, 2010; *Shen et al.*, 2013a; *Pollitz and Mooney*, 2014]. For the entire contiguous U.S., our results are consistent with results obtained from a multichannel cross-correlation method [*Jin and Gaherty*, 2015] and "nonplane wave" imaging methodology [*Pollitz and Mooney*, 2016]. Our results also appear to be qualitatively consistent with body wave tomography results estimated by *Schmandt et al.* [2015], who resolved a shear velocity model from multimode receiver function stacking, Rayleigh wave dispersion and ellipticity measurements.

3.3.1 Isotropic Velocities within 20 s - 30 s Period

For the period range of 20 s - 30 s (Figure 3.4, 3.5, 3.6, 3.7) the lowest velocities (3.3 - 3.5 km/s) are found in the Colorado Rockies (CR), the Rio Grande Rift (RGR), the Snake River Plane (SRP) and Yellowstone (YS), the eastern (Wasatch Front (WF)) and western edges of the Great Basin (GB), the Cascade Volcanic Arc (CVA), and the Green River Basin (GRB) (for shortest periods of 20 s - 22 s). Prominent high velocity zones are observed in the Columbia Basin (CB) in eastern Washington, southern Arizona, and western California in the Central Valley (CV). There is a transition from lower phase velocities to higher velocities along the approximate boundary between the Trans-Hudson (T-H) orogenic belt and the Superior Craton (SC) [*Whitmeyer and Karlstrom*, 2007]. This velocity transition fades within southern South Dakota where the Yavapai Province suture meets with the Trans-Hudson (T-H) and Superior Craton (SC) [*Whitmeyer and Karlstrom*, 2007]. We observe a low velocity anomaly corresponding with the location of

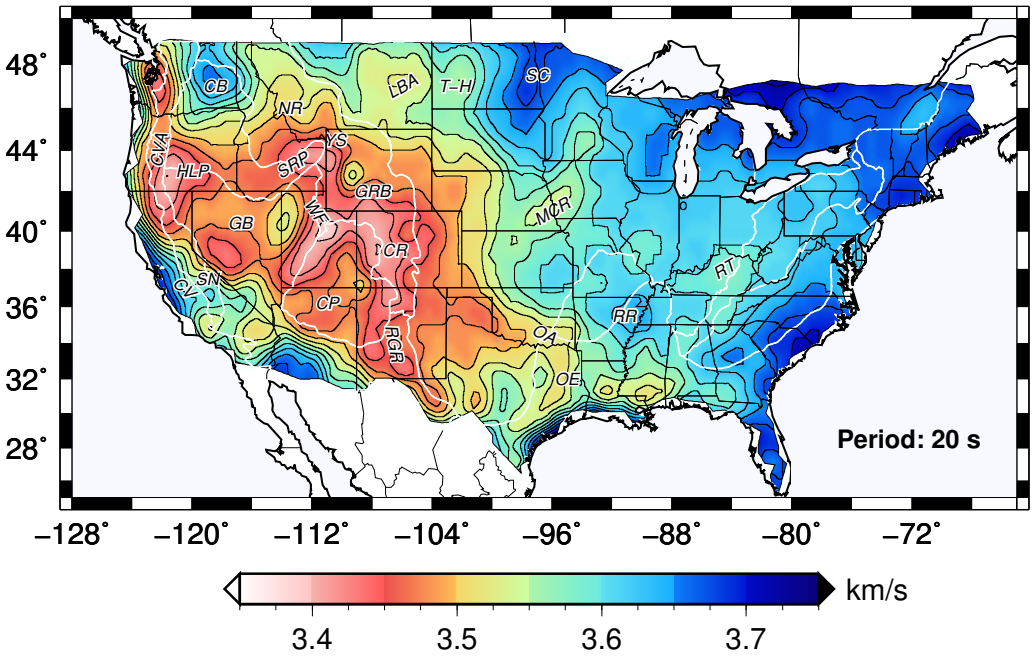

FIGURE 3.4: Isotropic phase velocity results for the 20 s Rayleigh wave. Contours are separated by intervals of 0.05 km/s, including all maps below. White lines show approximate geographic province boundaries, which are indicated as: CB, Columbia Basin; CP, Colorado Plateau; CR, Colorado Rockies; CVA, Cascade Volcanic Arc; CV, Central Valley; GB, Great Basin; GRB, Green River Basin; HLP, High Lava Plains; LBA, Little Belt Arc; MCR, Mid Continent Rift; NR, North Rocky Mountain; OA, Oklahoma Aulocogen; OE, Ouachita Embayment; RGR, Rio Grande Rift; RR, Reelfoot Rift; RT, Rome Trough; SN, Sierra Nevada; SRP, Snake River Plain; SC, Superior Craton; T-H, Trans-Hudson; WF, Wasatch Front; YS, Yellowstone.

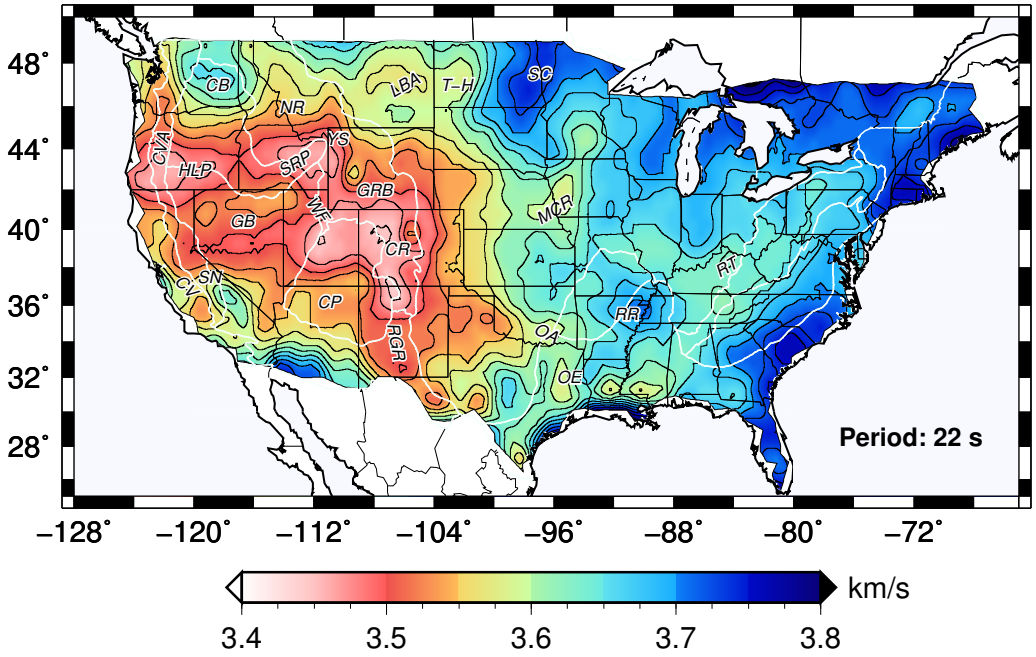

FIGURE 3.5: Isotropic phase velocity results for the 22 s Rayleigh wave.

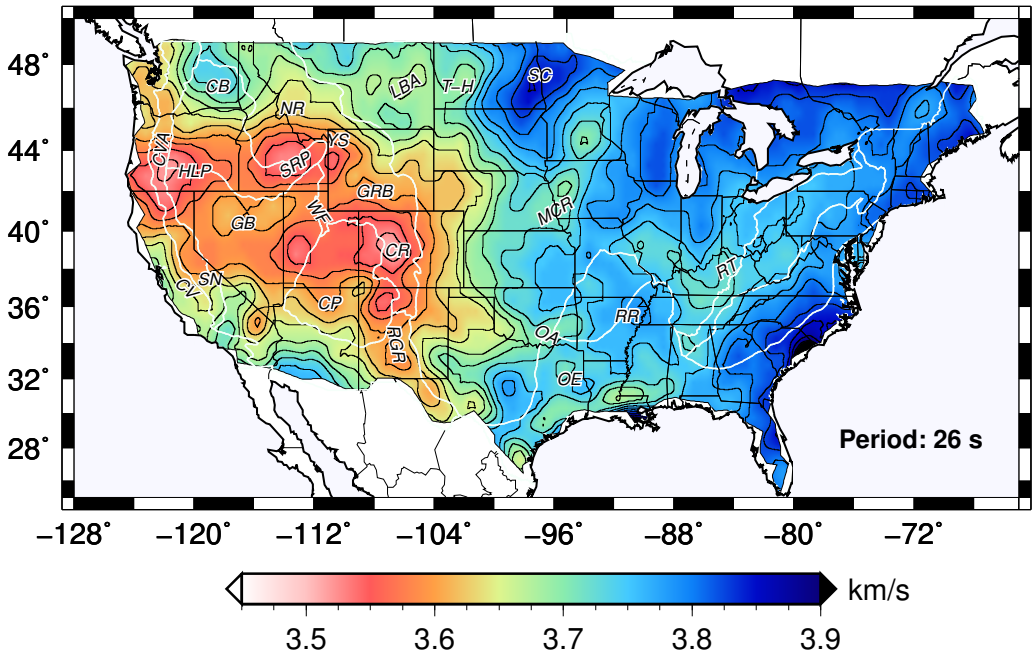

FIGURE 3.6: Isotropic phase velocity results for the 26 s Rayleigh wave.

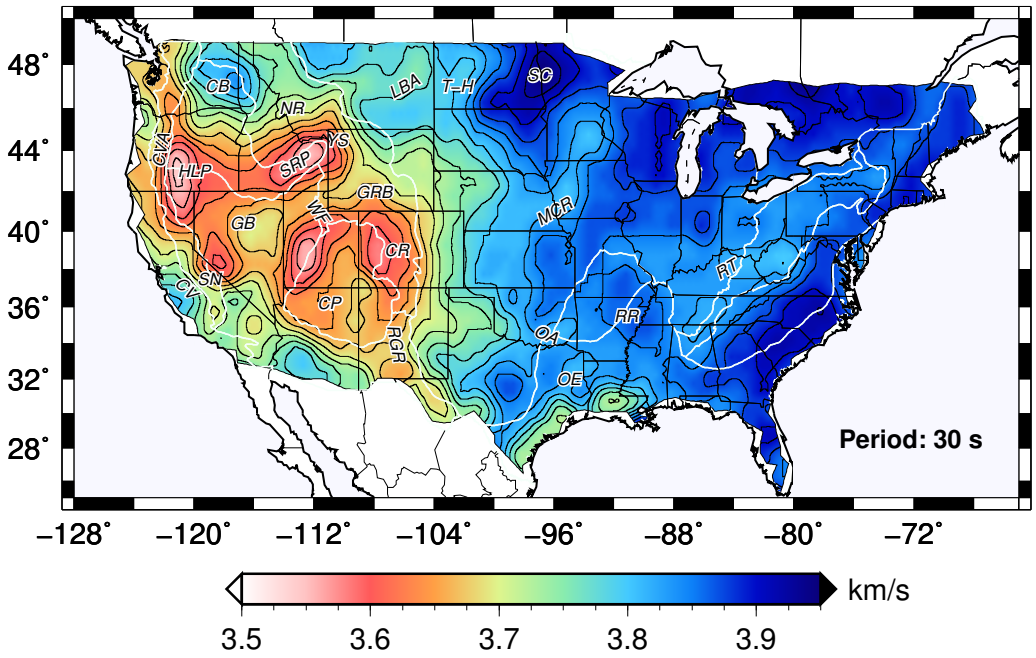

FIGURE 3.7: Isotropic phase velocity results for the 30 s Rayleigh wave.

the Mid Continent Rift (MCR) within southern Minnesota, Iowa, and southeast Nebraska. This anomaly has already been discovered in recent studies [*Shen et al.*, 2013b; *Pollitz and Mooney*, 2014, 2016]. The Superior, Penokean, Yavapai, and Mazatzal crust [*Whitmeyer and Karlstrom*, 2007] in the Great Lakes region show higher velocities, with a transition to slightly lower velocities along the approximate Grenville Front.

There is a low velocity anomaly along the Oklahoma Aulocogen (OA) [*Pollitz and Mooney*, 2014]. Phase velocities below the Reelfoot Rift (RR) are relatively fast, which agrees with inferences of a "rift pillow" within the underlying crust there [*Stuart et al.*, 1997; *Pollitz and Mooney*, 2014; *Schmandt et al.*, 2015]. Further to the northeast within Kentucky, a low velocity anomaly may correspond to the Rome Trough (RT) [*Pollitz and Mooney*, 2016]. The 30 s result shows higher velocities within central Texas. Lower velocities, however, are observed in southern Texas, Louisiana, and Mississippi, associated

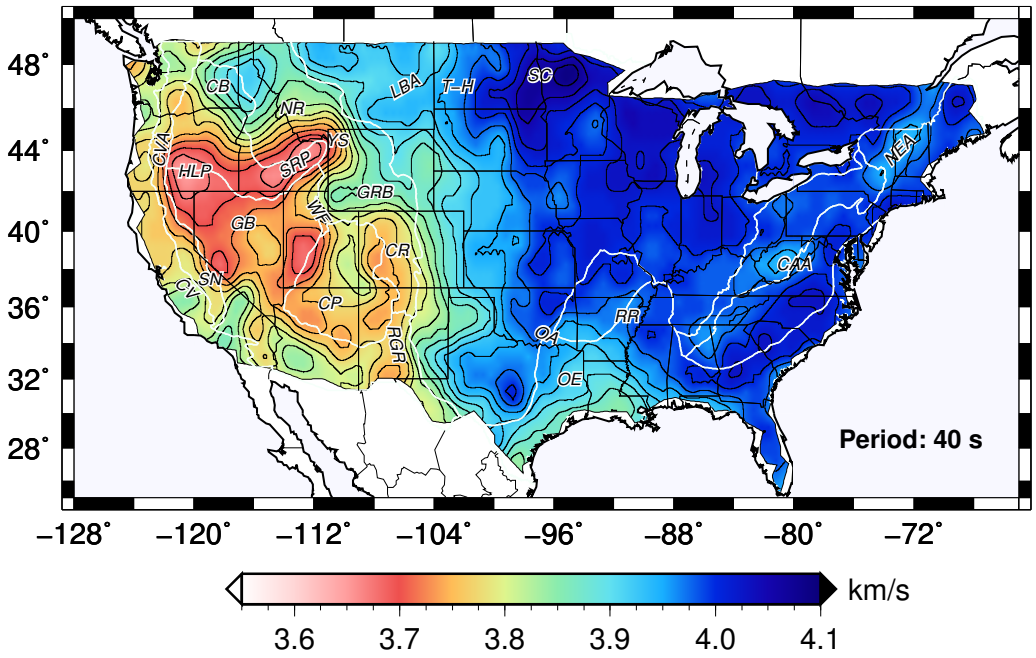

FIGURE 3.8: Isotropic phase velocity results for the 40 s Rayleigh wave. Geographic features as indicated: CAA, Central Appalachian Anomaly; NEA, Northeast Anomaly.

with the Gulf Coast thick sedimentary basins (20 s - 30 s). For the period range of 20 s - 30 s the eastern seaboard of the U.S. (east of the Laurentian margin) has higher phase velocities in comparison with the generally lower phase velocities in the Appalachian foreland basins, which lie to the west of accreted Appalachian terranes [*Keller and Hatcher*, 1999; *Cook and Oliver*, 1981].

3.3.2 Isotropic Velocities within 40 s - 70 s Period

For the period range of 40 s - 70 s (Figure 3.8, 3.9, 3.10, 3.11) the most obvious feature is the velocity contrast between the western U.S. and the Central and Eastern U.S. (CEUS). Major features in the western U.S. are the low phase velocities that rim the edges of the Colorado Plateau (CP) and Great Basin (GB) [*Levander et al.*, 2011], and low velocities

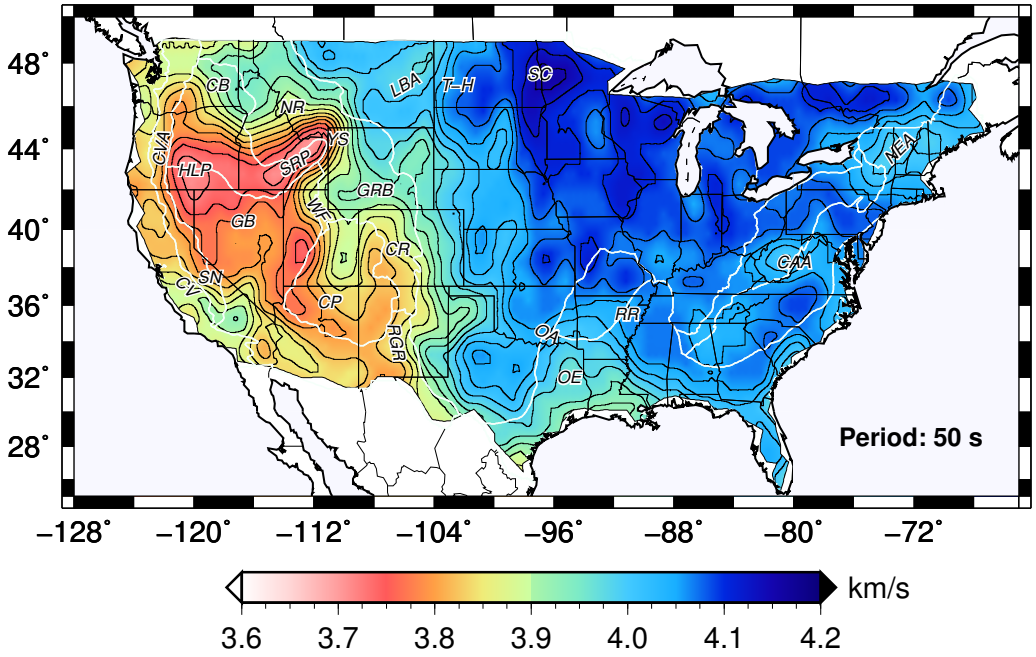

FIGURE 3.9: Isotropic phase velocity results for the 50 s Rayleigh wave.

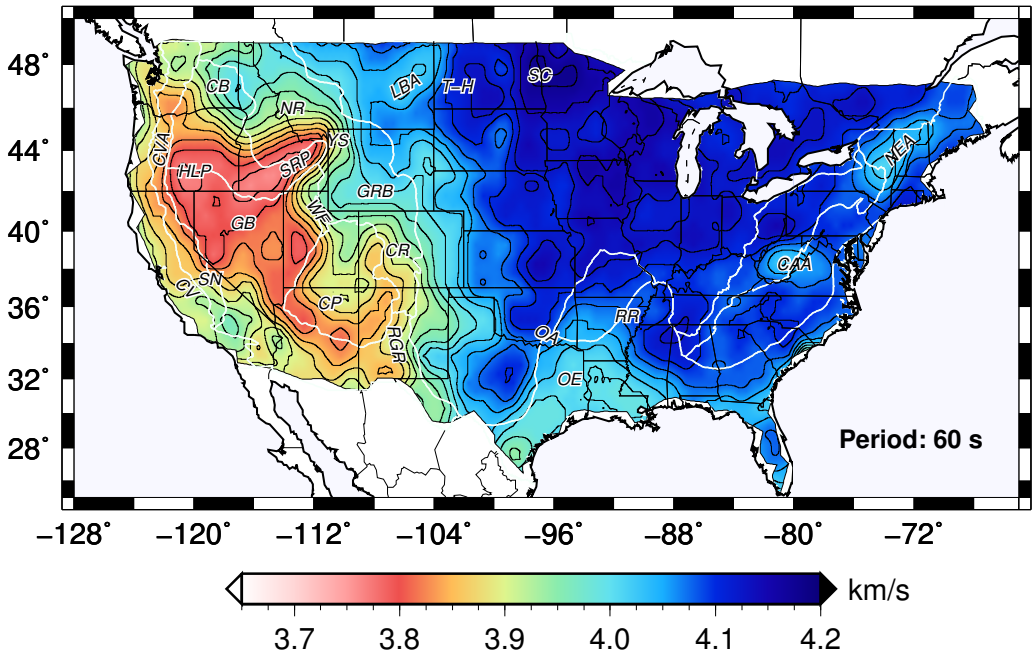

FIGURE 3.10: Isotropic phase velocity results for the 60 s Rayleigh wave.

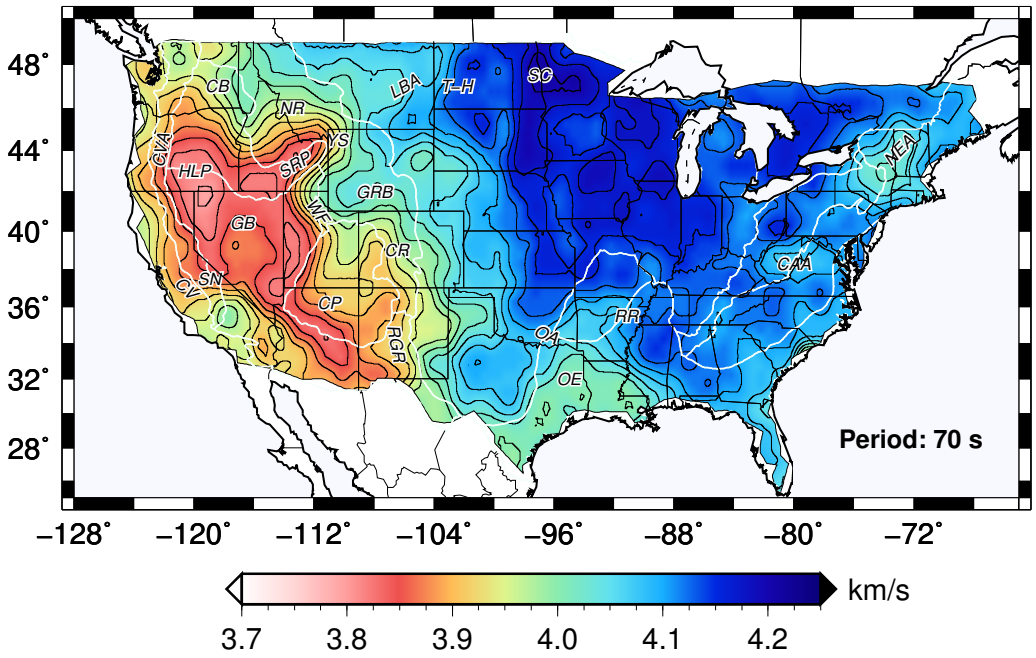

FIGURE 3.11: Isotropic phase velocity results for the 70 s Rayleigh wave.

in the Snake River Plane (SRP) and High Lava Plains (HLP) [*Wagner et al.*, 2010; *Roth et al.*, 2008]. We see generally higher phase velocities beneath and adjacent to the west of southern Sierra Nevada (SN), suggesting that we are observing the Isabella anomaly [*Benz and Zandt*, 1993; *Jones et al.*, 1994; *Schmandt and Humphreys*, 2010; *Jones et al.*, 2014], as well as higher velocities east of the Sierra Nevada (SN) within California, but this latter feature is not well resolved spatially.

Within this period range, the transition to highest phase velocities occurs along a roughly N-S trend through the central portions of North and South Dakota, Nebraska, Kansas, Oklahoma, and through central Texas. In the north this line corresponds approximately with the Trans-Hudson (T-H) and Superior Craton (SC) boundary. However, to the south this trend cuts across the Yavapai and Mazatzal terrane boundaries [*Whitmeyer and Karlstrom*, 2007] and it more closely follows the line of transition between

Central Lowland and Great Plains [*Fenneman*, 1917]. The lower phase velocities within the Ouachita Embayment (OE), suggest that the crustal and upper mantle structures have been modified by rifting during the Cambrian [*Thomas and Astini*, 1996; *Thomas*, 2011] and possibly further by collision during the Ouachita Marathon orogeny and subsequent Pangea breakup [*Porter et al.*, 2016]. The lower velocity anomaly associated with the Mid Continent Rift (MCR) in 20 s - 30 s periods (Figure 3.4, 3.5, 3.6, 3.7) is no longer present within this period range of 40 s - 70 s.

We observe two distinct low-velocities anomalies in the eastern U.S, one centered along the Virginia - West Virginia state boundary (referred to as the Central Appalachian Anomaly (CAA)), and the other located in Vermont, New Hampshire and easternmost New York (referred to as the Northeast Anomaly (NEA)). The locations of both anomalies coincide quite well with Rayleigh wave velocity results in eastern U.S. from *Liu and Holt* [2015], surface wave tomography results from *Jin and Gaherty* [2015]; *Pollitz and Mooney* [2016], and body wave velocity models at depths of $\sim$ 60 - 300 km obtained by *Schmandt and Lin* [2014]. *Porter et al.* [2016] jointly inverted phase velocity results from ambient noise tomography and wave gradiometry analysis to solve for shear velocity structure within the continental U.S. and they found that both CAA and NEA extend to considerable depths within the lithosphere. *van der Lee and Frederiksen* [2005] revealed the Northeast Anomaly (NEA) feature in their 3-D S-velocity model of upper mantle beneath U.S. even prior to the arrival of USArray. *Schmandt and Lin* [2014] and *Pollitz and Mooney* [2016] pointed out that the center of CAA corresponds with an Eocene ($\sim$47 Ma) swarm of basaltic volcanism [*Mazza et al.*, 2014]. *Eaton and Frederiksen* [2007] and

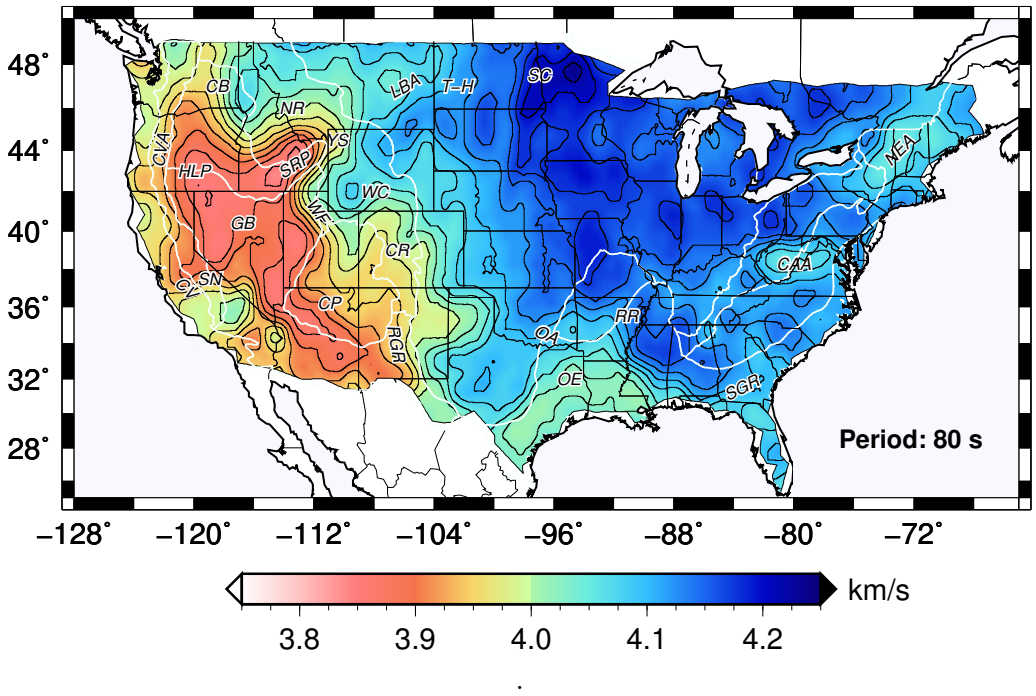

FIGURE 3.12: Isotropic phase velocity results for the 80 s Rayleigh wave. Geographic features as indicated: SGR : South Georgia Rift, WC: Wyoming Craton.

Villemaire et al. [2012] claimed the Northeast Anomaly (NEA) coincides with the inferred track of Great Meteor hotspot (∼200 - 110 Ma), which extends from northern Hudson bay to the northeast U.S. coast, and continues southeast as a chain of seamounts into the Atlantic ocean [*Duncan*, 1984].

3.3.3 Isotropic Velocities within 80 s - 110 s Period

Phase velocity results for the 80 s - 110 s Rayleigh waves (Figure 3.12, 3.13, 3.14, 3.15) show prominent low velocity features in the western U.S. in the Snake River Plane (SRP), High Lava Plain (HLP), eastern Great Basin (GB), along the western edge of Colorado Plateau (CP), and in southern Arizona. A tongue of high velocities extends from the Wyoming Craton (WC) into the central Colorado Plateau (CP). Higher phase velocity

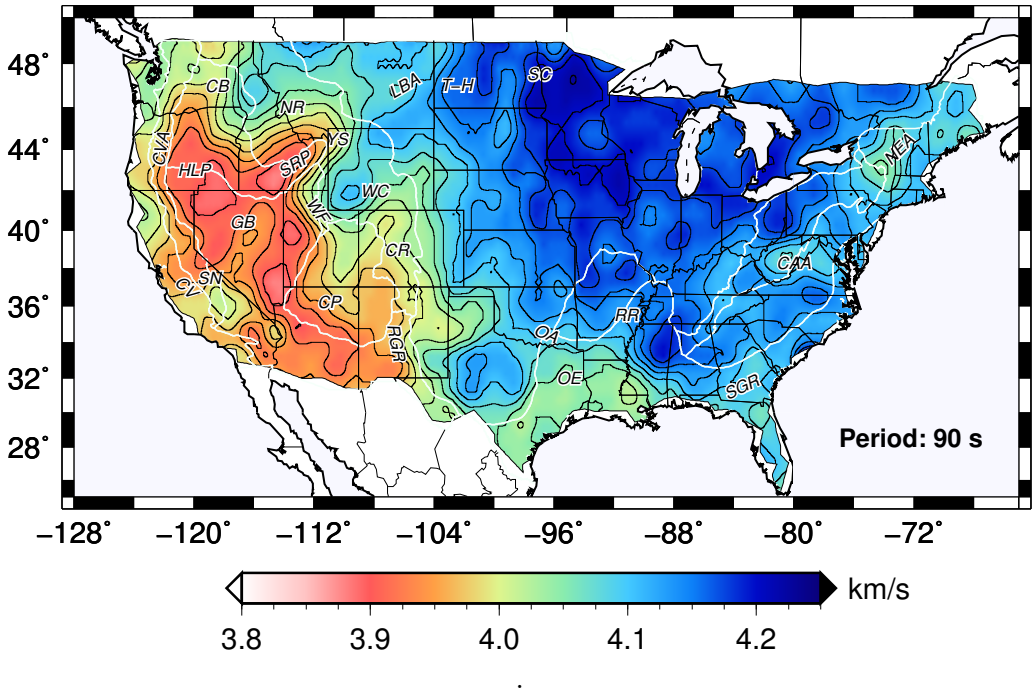

FIGURE 3.13: Isotropic phase velocity results for the 90 s Rayleigh wave.

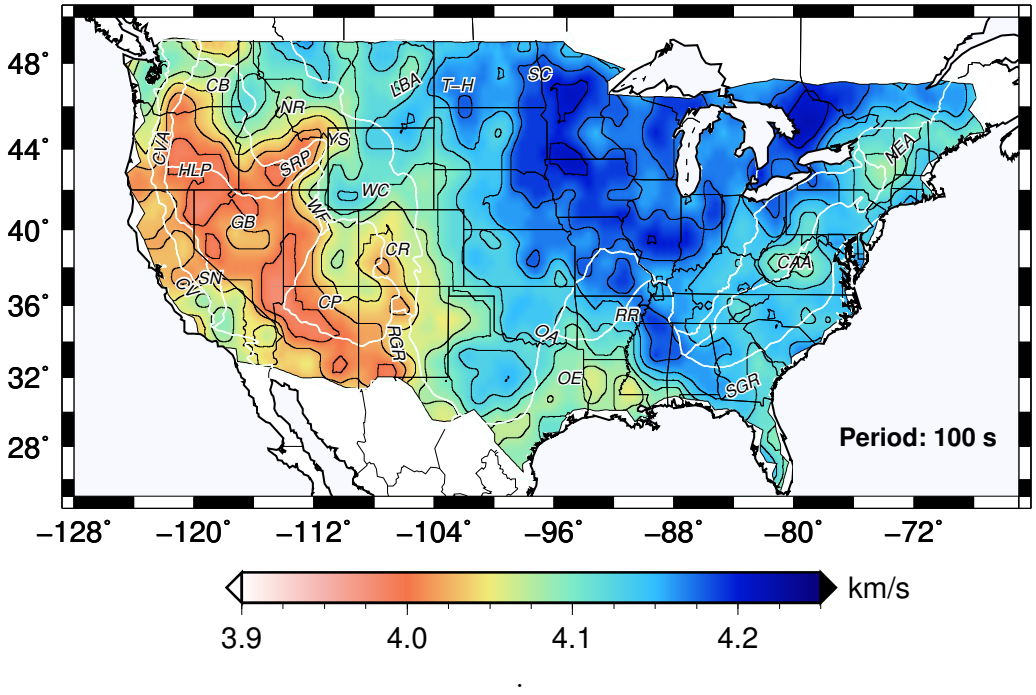

FIGURE 3.14: Isotropic phase velocity results for the 100 s Rayleigh wave.

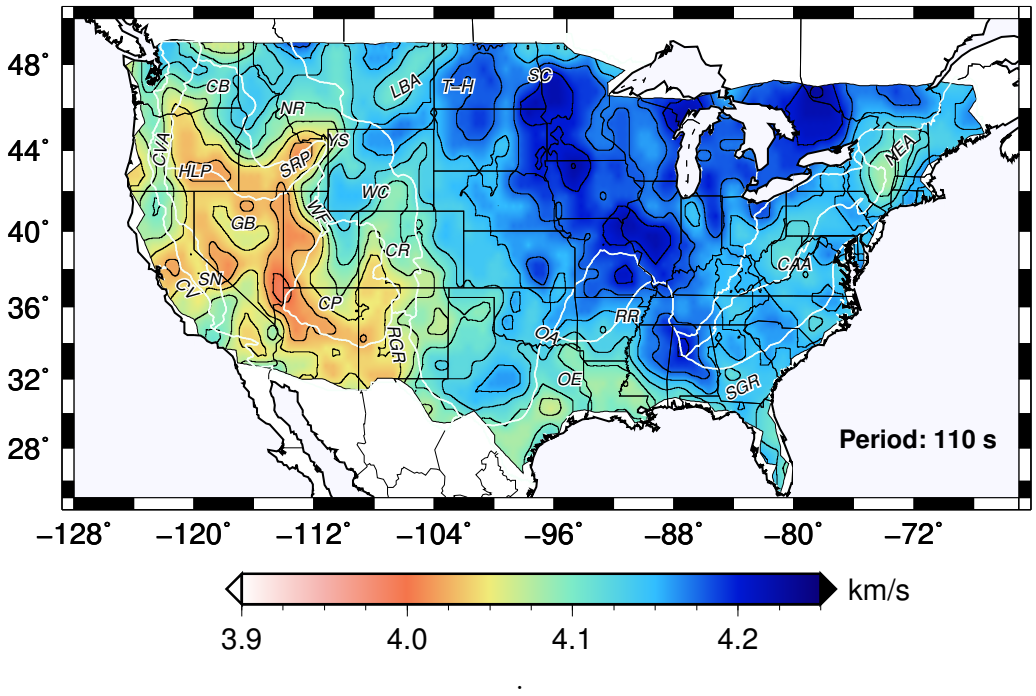

FIGURE 3.15: Isotropic phase velocity results for the 110 s Rayleigh wave.

values are resolved, at least in part, in the regions of the Isabella Anomaly [*Schmandt and Humphreys*, 2010; *Jones et al.*, 2014] and southern Sierra Nevada (SN). Within central and eastern Montana there is a lower velocity region that extends diagonally northeast, corresponding approximately to the Little Belt Arc (LBA), which is the suture zone between the Wyoming Craton (WC) and Medicine Hat block [*Whitmeyer and Karlstrom*, 2007]. This feature is observed in 40 s - 110 s periods. Although possibly not well resolved due to its thin spatial distribution, results at 90 s - 120 s show a roughly N-S trending lower velocity zone in east central North and South Dakota that approximately corresponds spatially with the suture zone between the Trans-Hudson (T-H) orogen and the Superior Craton (SC) [*Whitmeyer and Karlstrom*, 2007]. That is, for these longer periods the area corresponding to the western side of the Trans-Hudson orogen shows high structural

phase velocities.

The velocity transition along the approximate boundary between Great Plains and Central Lowland persists for periods of 80 s - 90 s, but this boundary is less distinct for periods up to 120 s. Within the Gulf of Mexico region phase velocities remain low for periods of 80 s - 110 s, with the longest periods showing the lowest relative values within the Ouachita Embayment (OE). A zone of higher phase velocities reaches southward into northern and central Mississippi and Alabama, north of the Gulf coastal plain. The highest velocities occur as far east as Lakes Erie and Ontario, which is east of the Grenville Front at 110 s (Figure 3.15). Also for the period range of 100 s - 110 s, a low velocity anomaly exists below eastern North Dakota and northern Minnesota and it's coincident with the Superior Upland [*Fenneman*, 1917]. The Central Appalachian Anomaly (CAA) and Northeast Anomaly (NAE) remain prominent for periods out to 110 s, which is consistent with body wave studies in the upper mantle from *Schmandt and Lin* [2014]. A low velocity anomaly starts to show up in the South Georgia Rift (SGR) for this period range, which may be part of Central Atlantic Magmatic Province (CAMP) that formed $\sim$ 200 Ma [*Heffner et al.*, 2012; *Pollitz and Mooney*, 2016].

3.3.4 Isotropic Velocities within 120 s - 150 s Period

For 120 s - 130 s periods (Figure 3.16, 3.17), many of the above described anomalies within the western U.S., like the low velocity regions in Snake River Plain (SRP), Yellowstone (YS), Great Basin (GB), Sierra Nevada (SN) and high velocities regions within the central and eastern U.S., are still apparent, but for periods 140 s - 150 s (Figure 3.18,

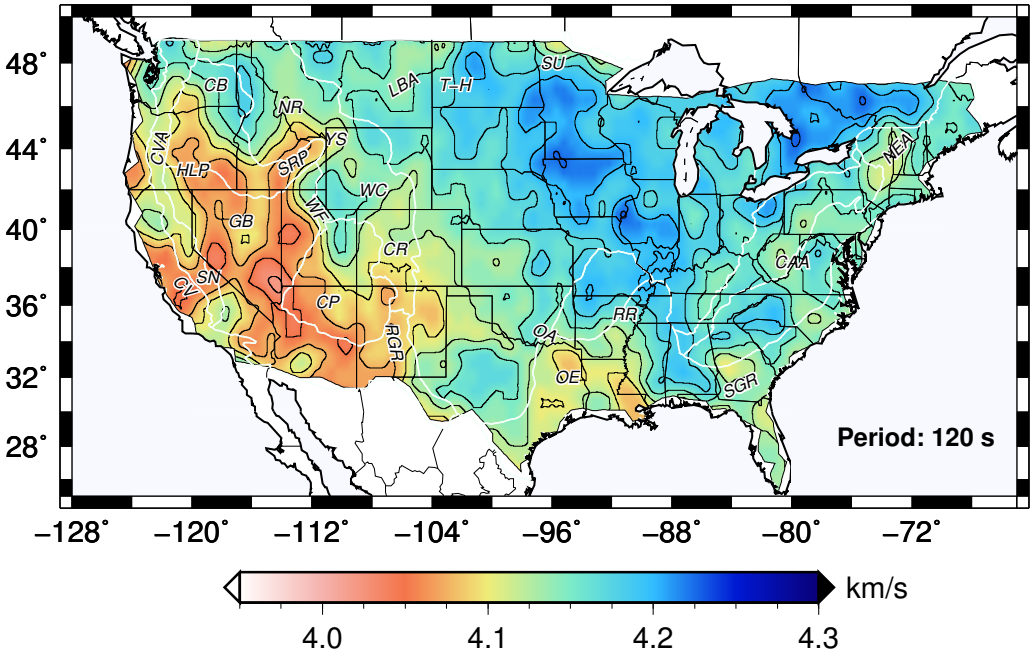

FIGURE 3.16: Isotropic phase velocity results for the 120 s Rayleigh wave. Geographic features as indicated: SU, Superior Upland.

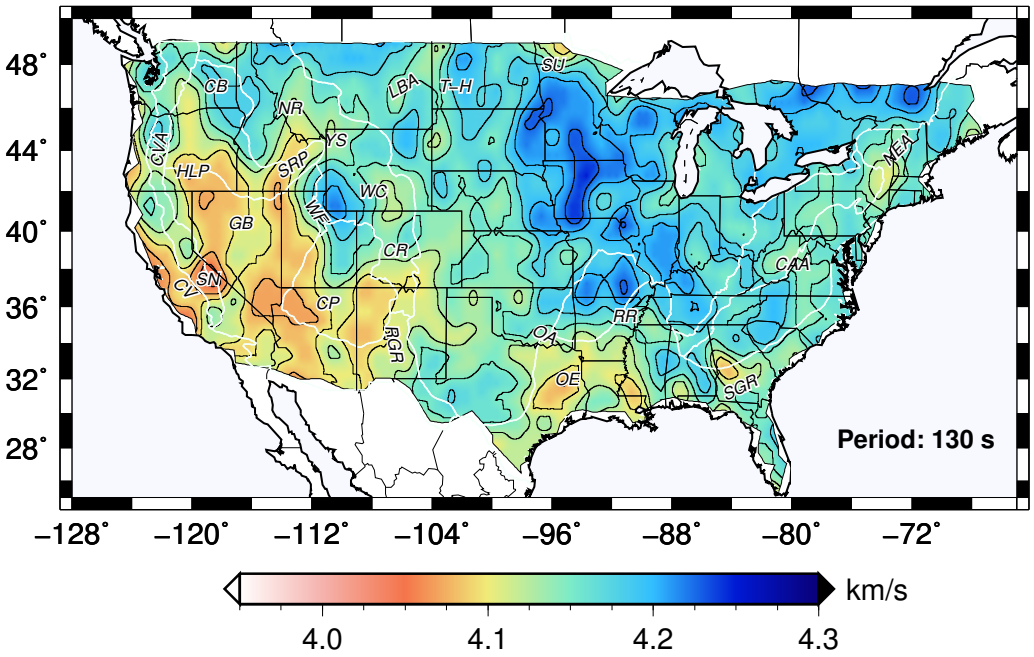

FIGURE 3.17: Isotropic phase velocity results for the 130 s Rayleigh wave.

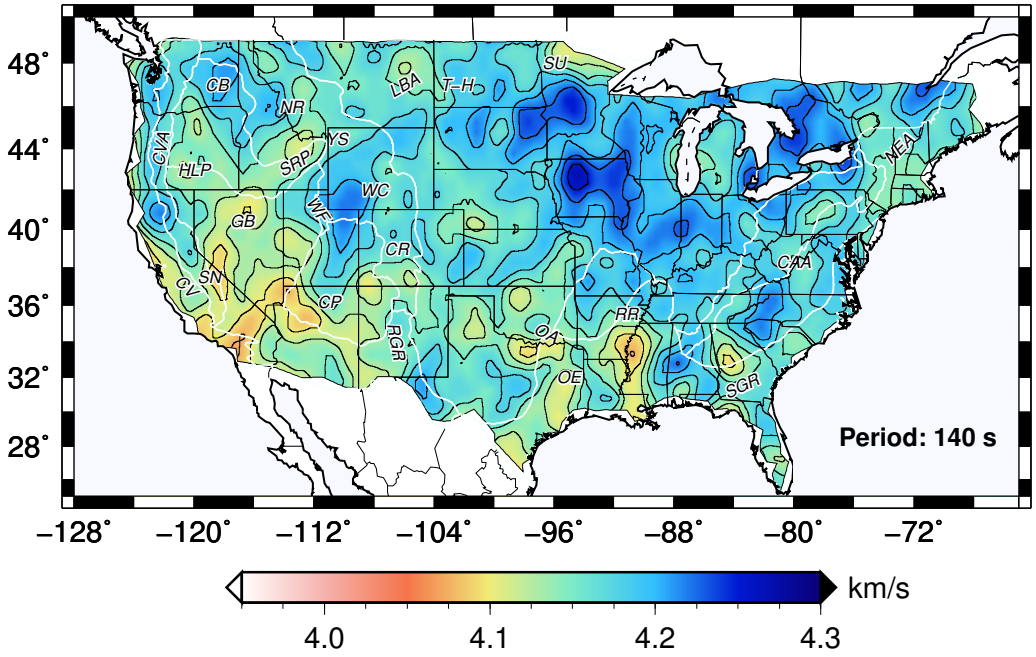

FIGURE 3.18: Isotropic phase velocity results for the 140 s Rayleigh wave.

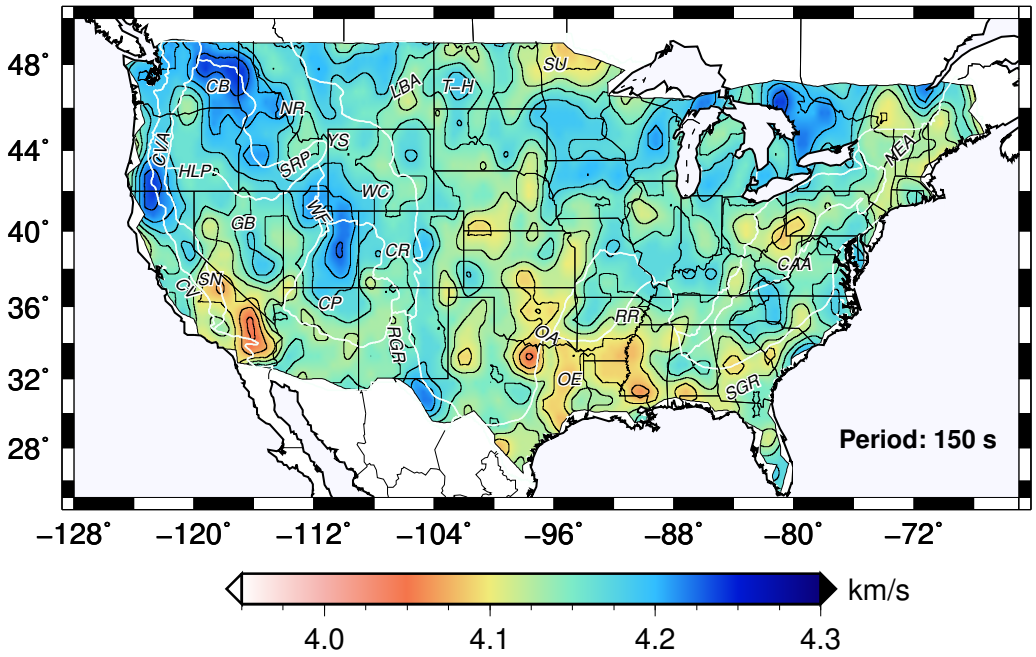

FIGURE 3.19: Isotropic phase velocity results for the 150 s Rayleigh wave.

3.19) the phase velocity differences between the western and eastern U.S. are less clear. High velocities within eastern Washington and western Idaho are consistent with a large high-velocity "Siletzia curtain" extending vertically beneath the Challis magmatic trend imaged by teleseismic tomography from *Schmandt and Humphreys* [2011], who attributed this seismically fast upper mantle to subducted ocean lithosphere. The Wyoming Craton (WC) and the central and northern Colorado Plateau (CP) stand out as significant high velocity anomalies, consistent with recent body wave tomography results for high velocity anomalies in these regions at 200 km depth [*Schmandt and Lin*, 2014]. The prominent low velocity regions in the Snake River Plain (SRP) and the Yellowstone (YS) regions have nearly vanished at 150 s, which is consistent with the 200 km bottom of these shear velocity anomalies determined in Rayleigh wave tomography studies [*Wagner et al.*, 2010]. Prominent fast regions for periods of 120 s - 150 s are observed in the Cascadia region (Juan de Fuca slab), the eastern Columbia Basin (CB), the southern Wyoming Craton (WC), the northernmost Colorado Plateau (CP), and the central core of the Craton region around the Great Lakes.

Phase velocities for the longest period of 150 s (Figure 3.19) show a low velocity region trending N-S beneath the Great Plains in the central U.S. from the southern Gulf state region into North Dakota and even northern Minnesota (Superior Upland (SU)). The low phase velocities beneath the Superior Upland are also present at 110 s (Figure 3.15). These lower phase velocities for the longest periods for both the Great Plains and the Superior Upland are somewhat enigmatic and to our knowledge have not be described to date. The low-velocity zone (LVZ) in the Reelfoot Rift (RR) is still pronounced up

to 150 s period. Both body wave tomography [*Zhang et al.*, 2009] and surface wave imaging [*Pollitz and Mooney*, 2014] suggest that the low velocity regions beneath RR extend to depths of 180 km, and possibly to 200 km [*Bedle and van der Lee*, 2006; *Pollitz and Mooney*, 2016]. Lower velocities are observed along the Oklahoma Aulocogen (OA), Ouachita Embayment (OE), and in southern Texas, Louisiana, and Mississippi. Whereas fast velocities are observed in the central Texas for the period range of 26 s - 120 s, for periods of 130 s - 150 s we observe slower velocities distributed further west into east-central Texas. These slower velocities in the eastern Texas nearly coincide with the low shear wave velocities at 180 km depth noted by *Pollitz and Mooney* [2016].

The Central Appalachian Anomaly (CAA) and Northeast Anomaly (NEA) persist to periods of 150 s. The low velocities beneath the South Georgia Rift (SGR) are more prominent for this period range, especially for 150 s period where a semi-continuous low velocity region starts from southern Alabama, passes through central and southern Georgia, South Carolina, and North Carolina. This low velocity anomaly connects with the Central Appalachian Anomaly (CAA), and is observed in Pennsylvania, New Jersey, New York and continues to the Northeast Anomaly (NEA).

3.4 Discussion

The 20 s - 150 s Rayleigh waves isotropic structural phase velocities can be used to constrain shear velocities in the crust and upper mantle across the contiguous U.S. [*Porter et al.*, 2016], especially when combined with other methods, such as receiver function analysis [*Shen et al.*, 2013a] and horizontal-to-vertical amplitude (H/V) ratio [*Tanimoto*

and Rivera, 2008; *Schmandt et al.*, 2015]. Furthermore, gradiometry parameters provide a rich field of information that can be used for present and future structural studies. *Liu and Holt* [2015, 2016a] have shown that gradiometry parameters and products provide remarkable features of the wavefield that link the focusing and defocusing of energy with significant amplitude variations. Gradiometry patterns, reflecting wavefield characteristics, are unique for each event. These archived results thus provide useful information about the structure along the ray path, which can serve as new constraints for viable structural interpretations in future 3-D modeling.

An interesting feature in the longest period results of 140 s - 150 s is the development of prominent low velocity zones covering several regions, including the Oklahoma Aulocogen (OA), Ouachita Embayment (OE), Realfoot Rift (RR), South Georgia Rift (SGR), as well as within the Great Plains and Superior Upland (SU). Furthermore, low velocity anomalies show a semi-continuous connection between the South Georgia Rift (SGR), the Central Appalachian Anomaly (CAA) and the Northeast Anomaly (NEA).

Low velocity anomalies beneath OA, OE, and RR have been discussed previously [*Zhang et al.*, 2009; *Pollitz and Mooney*, 2014], and our results are consistent with a deep lithosphere lower velocity signature there. The semi-continuous band of lower phase velocities between South Georgia Rift (SGR) and the Northeast Anomaly (NEA) may be a signature in the lower lithosphere left by the Central Atlantic Magmatic Province (CAMP) [*Heffner et al.*, 2012; *Pollitz and Mooney*, 2016]. *Chu et al.* [2013] attributed low velocity anomalies observed between Virginia and the mid-continent to hotspot interaction with the thermal-chemical lithosphere. *Pollitz and Mooney* [2016] argued that

the hotspot interaction within regions of lithosphere containing significant volumes of igneous intrusions associated with CAMP may also contribute to low velocity anomalies within the lower lithosphere, such as beneath the South Georgia Rift (SGR). The two hotspot tracks [*Chu et al.*, 2013] show paths that are roughly consistent with patterns of low velocity anomalies in our results for 140 s - 150 s. For example, the northern hotspot track ($\sim$ 100 Ma) described by *Chu et al.* [2013] passes from the NEA into Pennsylvania and CAA, and then through Kentucky, Missouri and Nebraska. We observe lower phase velocities in central Kentucky and northern Tennessee. We do not observe low velocities in eastern Missouri, but significant low velocity anomalies are present in western Missouri, eastern Kansas and Nebraska in the 140 s - 150 s period range. The continuous band of lower phase velocities in north and south Carolina, Georgia, the southern Gulf states, and east Texas are likewise consistent with the Bermuda hotspot track [*Chu et al.*, 2013]. However, the connectivity of the anomalies with the two hotspot tracks is only apparent for the longest period results of 140 s - 150 s, suggesting these anomalies are associated primarily with the lower lithosphere. Indeed, recent body wave tomography results [*Schmandt and Lin*, 2014] show similar patterns of low velocity anomalies at 200 km depth, consistent with these patterns described above. Although low velocities in NEA and CAA are potentially part of the northern hotspot track, they nevertheless are distinct in that they are present for all periods between 40 s - 150 s, suggesting they are associated with the entire lithosphere mantle [*Porter et al.*, 2016]. The Central Appalachian Anomaly (CAA) could be particularly strong because it may be associated with lithosphere delamination [*Mazza et al.*, 2014; *Schmandt and Lin*, 2014; *Porter et al.*,

2016].

Results for 140 s - 150 s periods do not uniquely define the depths of the source anomalies, and it remains unclear if velocity anomaly signals described above can be attributed solely to a lithosphere signature. The lithosphere-asthenosphere boundary (LAB) has been estimated using surface and body wave tomography [*Yuan and Romanowicz*, 2010; *Rychert et al.*, 2005] and receiver function studies [*Fischer et al.*, 2010; *Kumar et al.*, 2012]. If the lithosphere thickness of about 200 km obtained by *Yuan and Romanowicz* [2010] applies, then many of the anomalies described above for the longest periods could be signatures retained within the lithosphere. On the other hand, receiver function studies [*Fischer et al.*, 2010; *Kumar et al.*, 2012] have defined LAB boundaries along the easternmost U.S. that are around 100 km, suggesting that some of the anomaly features we have discussed (140 s - 150 s) may be a product of the asthenosphere. In this latter case, linking slow velocity anomalies for the longest periods to ancient heat sources within the asthenosphere [*Chu et al.*, 2013] may be problematic, owing to active mantle flow patterns and plate motions [*Forte*, 2007; *Forte et al.*, 2007; *Moucha et al.*, 2008; *Ghosh et al.*, 2013; *Wang et al.*, 2015]. Instead, the deep anomalies would reflect the present-day asthenosphere, and any correlation of these low velocity anomalies within the longest periods with past igneous activity within the lithosphere could be coincidence. As mentioned above, the CAA and NEA appear different in that they are present for a wide range of periods between 40 s - 150 s, suggesting that these anomalies are present at lithosphere depths [*Porter et al.*, 2016].

The slower phase velocities beneath the Great Plains and Superior Upland (SU) within

120 s - 150 s period remain enigmatic. These regions are too large to be solely explained by the hotspot tracks in *Chu et al.* [2013]. Instead the entire Great Plains and Superior Upland regions appear to be underlain by slow structural phase velocities at 120 s - 150 s. This could reflect asthenosphere signature, or possibly the influence of hydration mechanisms from the Farallon slab [*Humphreys et al.*, 2003; *Jones et al.*, 2015]. *Jones et al.* [2015] recently argued that uplift of the Great Plains was related to the introduction of water into the crust. Our observation of lower structural phase velocities out to the easternmost Great Plains may suggest alteration of lower lithosphere through introduction of fluids derived from the Farallon slab [*Humphreys et al.*, 2003]. The higher elevations of the Superior Upland (SU) may also be linked to similar processes as that proposed for the uplift of the Great Plains [*Jones et al.*, 2015]. If the lower phase velocities beneath the Great Plains and Superior Uplands reflect asthenosphere signal then the velocity anomalies may reflect temperature effects with the associated dynamic topography. Uplift of the Great Plains has occurred since the middle Miocene [*Heller et al.*, 2003] with uplift occurring up to the present-day being attributed to the dynamic topography [*Duller et al.*, 2012]. Alternatively, the changes observed at the longest periods may reflect the influence of anisotropy layering within the lithosphere described by *Yuan and Romanowicz* [2010].

3.5 Conclusions

We combined the wave gradiometry and Helmholtz equation solution [*Liu and Holt*, 2015] to process 696 earthquakes from 2006 to 2014 and calculated wave gradiometry parameters at 1,739 USArray TA Stations. The Rayleigh wave isotropic structural phase

velocities are obtained for 20 s - 150 s periods, along with variances and standard deviations. The phase velocities generally increase with period from 3.3 ± 0.1 km/s to 4.5 ± 0.2 km/s in the western U.S., from 3.6 ± 0.1 km/s to 4.5 ± 0.2 km/s in the central and eastern U.S., which are consistent with the theoretical dispersion curves [*Dahlen and Tromp*, 1998]. For periods longer than 50 s, the amplitude correction terms increase with period, and the standard deviations of dynamic phase velocity (0.2 - 0.25 km/s) are also larger than that of structural phase velocity (0.1 - 0.2 km/s). Thus we argue that surface wave tomography can be improved by using amplitude measurements to construct a geographically localized correction via the Helmholtz equation solution, at least for periods longer than 50 s in the case of USArray TA configuration [*Lin and Ritzwoller*, 2011a; *Jin and Gaherty*, 2015; *Liu and Holt*, 2015]. We have shown that the isotropic phase velocities obtained using wave gradiometry are interpreted to be similar to recent body wave and surface wave tomography and other inversion methods [*Lin et al.*, 2008; *Schmandt and Humphreys*, 2010, 2011; *Pollitz and Snoke*, 2010; *Shen et al.*, 2013a; *Pollitz and Mooney*, 2014; *Jin and Gaherty*, 2015; *Pollitz and Mooney*, 2016]. Furthermore, we have identified several regions with potentially new constraints, such as provided by anomaly patterns for the longest periods of 120 s - 150 s and the anomaly strength for the CAA and NEA defined for periods of 40 s - 150 s. The gradiometry parameters: $\vec{A}$, $\vec{B}$, ∇A, ∇B for all events are archived as additional constraints for future 3-D modeling.

Chapter 4

Inversion for Shear Velocity Models across the Continental U.S.

4.1 Introduction

The construction of crustal and upper mantle shear velocity models is crucial in developing an understanding of continental tectonics and the thermal and compositional structure of the lithosphere as well as to provide the structural framework for an assessment of natural hazards. The surface wave sensitively kernel has been employed by seismologists to provide constraints on the shear velocity structure within the crust and upper mantle [*Bedle and van der Lee*, 2009; *Bensen et al.*, 2009; *Yang et al.*, 2011]. The deployment of the EarthScope USArray TA network allows for the mapping of the Earths structure within the North America continent in unprecedented detail. Using the 8 s - 150 s Rayleigh waves recorded by USArray TA stations, we present three-dimensional models of the shear wave velocity structure within crust and upper mantle by inverting Rayleigh wave isotropic phase velocity results determined from ambient noise tomography [*Bensen et al.*, 2007] and wave gradiometry [*Liu and Holt*, 2015]. The shear velocity models have

already been published in *Porter et al.* [2016], which coincide well with previous calculated Rayleigh wave structural phase velocities [*Ekström*, 2014; *Jin and Gaherty*, 2015; *Liu and Holt*, 2016b,a] and body wave tomography results [*Schmandt and Humphreys*, 2010; *Burdick et al.*, 2014; *Schmandt and Lin*, 2014] across the contiguous U.S. These continent-wide models enable us to assess the effects of orogenic events on the modern crustal and upper mantle structure of North America. In this study we highlight some structural interpretations obtained by *Porter et al.* [2016], furthermore we provide further discussion on some new discoveries in the crust and upper mantle that were constrained primarily by gradiometry methods.

4.2 Data Sets and Methodology

The seismic data used in this study were collected from EarthScope USArray TA stations deployed from 2004 to 2015. Other publicly available data in southern California were used to improve the resolution of ambient noise tomography. Rayleigh wave phase velocity results at short periods (8 s - 40 s) and long periods (20 s - 150 s) were estimated using ambient noise tomography [*Bensen et al.*, 2007] and wave gradiometry [*Langston*, 2007a,b,c; *Liang and Langston*, 2009; *Liu and Holt*, 2015], respectively. Where overlapping data is present between 20 s - 40 s, the results from two methods are averaged [*Porter et al.*, 2016]. We then invert these combined phase velocity dispersion curves with a linearized least squares inversion method and a constant weight for each input phase velocity [*Herrmann and Ammon*, 2002]. However, the shear wave inversion is highly sensitive to sharp velocity contrasts in the starting model (e.g., Moho depth). In

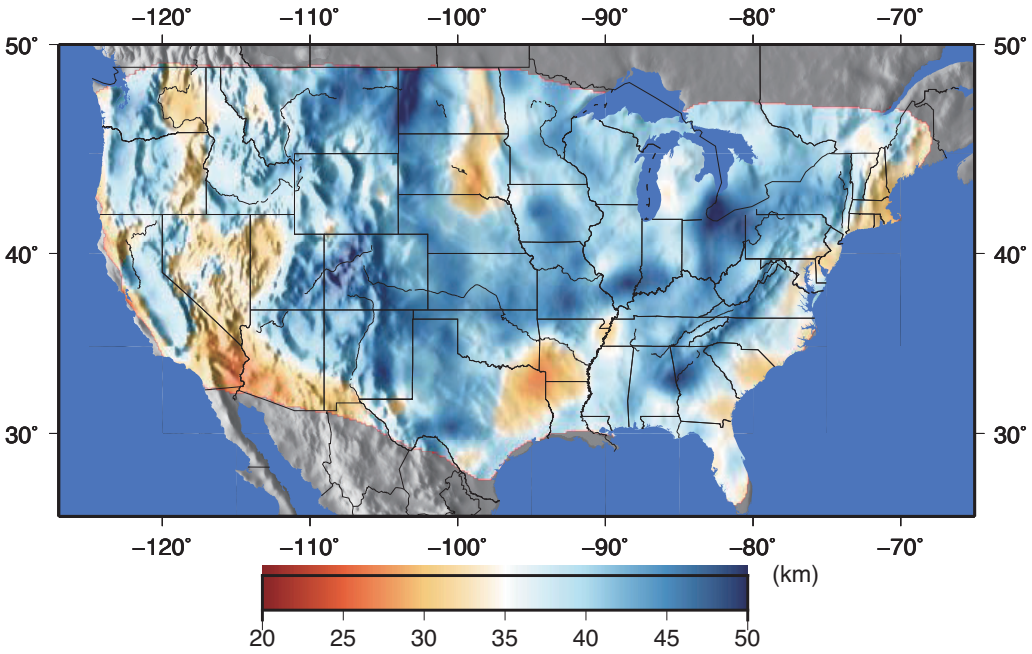

FIGURE 4.1: Map view of the EARS-derived crustal thickness model used in the inversions by *Porter et al.* [2016].

order to produce a consistent model across the U.S., continent-scale models of crustal and sediment thickness are embedded in the starting model [*Porter et al.*, 2016]. The crustal thickness estimates from the EarthScope Automated Receiver function Survey (EARS) [*Crotwell and Owens*, 2005] are shown in Figure 4.1. The sediment thickness estimates were taken from the model presented in *Laske et al.* [1997] (Figure 4.2). The detailed methodology, computation parameters and other techniques used in this study is described in *Porter et al.* [2016] in detail.

4.3 Analysis of Shear Velocity Results

Our shear velocity results highlight many of the same broad patterns as observed by *van der Lee and Frederiksen* [2005]; *Bensen et al.* [2007], with low velocities observed at

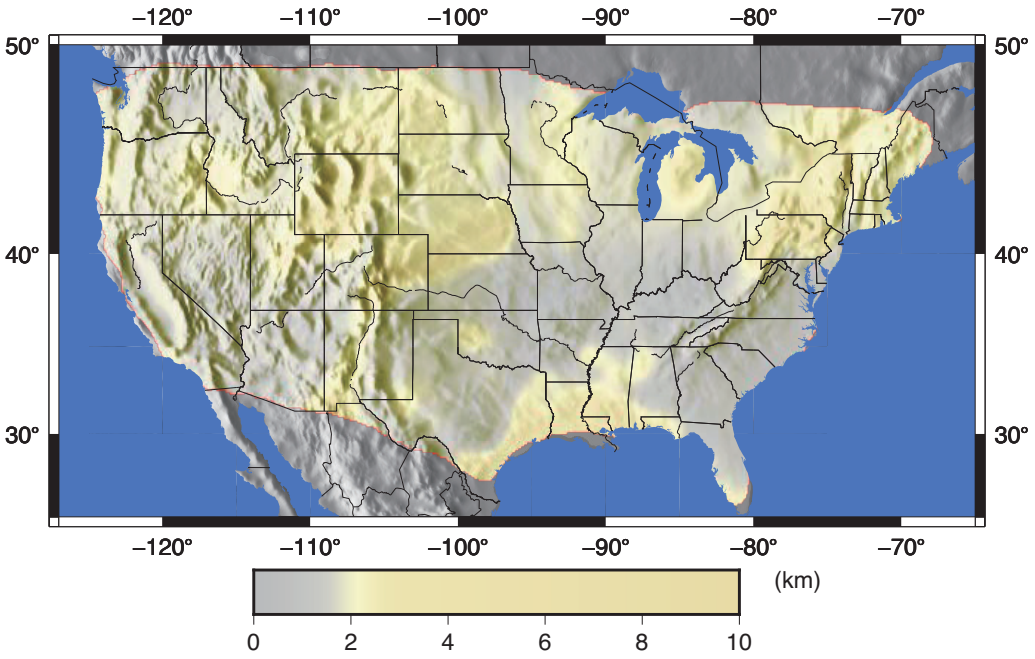

FIGURE 4.2: Map view of the sediment thickness model used in the inversions by *Porter et al.* [2016].

all depths in the western U.S. and faster velocities in the central and eastern U.S. Our observations within the western U.S. are similar to several continent-scale surveys that utilize surface wave measurements [*Pollitz and Snoke*, 2010; *Moschetti et al.*, 2010a,b; *Liu and Holt*, 2015] or combine receiver functions and surface waves [*Shen et al.*, 2013a,b; *Schmandt and Humphreys*, 2010] as well as numerous regional-scale studies. In the central and eastern U.S. there are marked similarities to surface wave results in New England [*Li et al.*, 2003], the south central U.S. [*Pollitz and Mooney*, 2014], and to body wave tomography results across the contiguous U.S. [*Schmandt and Humphreys*, 2010; *Burdick et al.*, 2014; *Schmandt and Lin*, 2014; *Pollitz and Mooney*, 2016]. However, some previous shear models predate the dense station spacing of the USArray Transportable Array, and do not provide the ability to image finer-scale features that we observe in this study.

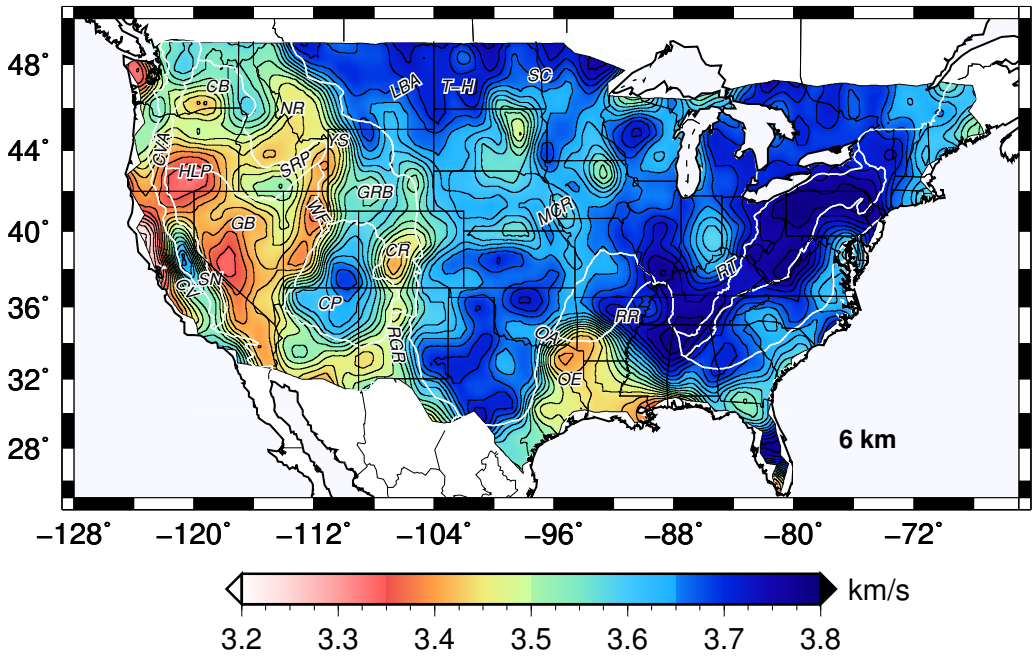

FIGURE 4.3: Map showing shear velocities at the depth of 6 km. Contours are separated by intervals of 0.05 km/s, including all the maps below. White lines show approximate geographic province boundaries, which are indicated as: CB, Columbia Basin; CP, Colorado Plateau; CR, Colorado Rockies; CVA, Cascade Volcanic Arc; CV, Central Valley; GB, Great Basin; GRB, Green River Basin; HLP, High Lava Plains; LBA, Little Belt Arc; MCR, Mid Continent Rift; NR, North Rocky Mountain; OA, Oklahoma Aulocogen; OE, Ouachita Embayment; RGR, Rio Grande Rift; RR, Reelfoot Rift; RT, Rome Trough; SN, Sierra Nevada; SRP, Snake River Plain; SC, Superior Craton; T-H, Trans-Hudson; WF, Wasatch Front; YS, Yellowstone.

Based on surface wave sensitivity kernels [*Snoke and James*, 1997], we are able to interpret the crustal and upper mantle structures by combining previous calculated Rayleigh wave isotropic velocities in Chapter 3 with these new shear velocity models.

4.3.1 Shear Velocities within the 6 km - (Moho - 4) km Depth

The shear velocity models within the crust across the continental U.S. are shown in Figure 4.3, 4.4, 4.5, 4.6, 4.7, 4.8 and 4.9. In the western U.S., shear velocities correlate well with deformation and volcanism. Low velocities (3.3 - 3.5 km/s) are observed in the

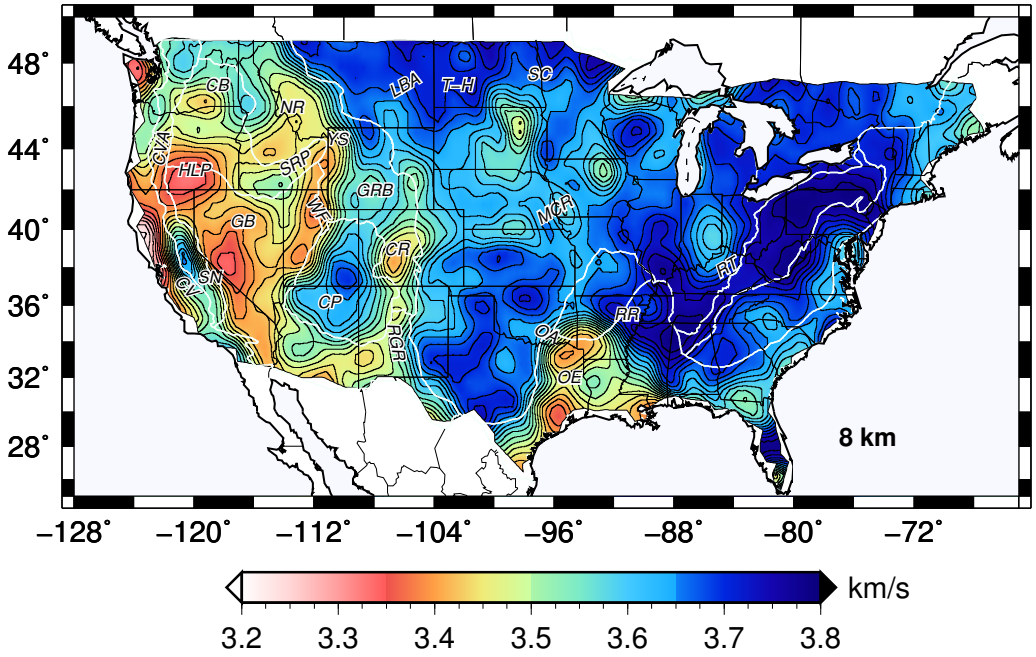

FIGURE 4.4: Map showing shear velocities at the depth of 8 km.

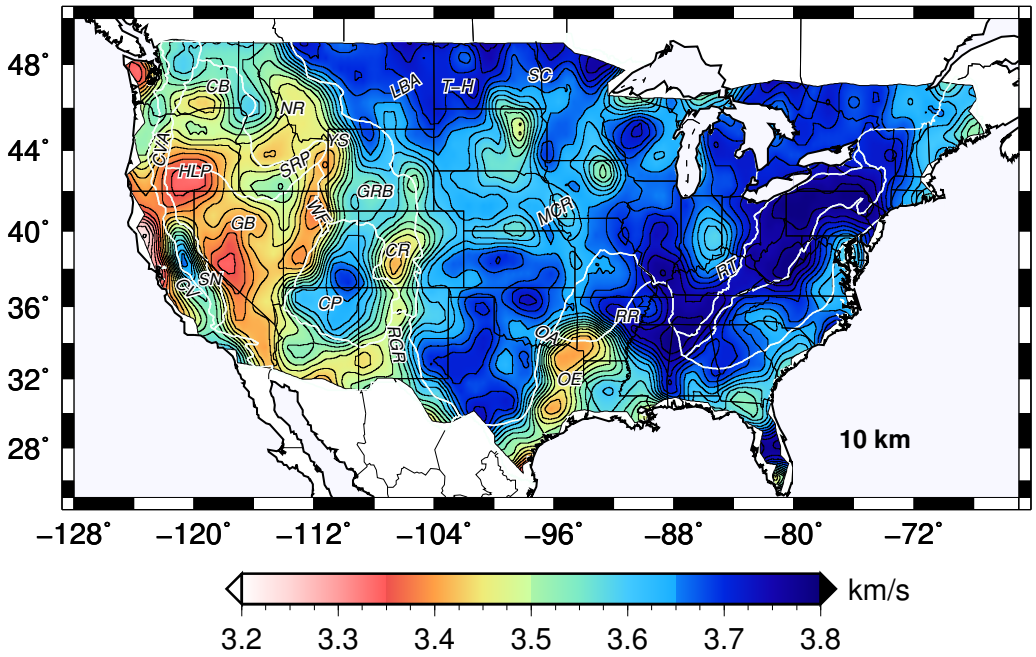

FIGURE 4.5: Map showing shear velocities at the depth of 10 km.

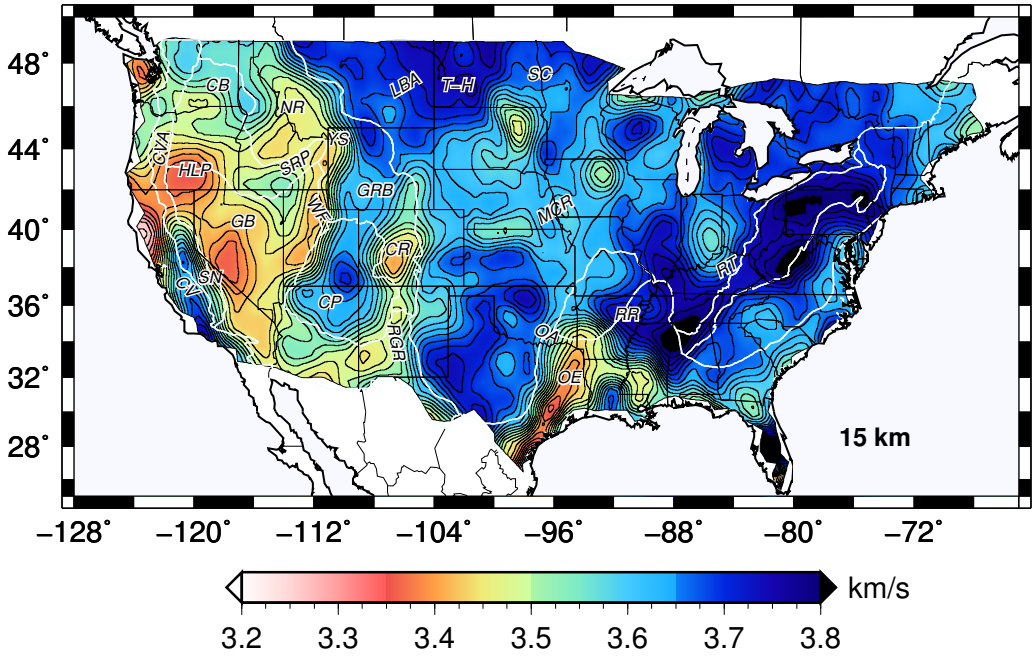

FIGURE 4.6: Map showing shear velocities at the depth of 15 km.

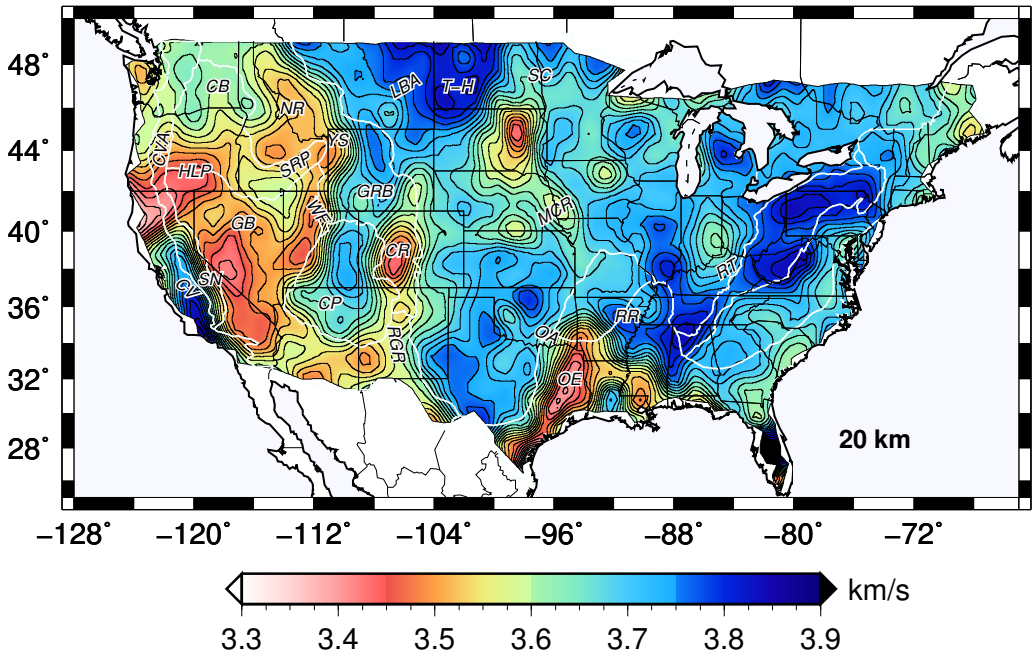

FIGURE 4.7: Maps showing shear velocities at the depth of 20 km.

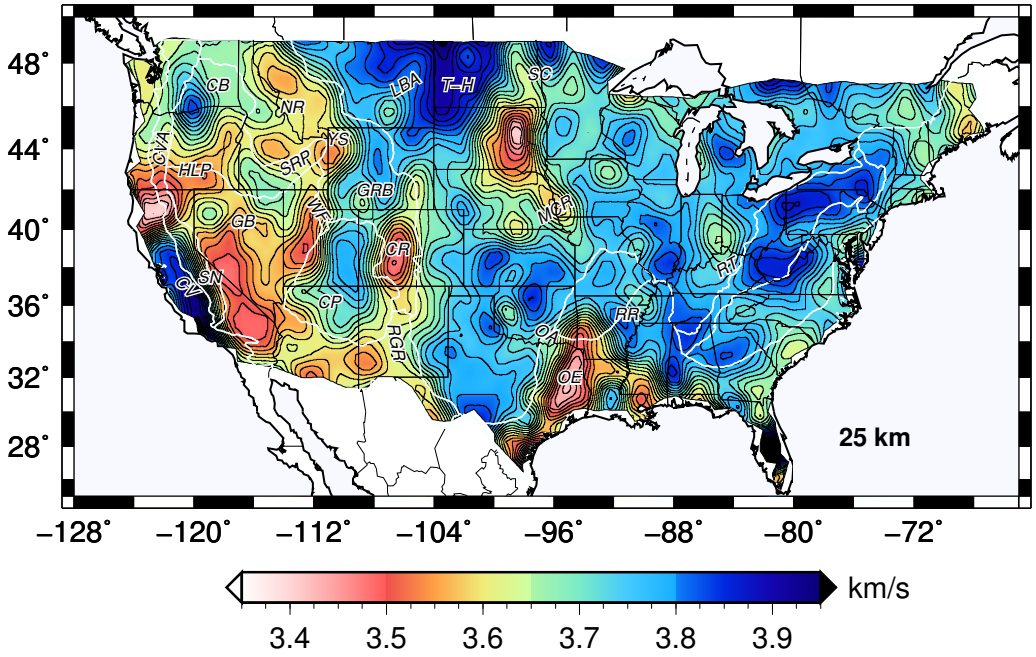

FIGURE 4.8: Map showing shear velocities at the depth of 25 km.

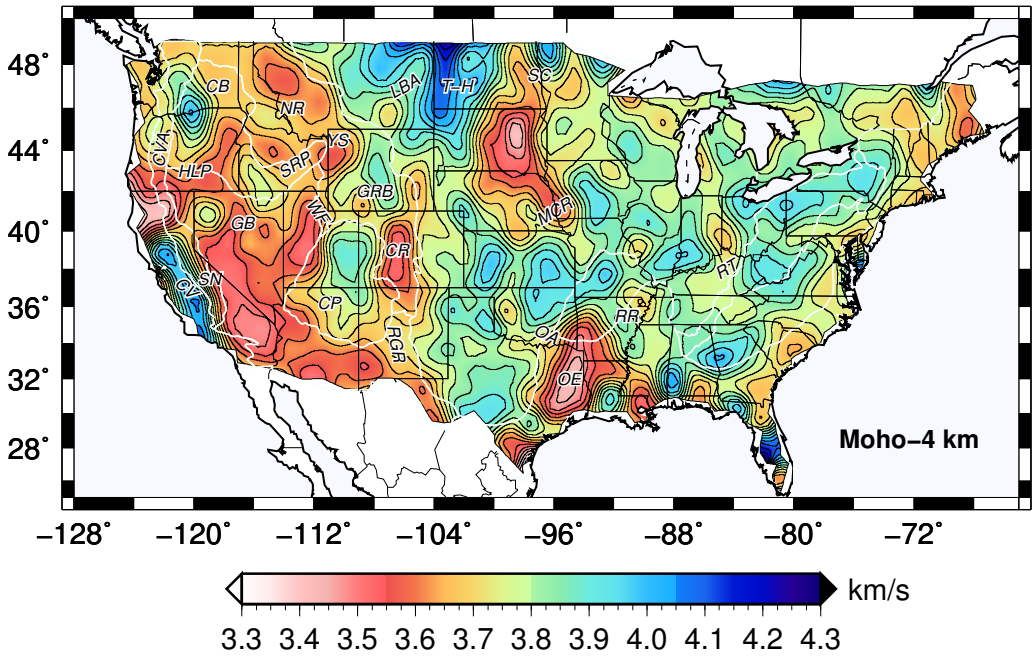

FIGURE 4.9: Map showing shear velocities at 4 km above Moho.

Columbia Basin (CB), the High Lava Plain (HLP), the North Rocky Mountain (NR), the Snake Rive Plain (SRP) and Yellowstone (YS), the Wasatch Front (WF), the Colorado Rockies (CR), the Rio Grande Rift (RGR), and the western Great Basin (GB) in western Nevada/California border region (close to Long Valley Caldera center). Noted strong velocity contrasts exist between the Colorado Plateau (CP) and Great Basin, between the Northern Rocky Mountains and the plains in western Montana, and along the edge of the Ouachita Embayment (OE). Low velocities are ubiquitous throughout the western U.S., with the exception of the Sierra Nevada (SN) and Colorado Plateau (CP), and more minor high velocity zones in the central Snake River Plain (SRP), and northern and eastern Columbia Basin (CB). *Porter et al.* [2016] argued that the high velocity contrast between Colorado Plateau (CP) middle and the surrounding regions correlate well with heat flow distributions [*Blackwell et al.*, 2011], reflecting the regions that have experienced significant extension and volcanism.

In the central and southern U.S., low velocities are commonly found in Ancestral Rocky Mountains (ARM) basins and high velocities in ARM uplifts [*Porter et al.*, 2016]. Within the Ouachita Embayment (OE) low velocities (3.3 - 3.5 km/s) are observed throughout the crust, possibly indicative of modification during the several episodes of deformation that the region has experienced, including Iapetan rifting [*Thomas and Astini*, 1996; *Thomas*, 2011], deformation related to the Ouachita Marathon Orogeny, rifting during breakup of Pangea, and/or passive margin sedimentation, though these results may be impacted by the thick sedimentary layer in the region [*Porter et al.*, 2016].

There is a strong correlation between the low velocities and sedimentation in Gulf

Coast (Figure 4.2), but the low velocity zone in eastern South Dakota remains enigmatic, which might come from the crustal thickness model used to constrain the starting model. We observe a low crustal thickness region extending from North Dakota to South Dakota (Figure 4.1), whereas this anomaly stops at northern South Dakota in a crustal thickness model derived from receiver function studies [*Schmandt et al.*, 2015]. This crustal thickness anomaly coincides quite well with the shear velocity anomaly in eastern South Dakota which extends to as deep as 200 km. Since the shear velocity inversion is highly sensitive to sharp velocity contrasts near the Moho in the starting model [*Porter et al.*, 2016], a crustal thickness model with high resolution and accuracy may be used to better constrain the starting shear model in the future. The Mid-Continent Rift (MCR) is not as continuous as a low velocity zone in these inversion results for shallow crust as they are in the phase velocity maps discussed in chapter 3, possibly also due to the input crustal thicklimit of Laramide deformationness model. But prominent low velocities are nevertheless observed for regions of northernmost Wisconsin, Iowa, and southern Nebraska. Phase velocities below the Reelfoot Rift (RR) are relatively fast, which agrees with inferences of a "rift pillow" within the underlying crust there [*Stuart et al.*, 1997; *Pollitz and Mooney*, 2014; *Schmandt et al.*, 2015].

In the eastern U.S., the most prominent high-velocity features (3.8 - 4.0 km/s) occur within the crust beneath the Appalachian Mountains [*Porter et al.*, 2016]. Low velocities are present in Maine, along sections of the east coast, and in southern Georgia (South Georgia Basin). There is a well developed anomaly in Indiana that has no known source.

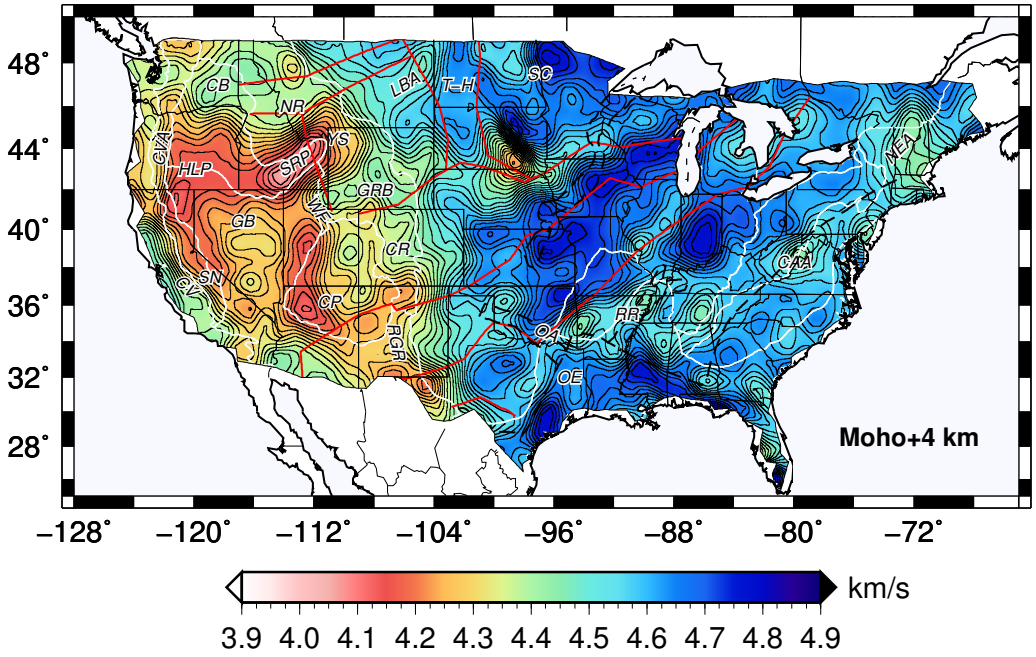

FIGURE 4.10: Maps showing shear velocities at 4 km below Moho. Geographic features are indicated as: CAA, Central Appalachian Anomaly; NEA, Northeast Anomaly. Red lines show approximate tectonic province boundaries following *Whitmeyer and Karlstrom* [2007] and black dashed lines show rift and collisional boundaries following *Schmandt et al.* [2015].

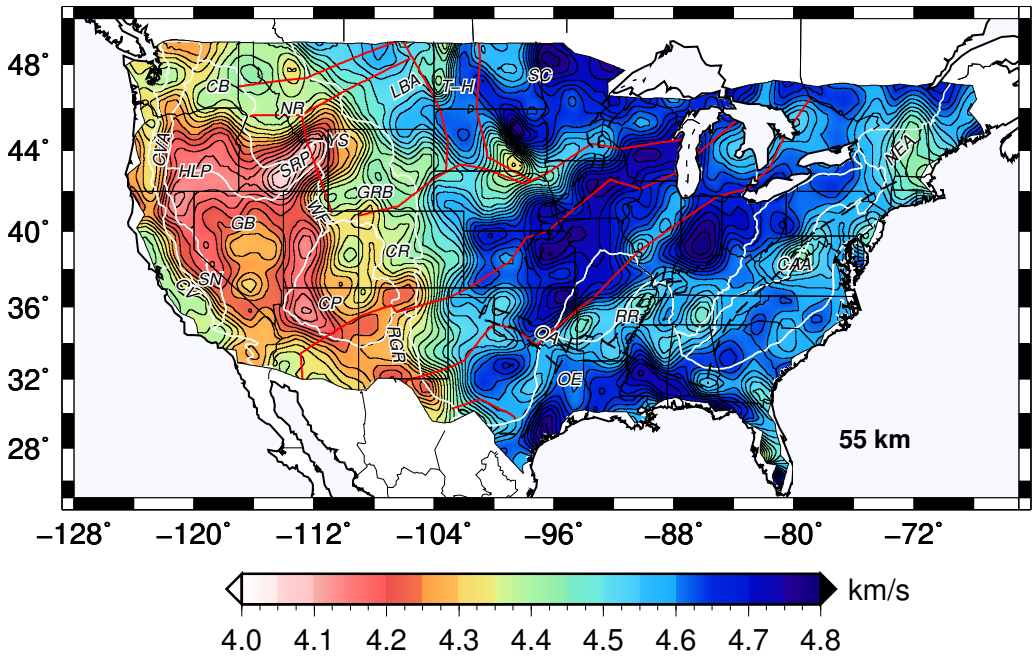

FIGURE 4.11: Map showing shear velocities at the depth of 55 km.

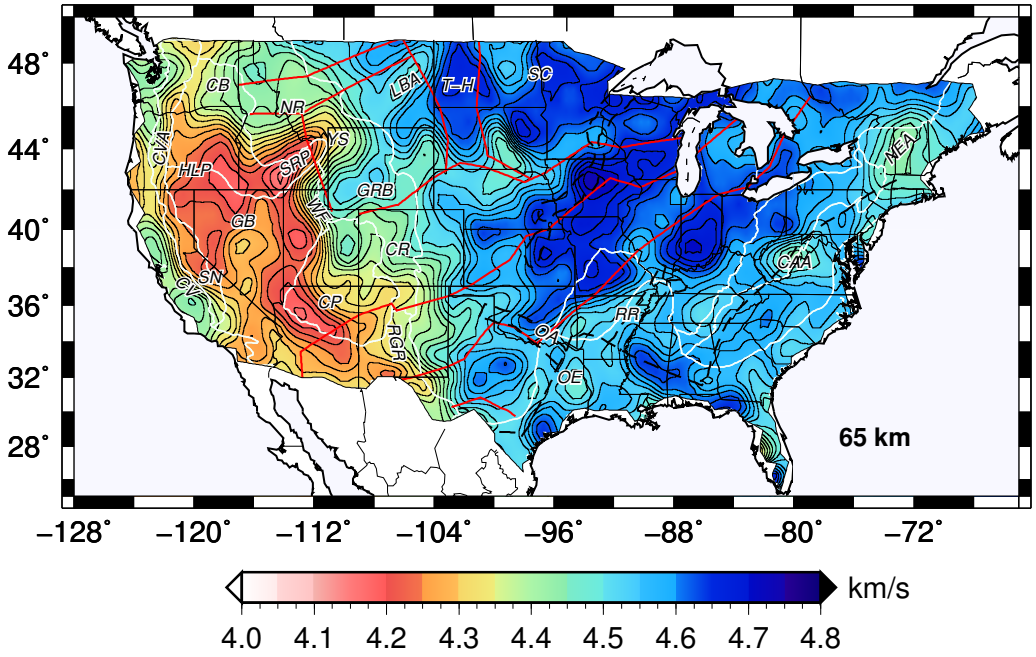

FIGURE 4.12: Map showing shear velocities at the depth of 65 km.

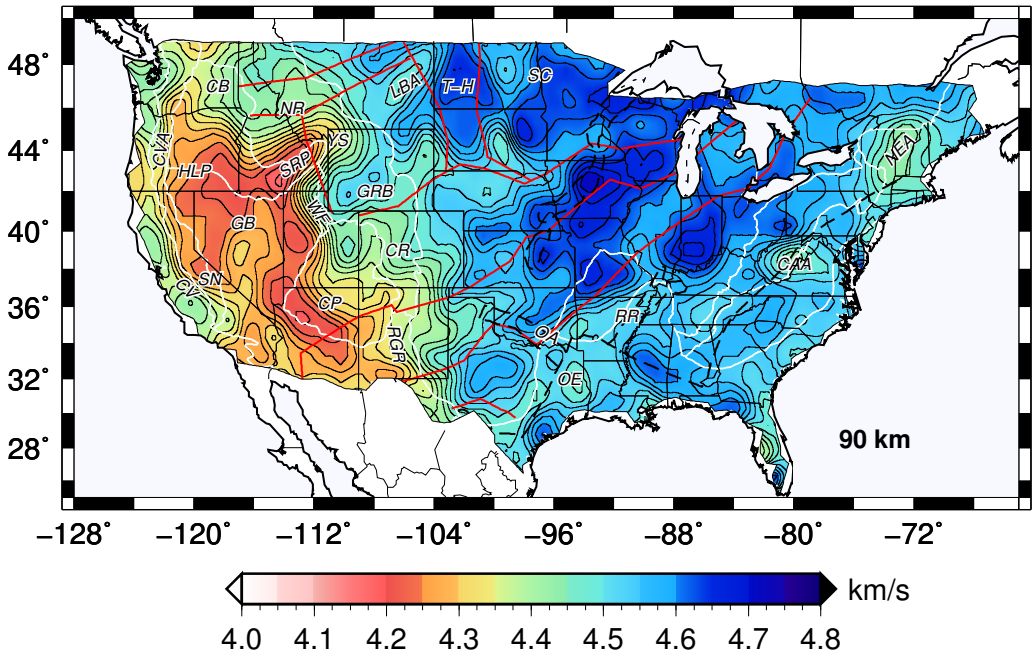

FIGURE 4.13: Map showing shear velocities at the depth of 90 km.

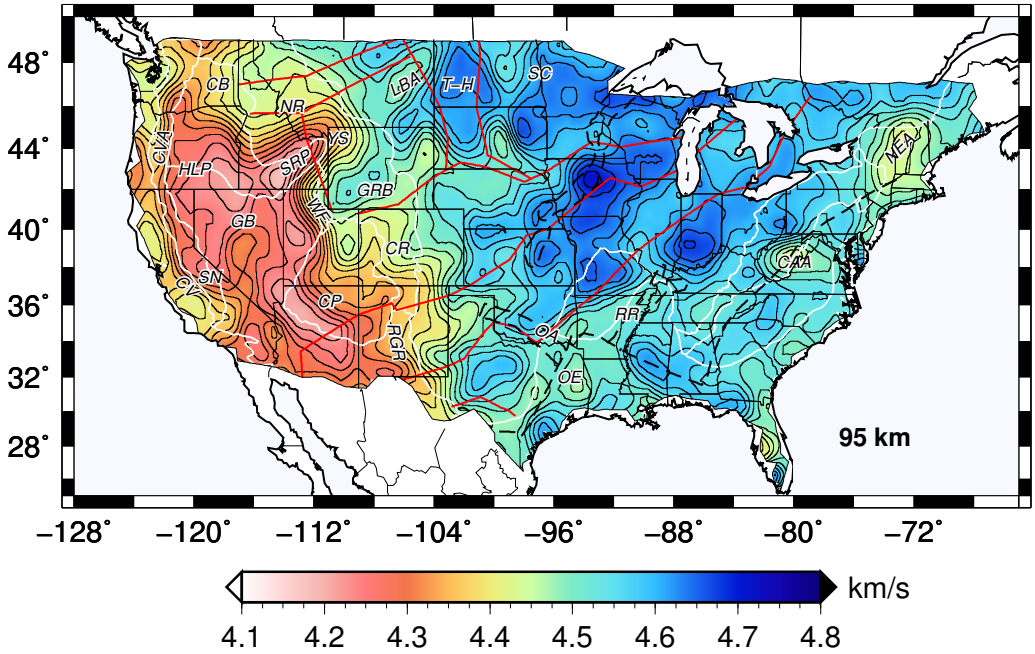

FIGURE 4.14: Map showing shear velocities at the depth of 95 km.

4.3.2 Shear Velocities within (Moho + 4) km - 95 km Depth

For the depth range of (Moho + 4) km - 95 km (Figure 4.10, 4.11, 4.12, 4.13, 4.14), the most prominent feature is the velocity contrast between the western U.S. and the central/eastern U.S. (CEUS), which closely aligns with the limits of Cordilleran deformation [*DeCelles*, 2004]. In the western U.S., the low velocities (4.1 - 4.3 km/s) are observed in the Snake Rive Plain (SRP) and Yellowstone (YS), the High Lave Plain (HLP), the Great Basin (GB), the south and central of Colorado Plain (CP), and the Rio Grande Rift (RGR). The higher phase velocities (4.4 - 4.5 km/s) within Central Valley (CV), beneath and adjacent to the west of southern Sierra Nevada (SN) coincide well with Isabella anomaly [*Schmandt and Humphreys*, 2010; *Jones et al.*, 2014]. A tongue of high velocities extends from the Wyoming Craton (WC) into the northern Colorado Plateau (CP). There is a low velocity region beneath the Black Hills in the western South Dakota

previous noted by *Shen et al.* [2013a]. *Porter et al.* [2016] suggests that the uplift of the range was controlled by a preexisting mantle weakness that may have led to the young volcanism in the region [*Kirchner*, 1977]. Within central and eastern Montana there is a lower velocity region that extends diagonally northeast, adjacent to the Little Belt Arc (LBA), which is the suture zone between the Wyoming Craton (WC) and Medicine Hat block [*Whitmeyer and Karlstrom*, 2007].

Shear velocity results in the mid continent within this depth range differ somewhat in pattern from the velocity trends that we saw in the phase velocities between 40 s - 70 s in Chapter 3. Whereas the Rayleigh wave phase velocities in this period range showed a transition to higher values along a roughly N-S trend through the central portions of North and South Dakota, Nebraska, Kansas, Oklahoma, and through central Texas, patterns from the shear velocity inversion are different. The shear velocity results in the depth range of (Moho + 4) km to 95 km show patterns of roughly linear trending NE-SW high and low velocity zones, similar to the trend of tectonic boundaries [*Whitmeyer and Karlstrom*, 2007]. The northern boundary of Yavapai terrane corresponds roughly with a trend of lower shear wave velocities in southern South Dakota, southern Minnesota, and central Wisconsin. North of this, the Superior Craton (SC) and Trans-Hudson (T-H) terranes show higher phase velocities. The southern portion of the Yavapai and northern portion of Mazatzal terranes are marked by NE trending high velocity zones in eastern Kansas, western Missouri, Iowa, and southern Wisconsin. South of the Mazatzal boundary another NE trending high velocity zone is observed in Oklahoma, southern Missouri,

central Indiana and Ohio. This high velocity region is cut by lower velocities within Illinois, which trend NNW from the Reelfoot Rift (RR). Furthermore, this higher velocity zone extends south of the Mazatzal terrane but rather falls within the northern portions of the Granite-Rhyolite Province [*Whitmeyer and Karlstrom*, 2007]. Shear velocities within the Ouachita Embayment (OE) are relatively high for (Moho + 4) km down to 55 km (4.7 - 4.8 km/s). At greater depths (65 km - 95 km), shear velocities are more moderate there (4.4 - 4.5 km/s) there. The lower velocities may suggest that the upper mantle in this depth range may have been modified by rifting during the Cambrian [*Thomas and Astini*, 1996; *Thomas*, 2011] and possibly further by collision during the Ouachita Marathon orogeny and subsequent Pangea breakup [*Porter et al.*, 2016]. At 55 km depth in the mantle low shear velocity results show in east Texas that connect up through southeastern Oklahoma, Arkansas and into the Reelfoot Rift (RR). High velocity zones persist within central Texas, and also central Mississippi and Alabama. Lower velocity zones can also be observed in a roughly continuous zone through central Tennessee, the central Appalachian Anomaly (CAA) and the Northeast Anomaly (NEA).

The two distinct low velocities anomalies (CAA and NEA) described in Chapter 3 are also prominent in the shear velocity inversion results for the eastern U.S. The locations of both anomalies coincide quite well with Rayleigh wave velocity results in eastern U.S. from *Liu and Holt* [2015, 2016b], surface wave tomography results from *Jin and Gaherty* [2015]; *Pollitz and Mooney* [2016], and body wave velocity models at depths of $\sim$ 60 km - 300 km obtained by *Schmandt and Lin* [2014]. *Porter et al.* [2016] claimed that both CAA and NEA extend to considerable depths within the lithosphere. *Schmandt and Lin*

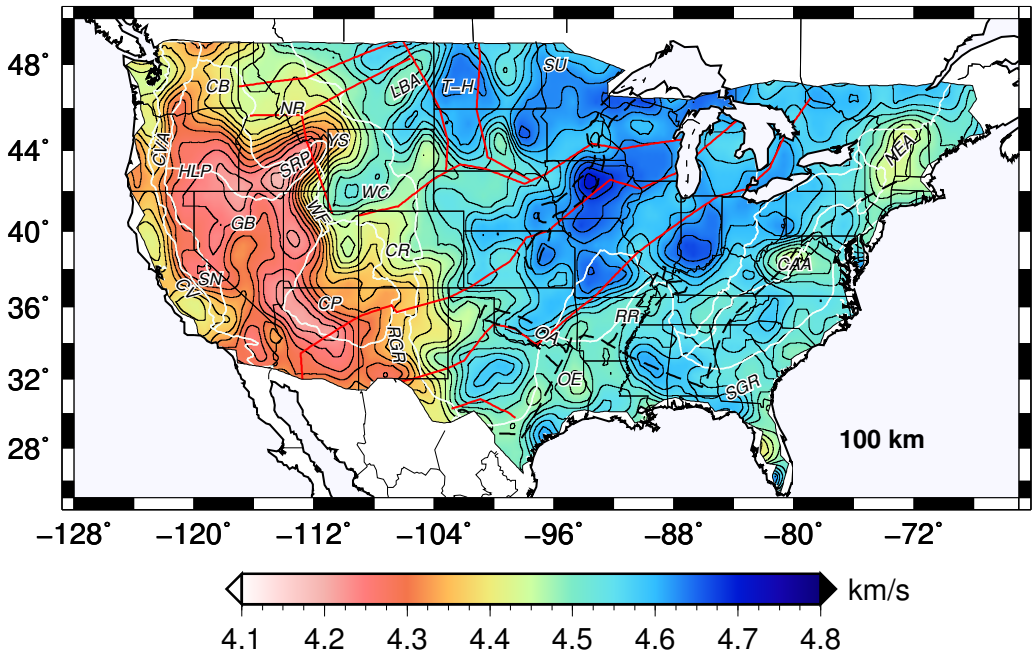

FIGURE 4.15: Map showing shear velocities at the depth of 100 km. Geographic features are indicated as: SGR, South Georgia Rift, WC, Wyoming Craton; SU, Superior Upland.

[2014] and *Pollitz and Mooney* [2016] pointed out that the center of CAA corresponds with an Eocene (∼47 Ma) swarm of basaltic volcanism, which is associated with the delamination of an eclogitic keel from the base of the crust [*Mazza et al.*, 2014]. *Eaton and Frederiksen* [2007] and *Villemaire et al.* [2012] argued that the NEA coincides with the inferred track of Great Meteor hotspot (∼200 - 110 Ma), which extends from northern Hudson bay to the northeast U.S. coast, and continues southeast as a chain of seamounts into the Atlantic ocean [*Duncan*, 1984].

4.3.3 Shear Velocities within 100 km - 150 km Depth

Within the depth range of 100 km - 150 km in the upper mantle (Figure 4.15, 4.16), we observe prominent low velocity features (4.2 - 4.4 km/s) in the western U.S. in the

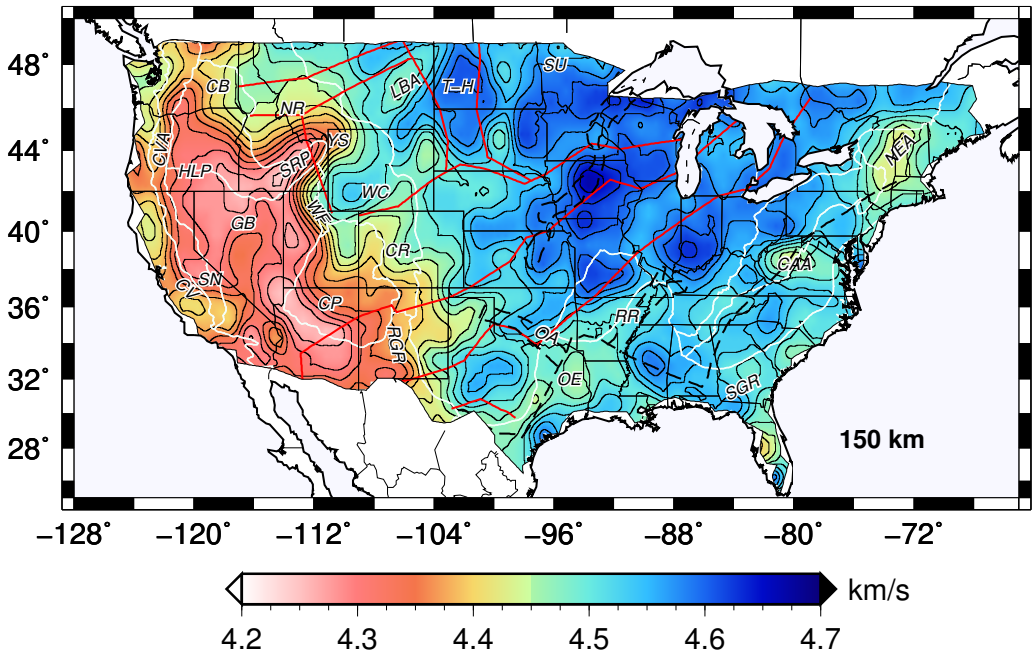

FIGURE 4.16: Map showing shear velocities at the depth of 150 km.

Snake River Plane (SRP), High Lava Plain (HLP), eastern Great Basin (GB), along the western edge of Colorado Plateau (CP), and in western Arizona. The Wyoming Craton (WC), which lies west of the Cordilleran strain also appears as a high-velocity region (4.45 - 4.55 km/s), consistent with thick lithosphere beneath it. Higher phase velocity values (4.4 km/s) are resolved, at least in part, in the regions of the Isabella Anomaly [*Schmandt and Humphreys*, 2010; *Jones et al.*, 2014] and southern Sierra Nevada (SN). The lower velocity adjacent to the Little Belt Arc (LBA) in east-central Montana is still present at this depth range. Although possibly not well resolved due to its thin spatial distribution, there is a roughly N-S trending lower velocity zone in east central North and South Dakota that approximately corresponds spatially with the suture zone between the Trans-Hudson (T-H) orogen and the Superior Craton (SC) [*Whitmeyer and Karlstrom*, 2007]. Many of the northeast trending zones of high and low shear wave velocity noted

for the (Moho + 4) km to 95 km depth range (Figure 4.10, 4.11, 4.12, 4.13, 4.14) are also apparent for this depth range of 100 km - 150 km. Within the Gulf Coast region low shear velocities exist in the Oklahoma Aulocogen (OA), the Ouachita Embayment (OE) and Realfoot Rift (RR). The high velocities in central Texas are still present along with the high velocity values in central Mississippi and Alabama. The CAA and the NEA remain prominent within this depth, which is consistent with body wave studies in the upper mantle from *Schmandt and Lin* [2014]. A low velocity anomaly starts to show up in the South Georgia Rift (SGR) at 100 km depth, which may be part of Central Atlantic Magmatic Province (CAMP) that formed $\sim$ 200 Ma [*Heffner et al.*, 2012; *Pollitz and Mooney*, 2016].

In general, low velocities are present in the western U.S. and along the continent margins, higher velocities are observed within the region bounded by the Grenville/Llano front [*Whitmeyer and Karlstrom*, 2007] and the eastern limit of Cordilleran strain [*DeCelles*, 2004], which comprises much of the core of the Craton. This observation is consistent with plate boundary processes reworking and possibly rejuvenating the mantle along the margins on the continent [*Porter et al.*, 2016].

4.3.4 Shear Velocities within 160 km - 200 km Depth

For the depth range of 160 km - 200 km (Figure 4.17, 4.18, 4.19, 4.20), many of the above described anomalies within the western U.S., like the low velocity regions (4.2 - 4.4 km/s) in the Great Basin (GB), the Sierra Nevada (SN), the Little Belt Arc (LBA) are still apparent. However, the low velocity regions in the Snake River Plain (SRP) and

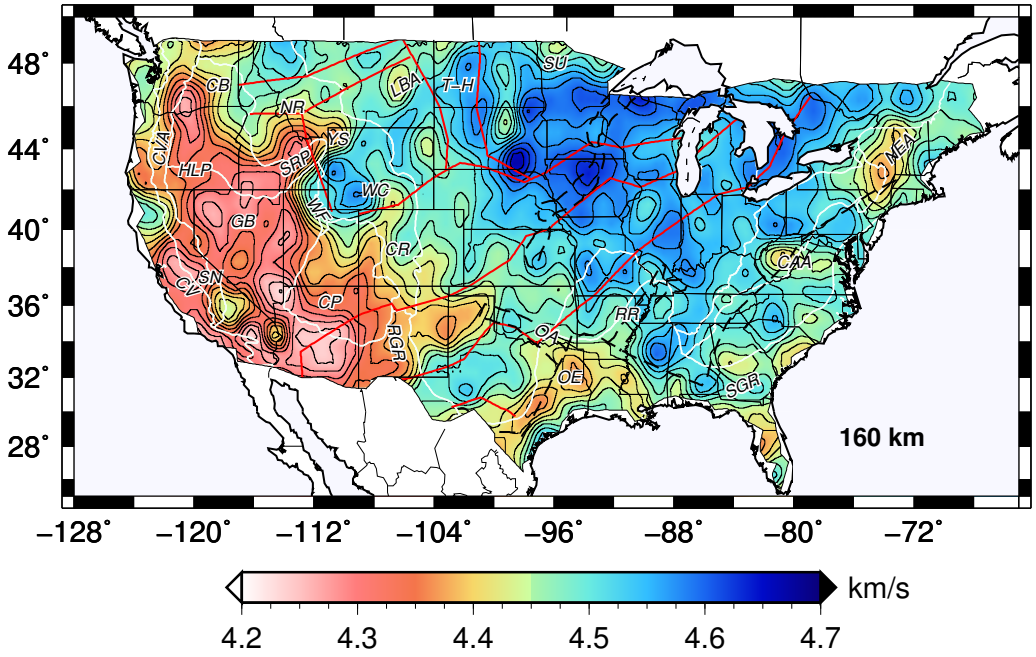

FIGURE 4.17: Map showing shear velocities at the depth of 160 km.

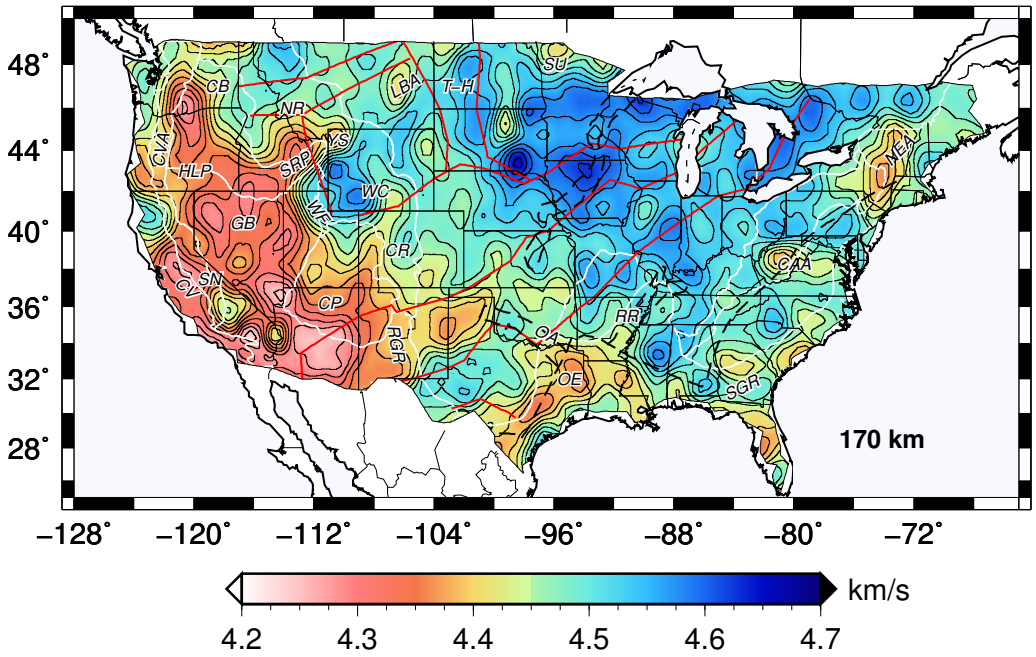

FIGURE 4.18: Map showing shear velocities at the depth of 170 km.

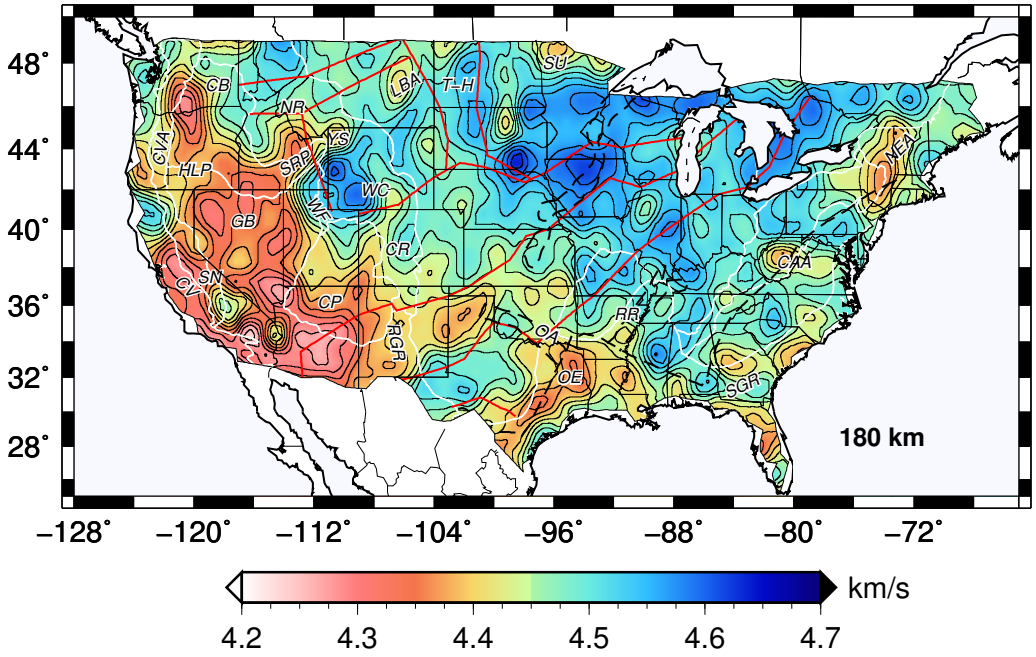

FIGURE 4.19: Map showing shear velocities at the depth of 180 km.

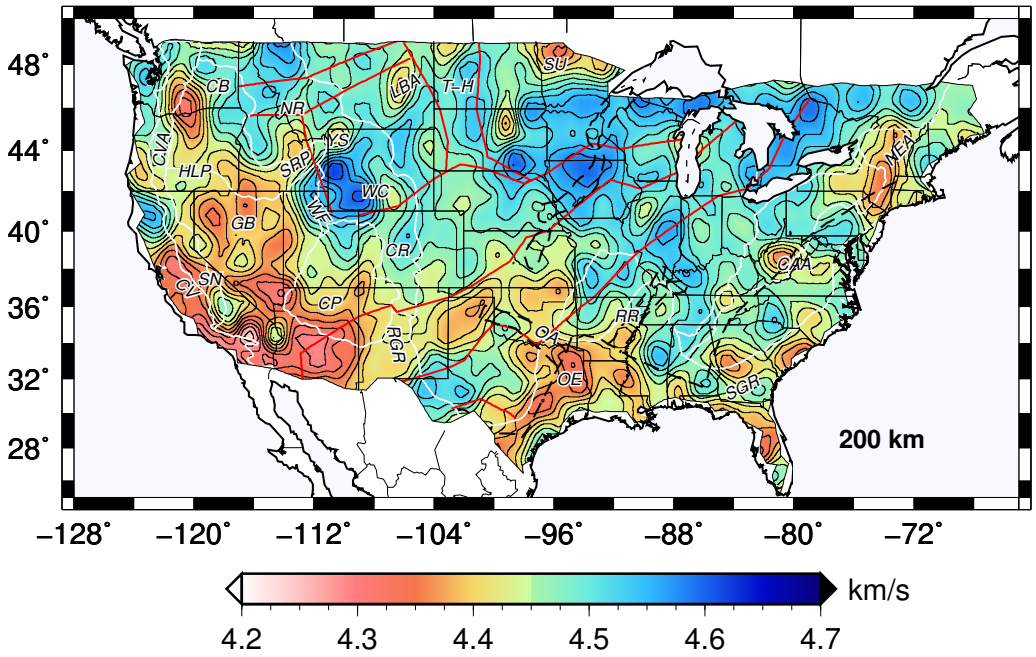

FIGURE 4.20: Map showing shear velocities at the depth of 200 km.

Yellowstone (YS) regions are weaker at 200 km, which are consistent with the 200 km bottom of these shear velocity anomalies determined in Rayleigh wave tomography studies [*Wagner et al.*, 2010]. The shear velocity differences between the western and eastern U.S. are less clear. High velocities within eastern Washington and western Idaho are consistent with a large high-velocity "Siletzia curtain" extending vertically beneath the Challis magmatic trend imaged by teleseismic tomography from *Schmandt and Humphreys* [2011], who attributed this seismically fast upper mantle to subducted ocean lithosphere. The Wyoming Craton (WC) and the northern Colorado Plateau (CP) stand out as significant high shear velocity anomalies (4.55 - 4.65 km/s) to 200 km depth.

We observe a low shear velocity region (4.35 - 4.45 km/s) trending N-S beneath the Great Plains in the central U.S. from the southern Gulf state region into North Dakota and even northern Minnesota (Superior Upland (SU)), which are somewhat enigmatic and to our knowledge have not been described to date [*Liu and Holt*, 2016b]. This could reflect asthenosphere signature, or possibly the influence of hydration mechanisms from the Farallon slab [*Humphreys et al.*, 2003; *Jones et al.*, 2015]. Alternatively, these anomalies may reflect the influence of anisotropy layering within the lithosphere described by *Yuan and Romanowicz* [2010]. The low velocity zone (4.4 - 4.45 km/s) in the Reelfoot Rift (RR) is still pronounced up to 200 km [*Bedle and van der Lee*, 2006; *Pollitz and Mooney*, 2016]. Lower velocities (4.35 - 4.45 km/s) are observed along the Oklahoma Aulocogen (OA), Ouachita Embayment (OE), and in southern Texas, Louisiana, and Mississippi [*Zhang et al.*, 2009; *Pollitz and Mooney*, 2014]. Whereas fast velocities (4.45 - 4.55 km/s) are observed in the central Texas for the depth range of 55 km - 200 km, for

depth range of 150 km - 200 km we observe slower velocities (4.35 - 4.45 km/s) distributed in northern Texas and further west into Arizona and east into Oklahoma.

The low velocities (4.35 - 4.4 km/s) beneath the South Georgia Rift (SGR) are more prominent for this depth range, especially for 180 km - 200 km, where a semi-continuous low velocity region starts from southern Alabama, passes through central and southern Georgia, South Carolina, and North Carolina. *Chu et al.* [2013] attributed low velocity anomalies observed between Virginia and the mid-continent to hotspot interaction with the thermal-chemical lithosphere. *Pollitz and Mooney* [2016] argued that the hotspot interaction within regions of lithosphere containing significant volumes of igneous intrusions associated with CAMP may also contribute to low velocity anomalies within the lower lithosphere. The two hotspot tracks [*Chu et al.*, 2013] show paths that are roughly consistent with patterns of low velocity anomalies in the depth range of 170 km - 200 km. The continuous band of lower velocities in north and south Carolina, Georgia, the southern Gulf states, and east Texas are likewise consistent with the Bermuda hotspot track [*Chu et al.*, 2013]. The low velocities in NEA and CAA are present for the depth range of 55 km - 200 km, suggesting they are associated with the entire lithosphere mantle [*Porter et al.*, 2016]. The CAA could be particularly strong because it may be associated with lithosphere delamination [*Mazza et al.*, 2014; *Schmandt and Lin*, 2014; *Porter et al.*, 2016].

4.4 Conclusion

We invert 8 s - 150 s Rayleigh wave phase velocities obtained from ambient noise tomography and wave gradiometry to produce high-resolution 3-D shear velocity models in the continental U.S. The broad depth range (8 km - 200 km) of these models allow us to examine the lithospheric structure of the continent in great detail and associate modern subsurface features in the crust and upper mantle to the formation of the continent and orogenic events that impacted the structure and evolution of the lithosphere in North America. These models highlight the complexities in the evolution of the continent and enable a direct comparison between lithospheric features in the western, central and eastern of the United States.

Velocities in the depth ranges of 55 km - 200 km show great variability not only within the western U.S. but also in central and eastern U.S. regions. Rather than one continuous Craton high velocity structure within the central core of the continent, USArray data have revealed a picture of the upper mantle lithosphere there that appears to be heterogeneous. Furthermore there are surprising low velocity zones in the central Appalachian anomaly (CAA) and Northeast Anomaly (NEA), and deep low velocity zones beneath parts of the Great Plains and a deep reaching high velocity zone beneath parts of the Wyoming Craton (WC). Variability in velocities at depths greater than 100 km could reflect asthenosphere signature, or possibly the influence of hydration mechanisms from the Farallon slab [*Humphreys et al.*, 2003; *Jones et al.*, 2015], hotspot interaction with the thermal-chemical lithosphere [*Chu et al.*, 2013], or other processes that have given

rise to erosion variable erosion of the lithosphere [*Foley*, 2008].

Bibliography

Aster, R. C., B. Borchers, and C. H. Thurber (2011), *Parameter Estimation and Inverse Problems*, Waltham, MA.

Bassin, C. (2000), The current limits of resolution for surface wave tomography in North America, *EOS Trans. AGU*.

Beavan, J., and J. Haines (2001), Contemporary horizontal velocity and strain rate fields of the Pacific-Australian plate boundary zone through New Zealand, *J. Geophys. Res.*, *106*(B1), 741, doi:10.1029/2000jb900302.

Bedle, H., and S. van der Lee (2006), Fossil flat-slab subduction beneath the Illinois basin, usa, *Tectonophysics*, *424*(1), 53–68, doi:10.1016/j.tecto.2006.06.003.

Bedle, H., and S. van der Lee (2009), S velocity variations beneath north america, *J. Geophy. Res. Solid Earth*, *114*(B7), doi:10.1029/2008JB005949.

Beghein, C., J. A. Snoke, and M. J. Fouch (2010), Depth constraints on azimuthal anisotropy in the great basin from rayleigh-wave phase velocity maps, *Earth Planet. Sci. Lett.*, *289*(3), 467–478, doi:10.1016/j.epsl.2009.11.036.

Bensen, G., M. Ritzwoller, M. Barmin, A. Levshin, F. Lin, M. Moschetti, N. Shapiro, and Y. Yang (2007), Processing seismic ambient noise data to obtain reliable broad-band surface wave dispersion measurements, *Geophys. J. Int.*, *169*(3), 1239–1260, doi: 10.1111/j.1365-246X.2007.03374.x.

Bensen, G., M. Ritzwoller, and Y. Yang (2009), A 3-D shear velocity model of the crust and uppermost mantle beneath the United States from ambient seismic noise, *Geophys. J. Int.*, *177*(3), 1177–1196, doi:10.1111/j.1365-246X.2009.04125.x.

Benz, H., and G. Zandt (1993), structure of the San Andreas fault system in northern and central California, *Seismic Tomography: Theory and Practice*, p. 440.

Birtill, J. W., and F. E. Whiteway (1965), The application of phased arrays to analysis of seismic body waves, philos, *Trans. R. Soc. London, Ser. A*, (258), 421–493, doi: 10.1098/rsta.1965.0048.

Blackwell, D., M. Richards, Z. Frone, A. Ruzo, R. Dingwall, and M. Williams (2011), Temperature-at-depth maps for the conterminous US and geothermal resource estimat, *GRC Transactions*, *35*(GRC1029452).

Bodin, T., and V. Maupin (2008), Resolution potential of surface wave phase velocity measurements at small arrays, *Geophys. J. Int.*, *172*(2), 698–706, doi:10.1111/j. 1365-246X.2007.03668.x.

Brudzinski, M. R., and R. M. Allen (2007), Segmentation in episodic tremor and slip all along Cascadia, *Geology*, *35*(10), 907, doi:10.1130/g23740a.1.

Bunks, C., F. M. Saleck, S. Zaleski, and G. Chavent (1995), Multiscale seismic waveform inversion, *Geophysics*, *60*(5), 1457–1473, doi:10.1190/1.1443880.

Burdick, S., C. Li, V. Martynov, T. Cox, J. Eakins, T. Mulder, L. Astiz, F. L. Vernon, G. L. Pavlis, and R. D. van der Hilst (2008), Upper mantle heterogeneity beneath North America from travel time tomography with global and USArray transportable array data, *Seismol. Res. Lett.*, *79*(3), 384–392, doi:10.1785/gssrl.79.3.384.

Burdick, S., R. D. van der Hilst, F. L. Vernon, V. Martynov, T. Cox, J. Eakins, G. H. Karasu, J. Tylell, L. Astiz, and G. L. Pavlis (2014), Model update January 2013: Upper mantle heterogeneity beneath North America from travel-time tomography with global and USArray transportable array data, *Seismol. Res. Lett.*, *85*(1), 77–81, doi: 10.1785/0220130098.

Cao, A., and A. Levander (2010), High-resolution transition zone structures of the gorda slab beneath the western United States: Implication for deep water subduction, *J. Geophys. Res.*, *115*(B7), doi:10.1029/2009jb006876.

Cerveny, V. (2005), *Seismic ray theory*, Cambridge University Press, Cambridge, UK.

Chu, R., W. Leng, D. V. Helmberger, and M. Gurnis (2013), Hidden hotspot track beneath the eastern United States, *Nature Geoscience*, *6*(11), 963–966, doi:10.1002/ 2015GL066637.

Cook, F. A., and J. E. Oliver (1981), The late Precambrian-early Paleozoic continental edge in the Appalachian orogen, *Am. J. Sci.*, *281*(8), 993–1008.

Crotwell, H. P., and T. J. Owens (2005), Automated receiver function processing, *Seismological Res. Lett.*, *76*(6), 702–709, doi:10.1785/gssrl.76.6.702.

Dahlen, F. A., and J. Tromp (1998), *Theoretical Global Seismology*, Princeton University Press, Princeton, NJ.

De Boor, C. (1987), *A practical guide to splines*, 392 pp., Springer-Verlag, New York.

DeCelles, P. G. (2004), Late Jurassic to Eocene evolution of the Cordilleran thrust belt and foreland basin system, western USA, *American Journal of Science*, *304*(2), 105–168, doi:10.2475/ajs.304.2.105.

Duller, R. A., A. C. Whittaker, J. B. Swinehart, J. J. Armitage, H. D. Sinclair, A. Bair, and P. A. Allen (2012), Abrupt landscape change post–6 ma on the central Great Plains, usa, *Geology*, *40*(10), 871–874, doi:10.1130/G32919.1.

Duncan, R. A. (1984), Age progressive volcanism in the New England seamonts and the opening of the central Atlantic Ocean, *J. Geophys. Res.*, *89*(B12), 9980–9990, doi:10.1029/JB089iB12p09980.

Eaton, D. W., and A. Frederiksen (2007), Seismic evidence for convection-driven motion of the North American plate, *Nature*, *446*(7134), 428–431, doi:10.1038/nature05675.

Ekström, G. (2014), Love and Rayleigh phase-velocity maps, 5–40 s, of the western and central USA from USArray data, *Earth Planet. Sci. Lett.*, *402*, 42–49, doi:10.1016/j.epsl.2013.11.022.

Evanzia, D., J. Pulliam, R. Ainsworth, H. Gurrola, and K. Pratt (2014), Seismic Vp & Vs tomography of Texas & Oklahoma with a focus on the Gulf Coast margin, *Earth Planet. Sci. Lett.*, *402*, 148–156, doi:10.1016/j.epsl.2013.12.027.

Evernden, J. F. (1954), Direction of approach of rayleigh waves and related problems (part II), *Bull. Seismol. Soc. Am.*, *44*(2A), 159–184.

Fenneman, N. M. (1917), Physiographic subdivision of the United States, *Proc. Natl. Acad. Sci.*, *3*(1), 17–22.

Fischer, K. M., H. A. Ford, D. L. Abt, and C. A. Rychert (2010), The lithosphere-asthenosphere boundary, *Annual Review of Earth and Planetary Sciences*, *38*, 551–575, doi:10.1146/annurev-earth-040809-152438.

Fletcher, R., and C. M. Reeves (1964), Function minimization by conjugate gradients, *The Computer Journal*, *7*(2), 149–154, doi:10.1093/comjnl/7.2.149.

Foley, S. F. (2008), Rejuvenation and erosion of the cratonic lithosphere, *Nature Geoscience*, *1*(8), 503–510, doi:10.1038/ngeo261.

Forte, A. (2007), Constraints on seismic models from other disciplinesimplications for mantle dynamics and composition, *Treatise on Geophysics*, *1*, 805–858.

Forte, A., J. Mitrovica, R. Moucha, N. Simmons, and S. Grand (2007), Descent of the ancient Farallon slab drives localized mantle flow below the New Madrid seismic zone, *Geophys. Res. Lett.*, *34*(4), doi:10.1029/2006GL027895.

Foster, A., G. Ekström, and M. Nettles (2013), Surface wave phase velocities of the western united states from a two-station method, *Geophys. J. Int.*, p. ggt454, doi: 10.1093/gji/ggt454.

Friederich, W., E. Wielandt, and S. Stange (1995), Non-plane geometries of seismic surface wavefields and their implications for regional surface-wave tomography, *Geophys. J. Int.*, *119*, 931–948, doi:10.1111/j.1365-246X.1994.tb04026.x.

Friederich, W., S. Hunzinger, and E. Wielandt (2000), A note on the interpretation of seismic surface waves over 3-d structures, *Geophys. J. Int.*, (142), 000–000, doi: 10.1046/j.1365-246X.2000.01241.x.

Ghosh, A., and E. W. Holt (2012), Plate motions and stresses from global dynamic models, *Science*, *335*(6070), 838–43, doi:10.1126/science.1214209.

Ghosh, A., E. W. Holt, and W. L. (2013), Predicting the lithospheric stress field and plate motions by joint modeling of lithosphere and mantle dynamics, *J. Geophys. Res. Solid Earth*, *118*(1), 346–368, doi:10.1029/2012jb009516.

Haines, A. J., and E. W. Holt (1993), A procedure for obtaining the complete horizontal motions within zones of distributed deformation from the inversion of strain rate data, *J. Geophys. Res.*, *98*(B7), 12,057, doi:10.1029/93jb00892.

Haines, A. J., J. A. Jackson, W. E. Holt, D. C. Agnew, and D. C. Agnew (1998), *Representing distributed deformation by continuous velocity fields*, Institute of Geological & Nuclear Sciences.

Heffner, D. M., J. H. Knapp, O. M. Akintunde, and C. C. Knapp (2012), Preserved extent of Jurassic flood basalt in the South Georgia Rift: A new interpretation of the J horizon, *Geology*, *40*(2), 167–170, doi:10.1130/G32638.1.

Heller, P. L., K. Dueker, and M. E. McMillan (2003), Post-paleozoic alluvial gravel transport as evidence of continental tilting in the US Cordillera, *Geol. Soc. Am. Bull.*, *115*(9), 1122–1132, doi:10.1130/B25219.1.

Herrmann, R., and C. Ammon (2002), Computer programs in seismology: Surface waves, receiver functions and crustal structure, *St. Louis University, St. Louis, MO*.

Holt, E. W., and G. Shcherbenko (2013), Toward a continuous monitoring of the horizontal displacement gradient tensor field in southern California using GPS observations from Plate Boundary Observatory (PBO), *Seismol. Res. Lett.*, *84*(3), 455–467, doi: 10.1785/0220130004.

Holt, E. W., N. Chamot-Rooke, X. Le Pichon, A. J. Haines, B. Shen-Tu, and J. Ren (2000a), Velocity field in Asia inferred from quaternary fault slip rates and global positioning system observations, *J. Geophys. Res.*, *105*(B8), 19,185, doi:10.1029/2000jb900045.

Holt, E. W., Shen-Tu, A. J. Haines, and J. Jackson (2000b), On the determination of self-consistent strain rate fields within zones of distributed continental deformation, in history and dynamics of global plate motions, *Geophys. Monogr. Ser.*, doi:10.1029/GM121p0113.

Humphreys, E., E. Hessler, K. Dueker, G. L. Farmer, E. Erslev, and T. Atwater (2003), How laramide-age hydration of north american lithosphere by the farallon slab controlled subsequent activity in the western united states, *International Geology Review*, *45*(7), 575–595, doi:10.2747/0020-6814.45.7.575.

Jin, G., and J. B. Gaherty (2015), Surface wave phase-velocity tomography based on multichannel cross-correlation, *Geophys. J. Int.*, *201*(3), 1383–1398, doi:10.1093/gji/ggv079.

Jones, C. H., H. Kanamori, and S. W. Roecker (1994), Missing roots and mantle drips: Regional Pn and teleseismic arrival times in the southern Sierra Nevada and vicinity, California, *J. Geophy. Res. Solid Earth*, *99*(B3), 4567–4601, doi:10.1029/93JB01232.

Jones, C. H., H. Reeg, G. Zandt, H. Gilbert, T. J. Owens, and J. Stachnik (2014), P-wave tomography of potential convective downwellings and their source regions, Sierra Nevada, California, *Geosphere*, *10*(3), 505–533, doi:10.1130/GES00961.1.

Jones, C. H., K. H. Mahan, L. A. Butcher, W. B. Levandowski, and G. L. Farmer (2015), Continental uplift through crustal hydration, *Geology*, *43*(4), 355–358, doi:10.1130/G36509.1.

Keller, G. R., and R. D. Hatcher (1999), Some comparisons of the structure and evolution of the southern Appalachian-Ouachita orogen and portions of the Trans-European Suture Zone region, *Tectonophysics*, *314*(1), 43–68, doi:10.1016/S0040-1951(99)00236-X.

Kirchner, J. G. (1977), Evidence for late Tertiary volcanic activity in the northern Black Hills, South Dakota, *Science*, *196*(4293), 977–977, doi:10.1126/science.196.4293.977.

Knopoff, L., S. Mueller, and W. Pilant L. (1966), Structure of the crust and upper mantle in the Alps from the phase velocity of Rayleigh waves, *Bull. Seismol. Soc. Am.*, *56*(5).

Kumar, P., X. Yuan, R. Kind, and J. Mechie (2012), The lithosphere-asthenosphere boundary observed with USArray receiver functions, *Solid Earth*, *3*(1), 149, doi:10.5194/se-3-149-2012.

Kustowski, B., G. Ekstrm, and A. M. Dziewoski (2008), Anisotropic shear-wave velocity structure of the earth's mantle: A global model, *J. Geophys. Res.*, *113*(B6), doi:10.1029/2007jb005169.

Langston, C. A. (2006), Explosion source strong ground motions in the Mississippi Embayment, *Bull. Seismol. Soc. Am.*, *96*(3), 1038–1054, doi:10.1785/0120050105.

Langston, C. A. (2007a), Spatial gradient analysis for linear seismic arrays, *Bull. Seismol. Soc. Am.*, *97*(1B), 265–280, doi:10.1785/0120060100.

Langston, C. A. (2007b), Wave gradiometry in two dimensions, *Bull. Seismol. Soc. Am.*, *97*(2), 401–416, doi:10.1785/0120060138.

Langston, C. A. (2007c), Wave gradiometry in the time domain, *Bull. Seismol. Soc. Am.*, *97*(3), 926–933, doi:10.1785/0120060152.

Langston, C. A., and S. P. Horton (2014), Three-dimensional seismic-velocity model for the unconsolidated Mississippi Embayment sediments from H/V ambient noise measurements, *Bull. Seismol. Soc. Am.*, *104*(5), 2349–2358, doi:10.1785/0120140026.

Laske, G., G. Masters, et al. (1997), A global digital map of sediment thickness, *Eos Trans. AGU*, *78*(F483).

Levander, A., B. Schmandt, M. S. Miller, K. Liu, K. E. Karlstrom, R. S. Crow, C. T. Lee, and E. D. Humphreys (2011), Continuing Colorado plateau uplift by delamination-style convective lithospheric downwelling, *Nature*, *472*(7344), 461–5, doi:10.1038/nature10001.

Li, A., D. W. Forsyth, and K. M. Fischer (2003), Shear velocity structure and azimuthal anisotropy beneath eastern north america from rayleigh wave inversion, *J. Geophy. Res. Solid Earth*, *108*(B8), doi:10.1029/2002JB002259.

Liang, C., and C. A. Langston (2008), Ambient seismic noise tomography and structure of eastern North America, *J. Geophys. Res.*, *113*(B3), doi:10.1029/2007jb005350.

Liang, C., and C. A. Langston (2009), Wave gradiometry for USArray: Rayleigh waves, *J. Geophys. Res.*, *114*(B2), doi:10.1029/2008jb005918.

Lin, F.-C., and M. H. Ritzwoller (2011a), Helmholtz surface wave tomography for isotropic and azimuthally anisotropic structure, *Geophys. J. Int.*, *186*(3), 1104–1120, doi:10.1111/j.1365-246X.2011.05070.x.

Lin, F.-C., and M. H. Ritzwoller (2011b), Apparent anisotropy in inhomogeneous isotropic media, *Geophys. J. Int.*, *186*(3), 1205–1219, doi:10.1111/j.1365-246X.2011.05100.x.

Lin, F.-C., and B. Schmandt (2014), Upper crustal azimuthal anisotropy across the contiguous U.S. determined by Rayleigh wave ellipticity, *Geophys. Res. lett.*, *41*, doi:10.1002/2014GL062362.

Lin, F.-C., M. P. Moschetti, and M. H. Ritzwoller (2008), Surface wave tomography of the western United States from ambient seismic noise: Rayleigh and Love wave phase velocity maps, *Geophys. J. Int.*, *173*(1), 281–298, doi:10.1111/j.1365-246X.2008.03720.x.

Lin, F.-C., M. H. Ritzwoller, and R. Snieder (2009), Eikonal tomography: surface wave tomography by phase front tracking across a regional broad-band seismic array, *Geophys. J. Int.*, *177*(3), 1091–1110, doi:10.1111/j.1365-246X.2009.04105.x.

Lin, F.-C., V. C. Tsai, and M. H. Ritzwoller (2012), The local amplification of surface waves: A new observable to constrain elastic velocities, density, and anelastic attenuation, *J. Geophy. Res. Solid Earth*, *117*(B6), doi:10.1029/2012JB009208.

Lin, F.-C., V. C. Tsai, and B. Schmandt (2014), 3-D crustal structure of the western United States: application of Rayleigh-wave ellipticity extracted from noise cross-correlations, *Geophys. J. Int.*, *198*(2), 656–670, doi:10.1093/gji/ggu160.

Liu, Y., and W. E. Holt (2015), Wave gradiometry and its link with helmholtz equation solutions applied to USArray in the eastern U.S., *J. Geophy. Res. Solid Earth*, *120*, 1–30, doi:10.1002/2015JB011982.

Liu, Y., and W. E. Holt (2016a), Apply wave gradiometry to six Gulf of California events recorded by USArray, *Manuscript in preparation*.

Liu, Y., and W. E. Holt (2016b), Wave gradiometry and Helmholtz equation solution applied to USArray across the contiguous U.S., *Submitted to Geochemistry, Geophysics, Geosystems*.

Mazza, S. E., E. Gazel, E. A. Johnson, M. J. Kunk, R. McAleer, J. A. Spotila, M. Bizimis, and D. S. Coleman (2014), Volcanoes of the passive margin: The youngest magmatic event in eastern North America, *Geology*, *42*(6), 483–486, doi:10.1130/G35407.1.

Meier, T., K. Dietrich, B. Stckhert, and H. P. Harjes (2004), One-dimensional models of shear wave velocity for the eastern mediterranean obtained from the inversion of Rayleigh wave phase velocities and tectonic implications, *Geophys. J. Int.*, *156*(1), 45–58, doi:10.1111/j.1365-246X.2004.02121.x.

Moschetti, M., M. Ritzwoller, F.-C. Lin, and Y. Yang (2010a), Crustal shear wave velocity structure of the western United States inferred from ambient seismic noise and earthquake data, *J. Geophy. Res. Solid Earth*, *115*(B10), doi:10.1029/2010JB007448.

Moschetti, M., M. Ritzwoller, F. Lin, and Y. Yang (2010b), Seismic evidence for widespread western-US deep-crustal deformation caused by extension, *Nature*, *464*(7290), 885–889, doi:10.1038/nature08951.

Moucha, R., A. M. Forte, J. X. Mitrovica, D. B. Rowley, S. Quéré, N. A. Simmons, and S. P. Grand (2008), Dynamic topography and long-term sea-level variations: There is no such thing as a stable continental platform, *Earth Planet. Sci. Lett.*, *271*(1), 101–108, doi:doi:10.1016/j.epsl.2008.03.056.

Obrebski, M., R. M. Allen, F. Pollitz, and S.-H. Hung (2011), Lithosphere-asthenosphere interaction beneath the western United States from the joint inversion of body-wave traveltimes and surface-wave phase velocities, *Geophys. J. Int.*, *185*(2), 1003–1021, doi:10.1111/j.1365-246X.2011.04990.x.

Park, J., and Y. Yu (1993), Seismic determination of elastic anistropy and mantle flow, *SCIENCE-NEW YORK THEN WASHINGTON*, *261*, 1159–1159.

Parker, E. H., R. B. Hawman, K. M. Fischer, and L. S. Wagner (2013), Crustal evolution across the southern appalachians: Initial results from the sesame broadband array, *Geophys. Res. lett.*, *40*(15), 3853–3857, doi:10.1002/grl.50761.

Pollitz, F. F., and W. D. Mooney (2014), Seismic structure of the central US crust and shallow upper mantle: uniqueness of the reelfoot rift, *Earth Planet. Sci. Lett.*, *402*, 157–166, doi:10.1016/j.epsl.2013.05.042.

Pollitz, F. F., and W. D. Mooney (2016), Seismic velocity structure of the crust and shallow mantle of the Central and Eastern United States by seismic surface wave imaging, *Geophys. Res. Lett.*, doi:10.1002/2015GL066637.

Pollitz, F. F., and J. A. Snoke (2010), Rayleigh-wave phase-velocity maps and three-dimensional shear velocity structure of the western US from local non-plane surface wave tomography, *Geophys. J. Int.*, *180*(3), 1153–1169, doi:10.1111/j.1365-246X.2009.04441.x.

Porritt, R. W., R. M. Allen, and F. F. Pollitz (2014), Seismic imaging east of the Rocky Mountains with USArray, *Earth Planet. Sci. Lett.*, *402*, 16–25, doi:10.1016/j.epsl.2013.10.034.

Porter, R., Y. Liu, and W. E. Holt (2016), Lithospheric records of orogeny within the continental US, *Geophys. Res. Lett.*, doi:10.1002/2015GL066950.

Roth, J. B., M. J. Fouch, D. E. James, and R. W. Carlson (2008), Three-dimensional seismic velocity structure of the northwestern united states, *Geophys. Res. Lett.*, *35*(15), doi:10.1029/2008GL034669.

Rychert, C. A., K. M. Fischer, and S. Rondenay (2005), A sharp lithosphere-asthenosphere boundary imaged beneath eastern North America, *Nature*, *436*(7050), 542–545, doi:10.1038/nature03904.

Schmandt, B., and E. Humphreys (2010), Complex subduction and small-scale convection revealed by body-wave tomography of the western United States upper mantle, *Earth Planet. Sci. Lett.*, *297*(3-4), 435–445, doi:10.1016/j.epsl.2010.06.047.

Schmandt, B., and E. Humphreys (2011), Seismically imaged relict slab from the 55 Ma Siletzia accretion to the northwest United States, *Geology*, *39*(2), 175–178, doi:10.1130/g31558.1.

Schmandt, B., and F.-C. Lin (2014), P and s wave tomography of the mantle beneath the United States, *Geophys. Res. lett.*, *41*, doi:10.1002/2014GL061231.

Schmandt, B., F.-C. Lin, and K. E. Karlstrom (2015), Distinct crustal isostasy trends east and west of the Rocky Mountain Front, *Geophys. Res. Lett.*, doi:10.1002/2015GL066593.

Shen, W., M. H. Ritzwoller, and V. Schulte-Pelkum (2013a), A 3-d model of the crust and uppermost mantle beneath the central and western US by joint inversion of receiver functions and surface wave dispersion, *J. Geophys. Res. Solid Earth*, *118*(1), 262–276, doi:10.1029/2012jb009602.

Shen, W., M. H. Ritzwoller, and V. Schulte-Pelkum (2013b), Crustal and uppermost mantle structure in the central U.S. encompassing the mid-continent rifft, *J. Geophys. Res. Solid Earth*, *118*, 4325–4344, doi:10.1002/jgrb.50321.

Sigloch, K., N. McQuarrie, and G. Nolet (2008), Two-stage subduction history under North America inferred from multiple-frequency tomography, *Nat. Geosci.*, *1*(7), 458–462, doi:10.1038/ngeo231.

Snoke, J. A., and D. E. James (1997), Lithospheric structure of the Chaco and Parana basins of South America from surface-wave inversion, *J. Geophy. Res. Solid Earth*, *102*(B2), 2939–2951.

Stuart, W. D., T. G. Hildenbrand, and R. W. Simpson (1997), Stressing of the New Madrid seismic zone by a lower crust detachment fault, *J. Geophy. Res. Solid Earth*, *102*(B12), 27,623–27,633, doi:10.1029/97JB02716.

Sun, D., and D. Helmberger (2011), Upper-mantle structures beneath USArray derived from waveform complexity, *Geophys. J. Int.*, *184*(1), 416–438, doi:10.1111/j.1365-246X.2010.04847.x.

Tanimoto, T., and L. Rivera (2008), The ZH ratio method for long-period seismic data: sensitivity kernels and observational techniques, *Geophys. J. Int.*, *172*(1), 187–198, doi:10.1111/j.1365-246X.2007.03609.x.

Tape, C., Q. Liu, A. Maggi, and J. Tromp (2009), Adjoint tomography of the southern california crust, *Science*, *325*(5943), 988–992, doi:10.1126/science.1175298.

Thomas, W. A. (2011), The Iapetan rifted margin of southern Laurentia, *Geosphere*, *7*(1), 97–120, doi:10.1130/GES00574.1.

Thomas, W. A., and R. A. Astini (1996), The Argentine Precordillera: a traveler from the Ouachita embayment of north American Laurentia, *Science*, *273*(5276), 752, doi: 10.1126/science.273.5276.752.

Towns, J., T. Cockerill, M. Dahan, I. Foster, K. Gaither, A. Grimshaw, V. Hazlewood, S. Lathrop, D. Lifka, G. D. Peterson, et al. (2014), XSEDE: accelerating scientific discovery, *Computing in Science & Engineering*, *16*(5), 62–74, doi: 10.1109/MCSE.2014.80.

Tromp, J., C. Tape, and Q. Liu (2005), Seismic tomography, adjoint methods, time reversal and banana-doughnut kernels, *Geophys. J. Int.*, *160*(1), 195–216, doi:10.1111/j.1365-246X.2004.02453.x.

Tromp, J., D. Komatitsch, V. Hjrleifsdttir, Q. Liu, H. Zhu, D. Peter, E. Bozdag, D. McRitchie, P. Friberg, C. Trabant, and A. Hutko (2010), Near real-time simulations of global cmt earthquakes, *Geophys. J. Int.*, *183*(1), 381–389, doi:10.1111/j.1365-246X.2010.04734.x.

van der Lee, S., and A. Frederiksen (2005), Surface wave tomography applied to the North American upper mantle, *Washington DC American Geophysical Union Geophysical Monograph Series*, *157*, 67–80, doi:10.1029/157GM05.

Villemaire, M., F. A. Darbyshire, and I. D. Bastow (2012), P-wave tomography of eastern North America: Evidence for mantle evolution from Archean to Phanerozoic, and

modification during subsequent hot spot tectonism, *J. Geophys. Res. Solid Earth*, *117*(B12302), doi:10.1029/2012JB009639,2012.

Wagner, L., D. W. Forsyth, M. J. Fouch, and D. E. James (2010), Detailed three-dimensional shear wave velocity structure of the northwestern United States from Rayleigh wave tomography, *Earth Planet. Sci. Lett.*, *299*(3), 273–284, doi:0.1016/j.epsl.2010.09.005.

Wang, X., W. E. Holt, and A. Ghosh (2015), Joint modeling of lithosphere and mantle dynamics: Evaluation of constraints from global tomography models, *J. Geophy. Res. Solid Earth*, *120*(12), 8633–8655, doi:10.1002/2015JB012188.

Wessel, P., W. H. Smith, R. Scharroo, J. Luis, and F. Wobbe (2013), Generic mapping tools: improved version released, *EOS Trans. AGU*, *94*(45), 409–410, doi:10.1002/2013EO450001.

West, J. D., M. J. Fouch, J. B. Roth, and L. T. Elkins-Tanton (2009), Vertical mantle flow associated with a lithospheric drip beneath the great basin, *Nat. Geosci.*, *2*(6), 439–444, doi:10.1038/ngeo526.

Whitmeyer, S. J., and K. E. Karlstrom (2007), Tectonic model for the proterozoic growth of north america, *Geosphere*, *3*(4), 220–259, doi:10.1130/GES00055.1.

Wielandt, E. (1993), Propagation and structural interpretation of non-plane waves, *Geophys. J. Int.*, *113*, 45–53, doi:10.1111/j.1365-246X.1993.tb02527.x.

Williams, L. M., K. M. Fisher, J. T. Freymueller, B. Tikoff, and A. M. Trehu (2010), Unlocking the secrets of the North American continent: An EarthScope science plan for 2010-2020, p. 78pp.

Yang, Y., and D. W. Forsyth (2006), Rayleigh wave phase velocities, small-scale convection, and azimuthal anisotropy beneath southern California, *J. Geophys. Res.*, *111*(B7), doi:10.1029/2005jb004180.

Yang, Y., and M. H. Ritzwoller (2008), Teleseismic surface wave tomography in the western U.S. using the transportable array component of USArray, *Geophys. Res. Lett.*, *35*(4), doi:10.1029/2007gl032278.

Yang, Y., W. Shen, and M. H. Ritzwoller (2011), Surface wave tomography on a large-scale seismic array combining ambient noise and teleseismic earthquake data, *Earthquake Science*, *24*(1), 55–64, doi:10.1007/s11589-011-0769-3.

Yuan, H., and B. Romanowicz (2010), Depth dependent azimuthal anisotropy in the western US upper mantle, *Earth Planet. Sci. Lett.*, *300*(3-4), 385–394, doi:10.1016/j.epsl.2010.10.020.

Zhang, Q., E. Sandvol, and M. Liu (2009), Lithospheric velocity structure of the New Madrid Seismic Zone: A joint teleseismic and local P tomographic study, *Geophys. Res. Lett.*, *36*(11), doi:10.1029/2009GL037687.

Zhu, H., E. Bozdağ, D. Peter, and J. Tromp (2012), Structure of the European upper mantle revealed by adjoint tomography, *Nature Geoscience*, *5*(7), 493–498, doi:10.1038/ngeo1501.

Zhu, H., E. Bozdağ, and J. Tromp (2015), Seismic structure of the european upper mantle based on adjoint tomography, *Geophys. J. Int.*, *201*(1), 18–52, doi:10.1093/gji/ggu492.